2004

PARAMETERS AFFECTING THE IMAGING AND DETECTION OF MICROBUBBLES IN BLOOD

https://hdl.handle.net/2144/1373

Boston University

BOSTON UNIVERSITY

COLLEGE OF ENGINEERING

Thesis

PARAMETERS AFFECTING THE IMAGING AND DETECTION OF MICROBUBBLES IN BLOOD

by

PAOLO ZANETTI

B.S. Boston University, 2002

Submitted in partial fulfillment of the
requirements for the degree of
Master of Science
2004

Approved by

First Reader
Ronald A Roy
Ronald A. Roy, Ph.D.
Professor of Mechanical Engineering

Second Reader
Constantin-C. Coussios, Ph.D. Cantab
Lecturer in Biomedical Engineering
Oxford University, Oxford, U.K.

Third Reader
Raymond J Nagem
Raymond Nagem, Ph.D.
Professor of Mechanical Engineering

“To Giancarlo & Gabriella Zanetti,

my parents: Grazie”

ACKNOWLEDGEMENTS

First of all, my greatest acknowledgements go to my advisor, Professor Ronald A. Roy, for his motivation and encouragement; for his care and meticulous attention to detail as well as his support in all aspects of life. My greatest thanks also go to Professor Raymond Nagem for his help and patience in reading preliminary drafts of my thesis.

I would like to give a special acknowledgement to my second reader and friend Dr. Constantin C. Coussios. Without him this project wouldn't have started and I wouldn't be here writing this thesis today. Thank you for the long hours in the lab, the continuous advice and thank you for being such a great mentor.

I would also like to thank Professor Mark W. Bitensky, Dr. Tatsuro Yoshida and Sergey Shevkoplyas from the Department of Biomedical Engineering for letting me use the facilities of the Visual and Circulatory Biophysics Laboratory.

Next, I would like to thank all the members of the PAC lab. Professor Robin Cleveland, my undergraduate advisor, for helping me make the decision of attending graduate school. Professor R. Glynn Holt, for his humor and attention to all that concerned my project. Emmanuel Bossy, the fellow from France. All the graduate students, and especially the ex-'corner group', Javier Van Cauwelaert, Caleb Farny, and Parag Chitnis, for being such great neighbors, always ready to listen and advise in moments of need. The veteran Charles Thomas for being a source of advice and knowledge. Jed Wilbur for bringing some humor to the pack. Lei Sui, Lee Sui, Hai Wang, Yuan Jing, and XinMai Yang for their help. In addition, I would like to thank previous members of the PAC lab that have greatly helped me in the past two years, namely Preston Wilson and Patrick Edson.

My Boston University acknowledgements should also include Joe Estano and David Campbell for allowing me to use the machine shop as well as Liz Katz, always ready to answer questions.

My special thanks also go to all of the friends that allowed the past two years to be also enjoyable and entertaining. Specifically, Giovanni Rossi, my roommate, Rohit Roopchand, the first person I met in Boston, Gianluca Paniz, my soccer mate, Boshra Nasr and Alejandra Bonifaz, my great neighbors. Also, thanks to all of you that have left Boston in the past couple of years but that still are here with your heart: Julian Volio, Charles Mark Vazzana, Rocio Chong, Ximena Montealegre, Alexis Vaughan, Amparo Pineda, Federico Penon, Alberto Bonilla, Gabriela Calderon, Charis Anastassiadou and many others that I surely forgot to mention but that are not for that reason less important.

Also, thanks to my boys in Rome for always keeping me informed on the life in the eternal city. Specifically: Marco Izzo, Massimiliano Brugia, Massimo Ratini, Leonardo Gaudio and Roberta Di Stano, grazie a tutti.

Special thanks also go to Silva Premoli for always being next to me in the good and in the bad moments. Always a source of comfort, joy and inspiration in my life. Alessia Gelosa, for your advice, your patience, and moral support.

Finally, I would like to thank my family who was always supportive in all aspects of my life. So far away physically yet so close emotionally. I would like to thank my father Giancarlo, my mother Gabriella, my brother Flavio, my sister Chiara and my brother in law Jacques. My thoughts also go to Sara and Paul, my niece and nephew, the joy and future of the family.

Lastly, I would like to acknowledge CenSSIS, the Center for Subsurface Sensing and Imaging Systems, under the Engineering Research Centers Program of the National Science Foundation (award number EEC-9986821) for their financial support.

PARAMETERS AFFECTING THE IMAGING AND DETECTION OF MICROBUBBLES IN BLOOD

PAOLO ZANETTI

ABSTRACT

Stabilized micron-sized bubbles, known as contrast agents, are often injected into the body to enhance ultrasound imaging of blood flow. The ability to detect such bubbles in blood depends on the relative magnitude of the acoustic power backscattered from the microbubbles (‘signal’) to the power backscattered from the red blood cells (‘noise’). Erythrocytes are acoustically small (Rayleigh regime), weak scatterers, and therefore the backscatter coefficient (BSC) of blood increases as the fourth power of frequency throughout the diagnostic frequency range. Microbubbles, on the other hand, are either resonant or super-resonant in the range 5-30 MHz. Above resonance, their total scattering cross-section remains constant with increasing frequency. In the present thesis, a theoretical model of the BSC of a suspension of red blood cells is presented and compared to the BSC of *Optison*® contrast agent microbubbles. It is predicted that, as the frequency increases, the BSC of red blood cell suspensions eventually exceeds the BSC of the strong scattering microbubbles, leading to a dramatic reduction in signal-to-noise ratio (SNR). This decrease in SNR with increasing frequency was also confirmed experimentally by use of an active cavitation detector for different concentrations of *Optison*® microbubbles in erythrocyte suspensions of different hematocrits. The magnitude of the observed decrease in SNR correlated well with theoretical predictions in most cases, except for very dense suspensions of red blood cells, where it is hypothesized that the close proximity of erythrocytes inhibits the acoustic response of the microbubbles.

Contents

List of Tables

List of Figures

List of Abbreviations

a = Radius (inner radius if two radii present)
a_n, b_n, c_n, C_n = Expansion coefficients
a_0 = Initial radius (inner radius if two radii present)
A = Vector displacement potential
A_b = Area of the bubble
ACD = Active cavitation detector
b = Outer radius
b_0 = Initial outer radius
BD = -3 dB beam diameter
BSC = Backscatter coefficient
BSC_{corr} = Corrected Backscatter coefficient
c = Velocity of sound
c_0 = Velocity of sound in a homogeneous medium
c_{1c} = Velocity of compressional waves in scatterer
c_{1s} = Velocity of shear waves in scatterer
c_2 = Velocity of sound in the fluid surrounding the scatterer
c_{rbc} = Velocity of sound in a single red blood cell
c_{sal} = Velocity of sound in isotonic saline
C_p = Heat capacity
d = Diameter of the cylindrical wire target
ds_e = Thickness of the shell
D = Element diameter of the transducer
E = Young’s modulus
f = Frequency
f_o = Resonant frequency
F = Focal length of the transducer
$g(\mathbf{r}, \mathbf{r_0})$ = Free space Green’s function
G_s = Stiffness of shell
$h_n^{(2)}$ = Hankel function of the second kind
H = Hematocrit
i = Imaginary number $(-1)^{1/2}$
I = Intensity
I_i = Incident intensity
I_0 = Initial intensity
$j_n(\ )$ = Spherical Bessel function of the first kind

$J_n(\ )$ = Bessel function of the first kind
k = Wavenumber (ω/c)
k_{1c} = ω/c_{1c}
k_{1s} = ω/c_{1s}
k_2 = ω/c_2
K_g = Thermal conductivity
l_D = Thermal diffusion length
L = Round-trip distance traveled by the sound wave
m = Effective mass of an oscillating bubble
n = Order integer
$n_n(\ )$ = Spherical Bessel function of the second kind
N = Number of measured voltages
$N_n(\ )$ = Bessel function of the second kind
p = Pressure
p' = Pressure perturbation
p_a = Driving acoustic pressure
p_A = Acoustic pressure amplitude
p_e = Equilibrium pressure inside the bubble
p_G = Gas pressure at equilibrium
p_H = Horizontal length of one pixel
p_i = Incident pressure field
p_L = Pressure in the liquid at the bubble surface
$P_n(\ )$ = Legendre polynomial
p_N = Number of pixels in the bubble image
p_0 = Hydrostatic pressure
P_0 = Initial pressure amplitude
p_s = Scattered pressure field
P_s = Scattered pressure amplitude
p_t = Total pressure
p_V = Vertical length of one pixel
p_∞ = $p_0 - p_a$
r, θ, z = Cylindrical coordinates
r, θ, ϕ = Spherical coordinates
$\mathbf{r}$ = Position vector to the observation point
$\mathbf{r_0}$ = Position vector within the volume (V)
R = Mechanical resistance of the bubble
R_c = Radiation resistance
$R_{\eta L}$ = Viscous resistance in the liquid
$R_{\eta s}$ = Viscous resistance of the shell
R_{th} = Thermal resistance
R_θ = Reflectivity
s = Spring constant
S_x = Standard deviation
$S_{\bar{x}}$ = Standard deviation of the mean
SNR = Signal-to-noise ratio
SNR_{avg} = Average signal-to-noise ratio
t = Time

$t_{v,p}$ = Student t-value for a given confidence interval
Δt = Round-trip time-of-flight
$\mathbf{u}$ = Displacement
$\mathbf{v}$ = Velocity
v_0 = Initial velocity
v' = Velocity perturbation
v_{rms} = RMS voltage
V = Volume
V_s = Initial volume of the shell ($b_0^3-a_0^3$)
W = Packing factor
x, y, z = Rectangular coordinates
x_{1c} = $k_{1c}a$
x_{1s} = $k_{1s}a$
x_2 = k_2a
y = Thickness
α, δ_d = Linear coefficients in the Church model
α_m, δ_{dm} = Non-linear coefficients in the Church model
$\alpha_n, \beta_n, \delta_n, \zeta_n, \eta_n$ = Scattering phase angles
α_{avg} = Average attenuation coefficient
α_I = Attenuation coefficient for intensity
α, α_A = Attenuation coefficient for amplitude
α_B = Attenuation coefficient for pure blood
α_{BB} = Attenuation coefficient for *Optison*® microbubbles in blood
α_{dB} = Attenuation coefficient in dB/cm
γ = Adiabatic constant
δ = Damping constant
δ_α = Precision uncertainty in attenuation
δ_A = Precision uncertainty in the area of the bubble
δ_c = Radiation damping
$\delta_{\eta L}$ = Viscous damping of liquid
$\delta_{\eta s}$ = Viscous damping of shell
δ_R = Precision uncertainty in the radius of the bubble
δ_{SNR} = Precision uncertainty in the SNR
δ_{th} = Thermal damping
δv_{rms} = Precision uncertainty of the rms voltage
ε_n = Neumann factor; $\varepsilon_0 = 1$; $\varepsilon_n = 2, n > 0$
η = Number density
η_n = Number density within a specific bin size
η_s = Viscosity of shell
η_L = Viscosity of liquid
κ = Polytropic exponent
κ_0 = Adiabatic compressibility
κ_1 = Compressibility of scatterer
κ_2 = Compressibility of the fluid surrounding the scatterer
λ, μ = Lamé elastic constants
λ_s = Elastic Lamé constant of the shell

ν = Poisson's ratio
ξ = Displacement in radial direction
Ξ = Velocity potential
Ξ_i = Incident velocity potential
Ξ_0 = Amplitude of incident wave
Ξ_s = Scattered velocity potential
Π_e = Scattered and absorbed power
Π_s = Scattered power
ρ = Density
ρ_0 = Density of fluid at rest
ρ_1 = Density of scatterer
ρ_2, ρ_L = Density of the fluid surrounding the scatterer
ρ_g = Density of the gas
ρ_s = Density of the shell
ρ' = Density perturbation
σ = Surface tension
σ_1 = Surface tension between the gas and the shell
σ_2 = Surface tension between the liquid and the shell
σ_d = Differential scattering cross-section
σ_e = Extinction cross-section
σ_s = Scattering cross-section
σ_r = Reduced scattering cross-section (non-dimensional)
σ_{dbs} = Differential backscattering cross-section
σ_n = Discretized differential backscattering cross-section
Φ_n = Boundary impedance scattering phase angle
Φ = Angular distribution function (form function)
Ψ = Scalar displacement potential
ω = Angular frequency
ω_0 = Angular resonance frequency
Ω = ω/ω_0
Ω_s = Solid angle

Chapter 1

Introduction

1.1 General Background

The use of high frequency sound waves as a diagnostic imaging tool has been a common practice since the 1970s and has seen constant evolvement and improvement since then, mainly due to its noninvasive nature, low cost, and ease of use. Ultrasound imaging devices have seen an increase in their complexity with a tendency to evolve towards smaller transducers, such as intra-vascular systems, and higher frequencies for better resolution.

Diagnostic ultrasound imaging is based upon the interpretation of echoes scattered from specific inhomogeneities within the tissue being investigated. A *pulse-echo* system usually consists of a transducer that transmits a short ultrasound pulse. The sound wave is, in part, absorbed by the medium and, in part, scattered in all directions by any object lying in its path. Part of the scattered signal is received either by the same transducer or by another transducer, making it possible to determine the distance of the object from the transducer, based on the time of travel and speed of sound in the medium.

Return echoes vary depending on the acoustic properties of the scatterer that is sampled (density and compressibility), allowing ultrasound scanners to create images of the examined region. Problems arise when the scatterer being investigated has very similar acoustic properties to the surrounding medium. In this case, the return echoes from the scatterer may be very weak, making them indistinguishable from the electrical noise produced by the imaging device itself. One such element in the realm of weak scattering, which demands special attention, is the red blood cell.

Imaging of blood is important in many applications, especially in the field of ultrasound imaging of the heart, also known as echocardiology. Unfortunately, scattering from blood is much weaker than that of other types of tissue, with amplitudes usually lower by 30-60 dB [73], creating the need for specific agents that can increase the amplitude of the scattered signal. The development of such agents, known as ultrasound contrast agents, began in the 1980's and usually consists of microbubbles stabilized by some kind of shell which prevents them from dissolving, therefore allowing them to persist throughout an ultrasound imaging treatment. The first agent to be approved was *Echovist®*, (Schering AG, Germany) developed in 1991, consisting of sugar crystals that dissolve in blood and liberate air [73], followed by *Albunex®* (Molecular Biosystems Inc., CA) in 1993, consisting of air-filled encapsulated microbubbles stabilized by surface layers of human serum albumin [62]. A photograph of *Optison®* (Mallinckrodt, MO), an FDA-approved, clinically utilized contrast agent is given in Figure 1.1. Similarly to *Albunex®*, *Optison®* is a suspension of human serum albumin microspheres containing octafluoropropane (C_3F_8) instead of air [70].

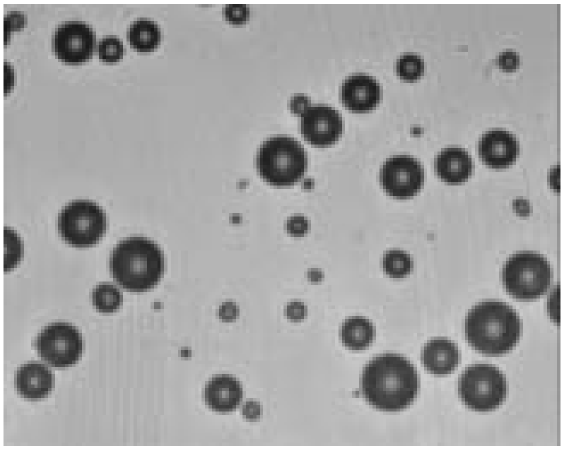

Figure 1.1 Image of a suspension of *Optison®* contrast agents in isotonic saline taken with a 40x microscope. The field of view measures 55x45 µm.

Microbubbles are an obvious choice as ultrasound contrast agents because they are strong scatterers. Scattering from bubbles has been a very important research topic in underwater acoustics, dating back to studies performed by Lord Rayleigh in 1872 [1, 2] and Minnaert in 1933 [3]. Both Rayleigh and Minnaert looked at a phenomenon called cavitation, commonly and loosely defined as the formation of gas bubbles in a liquid. It was shown, that when subjected to an acoustic field, among other things, bubbles are driven into oscillations. If the amplitude of these oscillations is small, the bubble may be modeled as a linear harmonic oscillator [3]. If driven at higher amplitudes or specific frequencies, the bubble motion may become very nonlinear, resulting in additional frequency components in the bubble response.

Free, linear oscillating bubbles were first investigated by Minnaert [3] who derived an equation for the resonance frequency of a spherical gas bubble in a liquid, ignoring surface tension. This frequency is now known as the Minnaert frequency (f_0) and is given by

$$f_0 = \frac{1}{2\pi a}\sqrt{\frac{3\kappa P_o}{\rho_L}} \tag{1.1}$$

where a is the radius of the bubble, κ is the polytropic exponent of the gas, P_0 is the equilibrium pressure inside the bubble, and ρ_L is the density of the liquid surrounding the bubble. At the resonance frequency, the response of the bubble is greatly enhanced, as can be seen from Figure 1.2, but beyond this point the bubble behaves like a geometric scatterer, hence like a rigid sphere. Ignoring surface tension, for bubbles in water greater than about 10 μm in diameter, the resonance frequency is inversely proportional to the bubble radius. Therefore, for an air bubble in water at standard temperature and pressure (273° K and 101 kPa) the product of the resonance frequency and the bubble radius can be computed as $f_0 a = 3.25$ Hz·m. Due to this simple proportionality between the resonance frequency and the radius of a bubble, one may also define a resonance size, corresponding to the radius of a resonating bubble given a particular insonifying frequency. A complete overview of the behavior of oscillating bubbles is given in Leighton [61].

Contrast agents being "special" bubbles, namely free bubbles with the addition of a surface layer surrounding them for stabilization purposes, have been an ever growing area of interest, especially to determine the effect that the shell may have on the behavior of the bubble when insonified by an ultrasound pulse. Studies in this direction have been performed by de Jong et al. [57], de Jong and Hoff [58], Church [62], Allen [71], and Ye [64]. A good overview of contrast agent characterization is given by Hoff [73].

The appearance of bubbles in medical diagnostic ultrasound is not exclusively due to contrast agents. Acoustic cavitation, namely the formation or driven pulsation of a bubble in response to an applied acoustic field, has been an ever growing cause of concern long before the advent of contrast agents. A phenomenon known as inertial cavitation, consisting in the unstable growth and violent collapse of a bubble, has been proven to produce deleterious bioeffects to human tissue. In this case, the motion of the bubble is dominated by the inertia of the liquid, hence the name "inertial". Concern over the existence of inertial cavitation has became of such importance that the Food and Drug Administration adopted an ad hoc index, namely the Mechanical Index (MI), that predicts the likelihood that a scanner operating at a specific pressure and frequency will produce inertial cavitation. The MI assumes the a priori existence of small microbubbles that act as sites for inertial cavitation inception. Thus, it is a particularly conservative indicator of the likelihood of generating inertial cavitation. Studies on the effects of acoustic cavitation have been extensively performed and will not be referenced in the present work. A good review of such effects is given in a special issue of the *Journal of Ultrasound in Medicine, Volume 19, February 2000*, dedicated entirely to the topic [67]. The concern over possible bioeffects has therefore created the important need for determining the presence of cavitating microbubbles.

Recent advances in ultrasound transducer technology have made it possible to produce ultrasound of increasingly high frequencies. Higher frequencies imply a smaller wavelength of the acoustic pulse being sent through the region investigated, which translates to a better imaging resolution. However, increasing the imaging frequency may produce a rather remarkable and unexpected result when imaging microbubbles of resonance or super-resonance size, such as contrast agents, in blood. The backscatter coefficient (BSC), defined as the power scattered in the backward direction (180^0 relative to the incident pulse) per unit incident intensity, per unit volume, per unit solid angle (see Sec. 3.1), of weak scatterers, such as red blood cells, increases as the fourth power of frequency, while the BSC of super-resonant microbubbles remains relatively constant, since they behave as geometric scatterers. At commonly used diagnostic frequencies (1 – 5 MHz) this effect is irrelevant since contrast agent microbubbles are designed for optimal response in this frequency range, and therefore, the BSC of the microbubbles is much higher than that of the red blood cells. However, as the detection frequency is increased beyond 5MHz, the scattering from the red blood cells may approach that of the microbubbles, diminishing, in the case of contrast agents, their image enhancement effect. Figure 1.2 shows a theoretical calculation of such an effect, clearly showing how the return from the red blood cells starts "catching up" with the return from the microbubble contrast agents, which become super-resonant for frequencies greater than 10 MHz. Similarly, when detecting cavitation in blood, at high frequencies, the signal from the red blood cells might shadow that from the cavitating bubbles, inhibiting the ability to detect them.

Therefore, it is important to investigate what exactly happens when imaging frequencies of 5MHz and above are used for imaging blood with contrast agents, or for detecting microbubbles in blood. What are the important parameters that affect imaging apart from the detection frequency? Is the concentration of bubbles and the concentration of the red blood cells important? The present study will try to answer such questions with the use of experimental data and theoretical modeling.

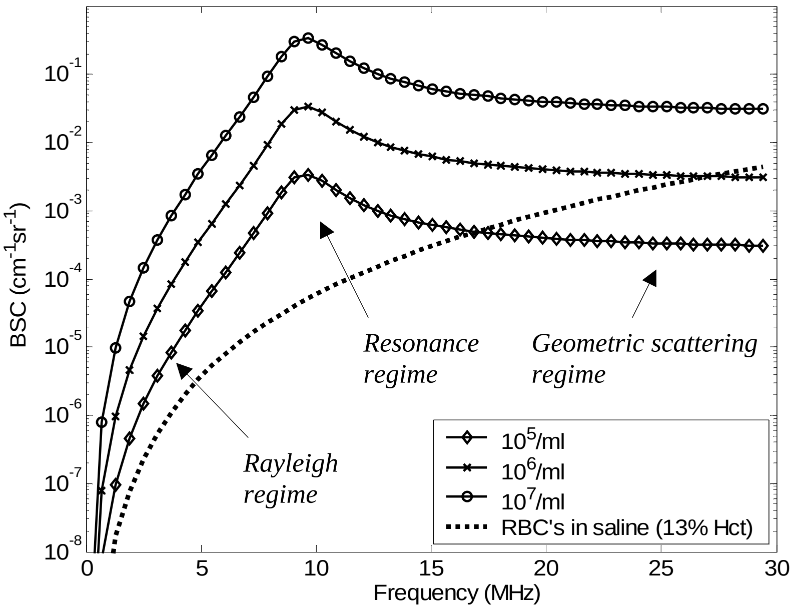

Figure 1.2 Backscatter coefficient for a suspension of different concentrations of 1 μm diameter air bubbles as a function of frequency compared to that of a suspension of red blood cells (RBC's) at 13% hematocrit. The plots are based on models developed in Chapter 2 and Chapter 3. Also shown are the three regimes for scattering from microbubbles: Rayleigh regime, resonance regime, and geometric scattering regime.

The purpose of this research is therefore to investigate the scattering from red blood cells and the scattering from microbubbles in order to determine how the relative magnitude of the two phenomena varies with acoustic frequency, taking into account other parameters such as hematocrit (the volume fraction of red blood cells to plasma in blood, usually at about 45-50% at human physiological levels), and the concentration and size distribution of microbubbles. The process will involve both the collection of experimental data with the use of an Active Cavitation Detector (ACD), described in Sec.1.2.2, as well as the development of theoretical formulations from a number of investigators.

The next subsections will therefore be dedicated to introducing the work previously performed by various researchers on scattering from red blood cells as well as the development of the apparatus used for the present work, namely the ACD.

1.2 A Brief History

1.2.1 Ultrasound scattering from blood

Blood is made of a suspension of red cells, white cells and platelets in plasma, each accounting for approximately 40-47%, 1%, and 0.3% of the total volume respectively [18]. Red cells, also known as erythrocytes, are the main contributors to blood's mechanical properties and their role is the transport of oxygen through the blood stream [23]. They are shaped like biconcave disks with no nucleus and are surrounded by a 7.5 nm thick membrane. Their mean cell volume is about 87 μm^3, which consists of mainly water and hemoglobin [18]. An illustration of a suspension of red blood cells is given in Figure 1.3. As previously mentioned, red blood cells scatter sound very weakly, because their acoustic properties are very similar to those of plasma: there is less than a 7% difference in compressibility and a 10% difference in density between plasma red blood cells [72].

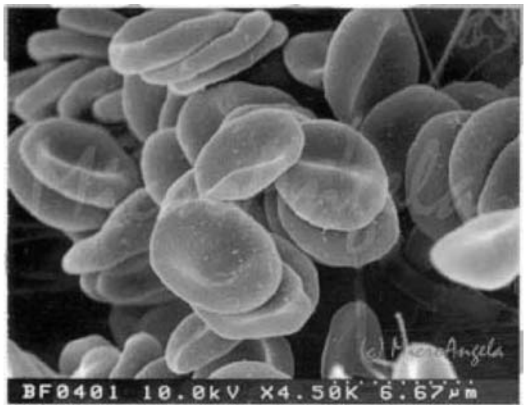

Figure 1.3 Illustration of a suspension of red blood cells in plasma obtained from T.W. Carvalho, *Microangela*, http://www.pbrc.hawaii.edu, 2000

A great deal of *in vitro* experimental measurements have been performed over the course of the previous five decades to study ultrasound scattering from blood. Carstensen et al. [10] in 1953 were the first to measure sound velocity and absorption through blood by using residues from centrifuged human blood at 85% hematocrit and diluting them with plasma. Results seemed to indicate nearly-linear relationship between absorption and frequency at different hematocrits and between absorption and hematocrit at different frequencies (0.8, 1.2, and 2.4 MHz).

In 1976, Shung et al. [27] used an immersion transducer and a latex chamber containing a suspension of red blood cells to determine the backscattering coefficient (BSC) of blood. The transducer generated a small sine-wave burst, which was scattered from the red blood cells and received by the same transducer. This experiment was performed at a sufficiently low pulse repetition frequency for the reflections from the blood and those from the latex and tank interfaces to be distinguishable. The backscatter coefficient was determined following a standard method developed by Siegelmann et al. [25] in which the power backscattered by the blood was compared to that from a planar target of known reflection coefficient. The BSC for a suspension of red blood cells was determined as a function of hematocrit at three different frequencies (5, 8.5, and 15 MHz). It was shown to exhibit a steady increase up to a region between 15% and 20% hematocrit, a leveling between 20% and 30% hematocrit, and then a decrease beyond that point.

In 1988, Yuan and Shung [48] published measurements of the attenuation and backscatter coefficients of suspensions of red blood cells as a function of frequency in the range 3.5-12.5 MHz at three different hematocrits (8%, 23%, 44 %). Attenuation, in dB/cm, was found to increase linearly with hematocrit and frequency, while the BSC was shown to increase as the fourth power of frequency. In a subsequent study, Wang and Shung [65] repeated the experiment for frequencies up to 30MHz, showing the same dependence of the attenuation and backscatter coefficients on frequency and hematocrit. In 2002 Maruvada et al. [75] extended the previous experiments to higher frequencies in the range 30-90 MHz, showing that the frequency dependence applies up to 90 MHz for low hematocrits (up to 15%), and up to 30MHz for higher hematocrits.

Important studies on the acoustic characterization of red blood cells were also performed by Roy [43], who used scattered echoes , detected at two different angles, from individual red blood cells to calculate their acoustic properties. In 2001, Coussios [72] used similar acoustic techniques to monitor the extent of hemolysis (the destruction of red blood cells) of human red blood cells in a closed artificial circuit.

1.2.2 Detection of microbubbles and the ACD

The need for detecting and imaging microbubbles came about with the discovery that ultrasound-induced transient or inertial cavitation was a major cause of deleterious bioeffects in human tissue. Until the 1980's, it was believed that inertial cavitation could not occur at the typical frequencies of diagnostic imaging devices, mainly because the short pulses of ultrasound sent out by these devices would not allow enough time for the bubble to grow. A breakthrough occurred in 1982, when independent studies by Apfel [36] and Flynn [37] demonstrated that such an event was possible, in timescales of the order of microseconds, provided that there was a sufficient acoustic stress. This result led the research community to explore the non-trivial task of detecting such short-lived events, with the development of very sensitive techniques for measuring acoustic scattering.

The two main setups that have been developed to detect cavitation *in vitro* are the *passive cavitation detector* (PCD), and the *active cavitation detector* (ACD) both of which rely on scattering from the cavitation bubbles. The PCD was first developed by Atchley and Frizzell [44] and usually consists of a focused detection transducer which passively “listens” and picks up the scattered signal from the cavitation event. This technique was found to be very efficient when the incident pulse of the diagnostic transducer is relatively long (longer than 3 acoustic cycles) but was not sensitive enough for shorter pulses. In 1987 Roy [43] and in 1990 Roy and Madanshetty [52] developed the ACD, which consists of a high-frequency, narrowband, pulse-echo device that probes the cavitation zone, as shown schematically in Figure 1.4. The tight focusing and high excitation frequency of the ACD not only adds sensitivity, but provides both spatial and temporal resolution to the detection measurements. The ACD was effectively used in various experimental investigations by Crum et al. [55], Madanshetty et al. [54], Holland et al. [56], and Huertas et al. [60].

In the present study, an ACD was constructed and used at four different detection frequencies (5, 15, 25, 30 MHz) for measuring the backscattered signal from numerous scattering targets in addition to suspensions of red blood cells in saline, and suspensions of microbubbles in blood and saline. Chapter 4 will explain in detail the development of this device as well as the experimental setup as a whole. The extremely high sensitivity of the ACD results in a very high signal-to-noise ratio, thereby allowing the detection of even the smallest and weakest of scatterers. Such high detection capabilities are crucial when observing the backscatter from weak scatterers such as red blood cells, especially at the lower frequencies.

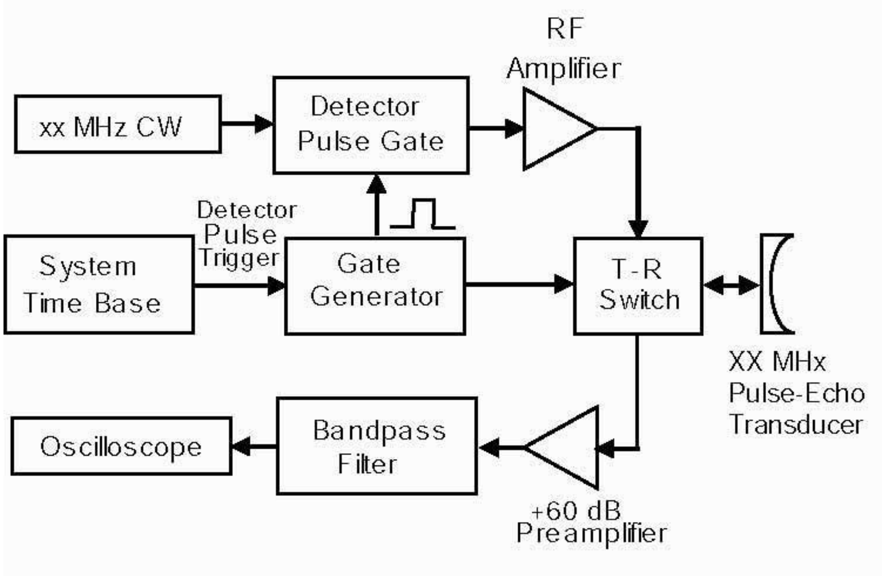

Figure 1.4 Schematic of the active cavitation detector developed by Roy [43], used as the main element of the experimental setup for the current investigation.

1.3 Overview and Motivations

1.3.1 The Roy and Fowlkes experiment

In 1994 Roy and Fowlkes performed an experiment involving the detection of microbubbles in a flow with the use of an ACD. The experiment consisted of a 1.8-MHz high-intensity focused ultrasound (HIFU) source that generated microbubbles (via cavitation) in both water and blood, which were kept in constant circulation with a peristaltic pump. The bubbles traveled with the host fluid until they reached the focus of the 30 MHz ACD, where they were detected and displayed by an oscilloscope [79]. The experimental setup of this experiment is displayed in Figure 1.5.

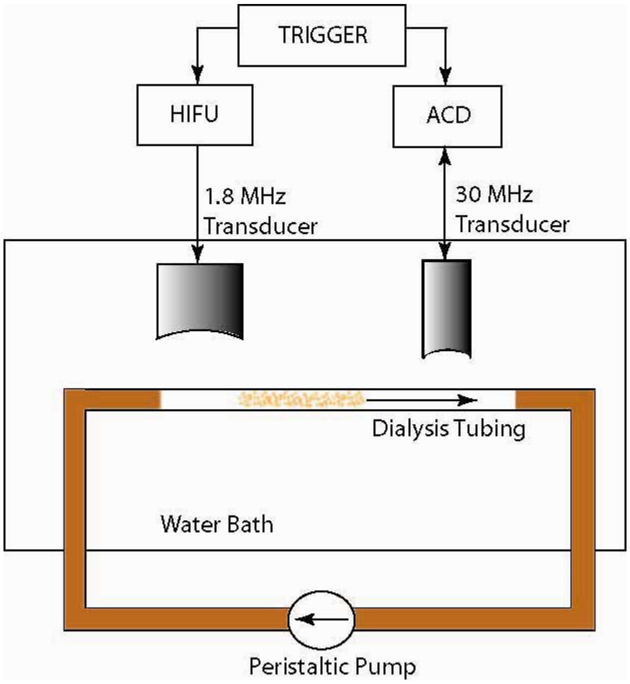

Figure 1.5 Setup of the experiment performed by Roy and Fowlkes for detecting HIFU-generated cavitation in a dialysis tubing flow loop with an active cavitation detector.

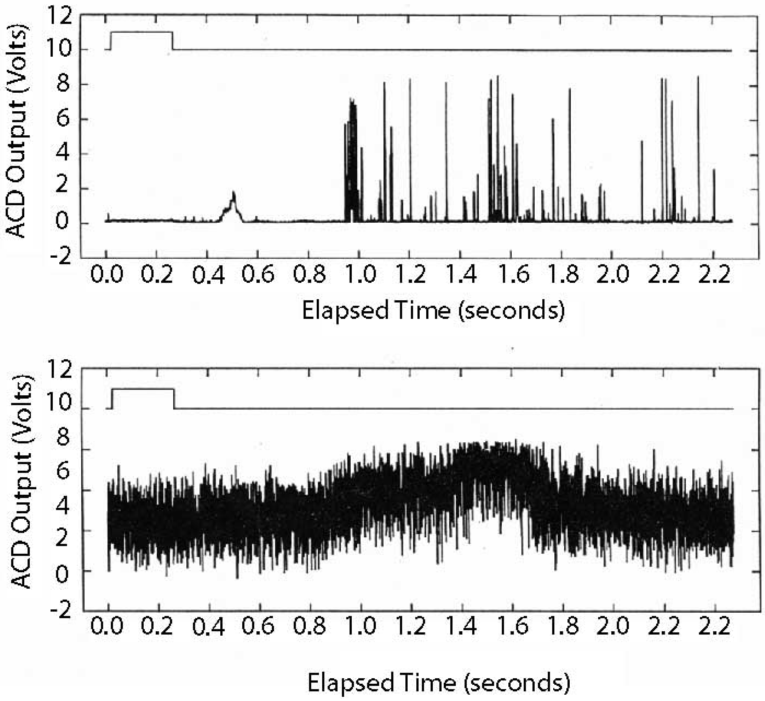

Figure 1.6 ACD output of the experiment performed by Roy and Fowlkes for detecting HIFU-generated cavitation in a dialysis tubing flow loop. Top plot displays the scattering in water and the bottom plot displays the scattering in blood.

The displayed output given in Figure 1.6 was remarkable. When the host fluid was plain water, the cavitation events were clearly visible. On the other hand, when the host fluid was blood, the return from the microbubbles was completely shadowed by the signal from the suspension of red blood cells. In <u>both</u> cases, the microbubbles were readily observable using a standard diagnostic imager (ATL Ultramark 8, 5 MHz sector scanner).

Roy and Fowlkes therefore observed that, at 30 MHz, the “weak” signal scattered from the red-blood cells became significant, even in the presence of strong scatterers such as microbubbles. This observation created a need for further investigation of the obscuring of the signal from the bubbles by the red blood cells as a function of frequency, as well as the absolute and relative concentrations of weak and strong scatterers. In the present clinical context of utilizing higher and higher imaging frequencies so as to achieve better image resolution, it is believed that developing a better understanding of the contribution of weak scatterers to the overall backscattered signal is particularly important.

1.3.2 Overview of experiments

Given the importance of identifying how an increase in imaging frequency will affect the scattering of very “strong” scatterers such as microbubbles in the presence of “weak” scatterers such as red blood cells, the decision was made to implement an active cavitation detector (ACD) to investigate such a phenomenon. All experiments were performed at 4 insonifying frequencies, 5, 15, 25, and 30 MHz using focused transducers. The goal will therefore be to show how the power backscattered by a strong target or a suspension of targets, such as microbubbles (“signal”), compares to the power backscattered by a suspension of weak scatterers, such as red blood cells (“noise”), as a function of frequency, and how hematocrit and microbubble concentration affect the results. A formulation called the signal-to-noise ratio (SNR) was therefore implemented (see Chapter 3) allowing to compare the backscattered returns from the two populations of scatters.

In order to prove the initial concept of a decrease in the SNR for a strong scatterer immersed in a suspension of weak scatterers with increasing imaging frequency, the first experiment performed was to immerse a 35 μm fiberglass wire and a 25 μm tungsten wire, also strong scatterers, in a suspension of red blood cells. The SNR was computed for all four frequencies at 13% hematocrit (which happens to be the value that provides the strongest scattering, explained in Sec. 3.1.1). The wire was chosen for the simple geometry (cylinder), straightforward theoretical modeling, availability, and ease of mounting, and was also used to measure the attenuation coefficient in blood as a function of frequency and hematocrit (3.5%, 12.5%, 20%, 30%, 40%, and 50%).

The next step consisted in using different concentrations of microbubbles in blood ($6.5\text{x}10^4$ microbubbles/ml and $6.5\text{x}10^5$ microbubbles/ml) at different hematocrits (1% and 45%) and measuring the resulting SNR. The microbubble contrast agent *Optison®* was employed for the scattering from microbubbles and the concentrations were chosen to mimic clinical dosages. The attenuation coefficient was also obtained for blood and Optison® and compared to that of just blood. All experimental results of the SNR were then compared to theoretical modeling formulations developed in Chapter 2 and 3.

1.4 Recapitulation and Outline of Thesis

The main objective of the present study is to investigate how the relative magnitude of the scattered signal from a strong scatterer (in particular microbubbles) and that of a suspension of red blood cells varies as a function of frequency in the 5-30 MHz range, hematocrit, and bubble concentration.

The present document will therefore begin with an explanation of the single-particle scattering theory needed to model the return from a red blood cell, a sphere, an elastic cylinder, and a contrast agent microbubble explained in Chapter 2. Chapter 3 will consider collections of scatterers and adjust the solutions for the single-particle models to illustrate how suspensions of red blood cells and suspensions of microbubbles scatter sound. A formulation of how the BSC changes as a function of red blood cell concentration and as a function of frequency will be developed. Next, a derivation of the SNR for an elastic cylinder in blood and for *Optison*® microbubbles in blood will be introduced and relevant examples will be discussed. The next step will be to introduce the experimental setup and procedures performed for this study in detail, with a thorough explanation of the functioning of the ACD in Chapter 4. This will include illustrations of the electronics and the tank assembly, in addition to detailed procedures for all the experiments performed and for the preparation of red blood cell suspensions. Finally, results will be presented in Chapter 5, including the attenuation through red blood cells as a function of frequency and hematocrit, attenuation through red blood cells with the addition of *Optison*® microbubble contrast agents, the SNR of a rigid cylindrical wire target in blood, and the SNR of microbubbles in blood. A brief discussion will follow each result with explanations of both the qualitative behavior and the quantitative outcome of the experimental results. Lastly, the final conclusions will be given in Chapter 6 with suggestions for future work.

Chapter 2

Scattering Theory

Three main problems were investigated during the course of this project, as outlined in the introduction: (1) the observability of the return signal or backscatter from a single, discrete, well-defined strong scatterer in a suspension of red blood cells, (2) the observability of the return signal from a suspension of contrast agent microbubbles in a suspension of red blood cells, and (3) the determination of the attenuation of sound in a suspension of solely red blood cells and red blood cells with the addition of a contrast agent. The theoretical modeling of such problems, therefore, mainly consisted in investigating different acoustic scattering models, developed by several investigators over the course of the last century.

The target used in the experimental setup (see Chapter 4) was either a sphere or a cylinder made of materials such as fiberglass and tungsten. Models of the scattering from such geometries were developed by Faran [8] in 1951 with the solution for the elastic sphere and cylinder, as well as Hickling [14], Doolittle and Überall [19], Hay and Burling [38], and Neubauer [42]. Similarly, individual *Optison*® microbubbles can be modeled as spherical shells, using the scattering models developed by Hasegawa et al. [45], Zhen Ye [64] and Allen [71]. Another approach consists of viewing each contrast agent particle as an oscillating gas bubble, with the addition of a damping term accounting for the effect of the surface layer surrounding the bubble, as done by de Jong et al. [57], de Jong and Hoff [58] and Church in [62]. Finally, individual red blood cells can be modeled as spherical fluid scatterers, either by using the exact solution developed by Anderson [6], or by making use of the Rayleigh (long wavelength) [1] or Born (weak scatter) approximations [21].

The next section provides a general overview of sound propagation in a homogeneous medium. Scattering models for spheres, cylinders, and spherical shells are described in the subsequent sections, with specific examples applied to red blood cells and contrast agents. The bubble dynamics model developed by Church [62] for a viscoelastic spherical shell is also described. Solutions are compared and validated against previously published results. This chapter deals exclusively with single-particle scattering models. The problem of scattering and attenuation by *collections* of particles, be they red blood cells or microbubbles, is treated in Chapter 3.

2.1 Sound Propagation in a Homogeneous Medium

A brief introduction to the governing equations for the propagation of a sound wave in a homogeneous medium will follow below. Such equations will lead to the derivation of the homogenous wave equation. Scattering in an inhomogeneous medium will follow in the next sections with inhomogeneities of specific geometries.

In order to completely describe the propagation of sound in a homogeneous medium one needs to satisfy two conservation laws, mass and momentum, as well as determine the equation of state relating the acoustic pressure to the density. From these three equations, one can then derive the homogeneous wave equation.

For an isotropic fluid of density ρ moving at velocity ***v***, the equation of continuity (conservation of mass) in three dimensions takes the form

$$\frac{\partial \rho}{\partial t} + \nabla \cdot \rho \mathbf{v} = 0 \; . \tag{2.1}$$

In the absence of external forces and neglecting viscosity, the Euler equation (conservation of momentum) can be written as

$$\rho \left[\frac{\partial \mathbf{v}}{\partial t} + \mathbf{v} \cdot \nabla \mathbf{v} \right] + \nabla p = 0 \; , \tag{2.2}$$

where p designates the pressure. When a fluid, initially at rest, of density ρ_0 and at pressure p_0 is perturbed by a sound wave, the density, velocity and pressure at position ***x*** and time t are given by $\rho(\mathbf{x},t)=\rho_0+\rho'(\mathbf{x},t)$, $v(\mathbf{x},t)=v'(\mathbf{x},t)$ and $p(\mathbf{x},t)=p_0+p'(\mathbf{x},t)$, where ρ', v', and p' are small. This gives

$$\frac{\rho - \rho_0}{\rho_0} \ll 1, \quad \frac{p - p_0}{p_0} \ll 1 \text{ and } \mathbf{v} \cdot \nabla \mathbf{v} \ll \frac{\partial \mathbf{v}}{\partial t} \, . \tag{2.3}$$

The continuity equation (Eq. (2.1)) can therefore be written as

$$\frac{\partial \left(\rho_0 + \rho'(\mathbf{x},t) \right)}{\partial t} + \nabla \cdot \left(\left(\rho_0 + \rho'(\mathbf{x},t) \right) \mathbf{v}'(\mathbf{x},t) \right) \tag{2.4}$$

and the Euler equation (Eq. (2.2)) takes the form

$$\left(\rho_0 + \rho'(\mathbf{x},t) \right) \left(\frac{\partial \mathbf{v}'(\mathbf{x},t)}{\partial t} + \mathbf{v}'(\mathbf{x},t) \cdot \nabla \mathbf{v}'(\mathbf{x},t) \right) + \nabla \left(p_0 + p'(\mathbf{x},t) \right) = 0 \tag{2.5}$$

Neglecting second order terms, Eqs. (2.4) and (2.5) can be simplified as

$$\frac{\partial \rho'(\mathbf{x},t)}{\partial t} + \rho_0 \nabla \cdot \mathbf{v}'(\mathbf{x},t) = 0 \tag{2.6}$$

$$\rho_0(\mathbf{x},t) \frac{\partial \mathbf{v}'(\mathbf{x},t)}{\partial t} + \nabla p'(\mathbf{x},t) = 0. \tag{2.7}$$

Eqs. (2.6) and (2.7) are also known as the linearized continuity equation and the linearized Euler equation.

The last equation needed for the description of sound propagation in a homogeneous medium is the equation of state. This type of equation usually relates one of the state variables, such as pressure, density or entropy, to the other two. If one considers an adiabatic compressible fluid, the density ρ is a function of pressure only, i.e. $\rho=\rho(p)$. The density fluctuations, ρ', about a mean value, ρ_0, can then be written as a Taylor series expansion in the fluctuations about the mean pressure, p', as:

$$\rho' = \frac{\partial \rho}{\partial p} p' + \frac{\partial^2 \rho}{\partial p^2} \frac{p'^2}{2} + \ldots \tag{2.8}$$

Neglecting second order terms and using the first order term in Eq. (2.8) to define the adiabatic compressibility κ_0, we can write

$$\rho' = \frac{\partial \rho}{\partial p} p' = \kappa_0 \rho_0 p' \tag{2.9}$$

The above equation can then be rewritten in terms of the speed of sound (c_0) as:

$$\rho' = \frac{1}{{c_0}^2} p' \tag{2.10}$$

Using Eqs. (2.6), (2.7), (2.9), and (2.10) the homogeneous wave equation can be derived. This is done by differentiating Eq. (2.6), taking the divergence of Eq. (2.7), and inserting Eq. (2.10) for the density. Dropping the primes for simplicity, the wave equation can be written as:

$$\nabla^2 p(\mathbf{x},t) - \rho_o \kappa_0 \frac{\partial^2 p(\mathbf{x},t)}{\partial t^2} = \nabla^2 p(\mathbf{x},t) - \frac{1}{{c_0}^2} \frac{\partial^2 p(\mathbf{x},t)}{\partial t^2} = 0 \tag{2.11}$$

Equation (2.11) can be solved and used to describe the behavior of a sound wave propagating through a homogeneous medium. The following sections will shift attention to solutions for specific scattering problems, which describe examples of sound waves encountering inhomogeneities of well-known geometries such as spheres and cylinders.

2.2 Ultrasound Scattering from Spheres

Sound scattering from spheres has been one of the most popular and extensively treated problems in the realm of acoustic scattering, mainly due to the geometric simplicity of a spherical object. Several exact and approximate solutions have been developed by various authors and will be introduced in the following sections. Most of the solutions presented are cast in the form of normal mode expansions and are best evaluated numerically.

The exact solution for scattering from an elastic sphere is first derived. This problem was initially investigated by Faran [8], and later by Hickling [14, 15] and Hay and Burling [38], who introduced viscous and thermal effects that will not be considered here. The exact solution developed by Anderson [6] for scattering from a fluid sphere is then presented, since it will be used later to model scattering by a red blood cell. Particular attention will be given to the case where the sphere is much smaller than the wavelength, known as the Rayleigh approximation [1, 22], and to the case where the density and compressibility of the scatterer are very similar to those of the surrounding medium, giving rise to the Born approximation [21]. The specific case of scattering from a red blood cell will be investigated by performing a comparison between the Anderson, Faran, Rayleigh approximation and Born approximation solutions.

2.2.1 The elastic sphere – an exact solution

The derivation outlined below follows that of Faran [8] and utilizes the coordinate system shown in Figure 2.1. A harmonic plane wave of frequency ω, traveling in the positive z-direction, impinges upon a sphere made of a homogenous, isotropic material . The goal is to determine the amplitude of the scattered wave at large distances from the sphere. All material properties of the spherical scatterer are denoted by the subscript 1, while the properties of the surrounding medium are denoted by the subscript 2.

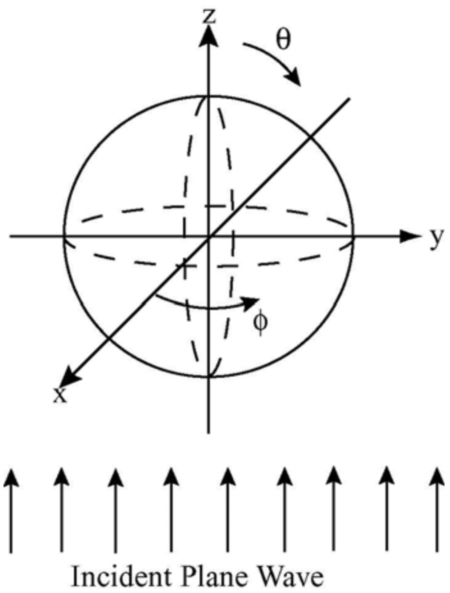

Figure 2.1 The coordinate axis for the scattering by spheres (Faran [8]).

One can first transfer to spherical coordinates by applying the following transformations:

$$x = r\sin\theta\cos\phi \quad y = r\sin\theta\sin\phi \quad z = r\cos\theta \tag{2.12}$$

The next step is to determine mathematical expressions for the displacement and pressure, both inside and outside the sphere. Starting with the inside of the sphere, one may represent solutions of the equation of motion of a solid elastic medium with Lamé constants λ and μ, density ρ_1, and displacement $\boldsymbol{u}$ by [31]:

$$(\lambda + 2\mu)\nabla(\nabla\cdot\mathbf{u}) - \mu\nabla\times(\nabla\times\mathbf{u}) = \rho_1\frac{\partial^2\mathbf{u}}{\partial t^2}\,. \tag{2.13}$$

Equation (2.13) above then leads to two independent wave equations,

$$\nabla^2(\nabla\cdot\mathbf{u}) = \left(\frac{\rho_1}{\lambda} + 2\mu\right)\frac{\partial^2(\nabla\cdot\mathbf{u})}{\partial t^2} \tag{2.14}$$

$$\nabla^2(\nabla\times\mathbf{u}) = \left(\frac{\rho_1}{\mu}\right)\frac{\partial^2(\nabla\times\mathbf{u})}{\partial t^2}, \tag{2.15}$$

which can be used to define the compressional (c_{1c}) and shear (c_{1s}) wave velocities in terms of the Lamé constants (λ and μ) of the sphere or, equivalently, of its Young's modulus (E) and Poisson's ratio (ν):

$$c_{1c} = \left[\frac{(\lambda + 2\mu)}{\rho_1} \right]^{\frac{1}{2}} = \left[E \frac{(1-\nu)}{\rho_1 (1+\nu)(1-2\nu)} \right]^{\frac{1}{2}} \tag{2.16}$$

$$c_{1s} = \left(\frac{\mu}{\rho_1} \right)^{\frac{1}{2}} = \left[\frac{E}{2\rho_1 (1+\nu)} \right]^{\frac{1}{2}} . \tag{2.17}$$

In order to determine the solution for Eq. (2.13), one can define the displacement in terms of a scalar and vector potential given by

$$\mathbf{u} = -\nabla\Psi + \nabla \times A \, . \tag{2.18}$$

Equation (2.18) can therefore be viewed as the sum of the displacements associated with both the compressional and shear waves. The potentials in Eq. (2.18) above satisfy the following wave equations,

$$\nabla^2 \Psi = \left(\frac{1}{{c_{1c}}^2} \right) \frac{\partial^2 \Psi}{\partial t^2} \tag{2.19}$$

$$\nabla^2 A = \left(\frac{1}{{c_{1s}}^2} \right) \frac{\partial^2 A}{\partial t^2} \, . \tag{2.20}$$

After taking into account the change in coordinates given in Eq. (2.12), one can determine solutions for the potentials given as

$$\Psi = \sum_{n=0}^{\infty} a_n j_n (k_{1c} r) P_n (\cos\theta) \tag{2.21}$$

$$A = \sum_{n=0}^{\infty} b_n j_n (k_{1s} r) \frac{\partial}{\partial\theta} P_n (\cos\theta) , \tag{2.22}$$

where j_n is the spherical Bessel function of the first kind and $P_n(\cos\ \theta)$ is the Legendre polynomial.

Expressions for the incident and scattered pressure fields with initial pressure amplitude P_0 are given by Faran [8] in the form

$$p_i = P_o \sum_{n=0}^{\infty} (2n+1)(-i)^n\ j_n\left(k_2 r\right) P_n\left(\cos\theta\right) \tag{2.23}$$

$$p_s = P_o \sum_{n=0}^{\infty} c_n \left[j_n\left(k_2 r\right) - i n_n\left(k_2 r\right)\right] P_n\left(\cos\theta\right), \tag{2.24}$$

where n_n is the spherical Bessel function of the second kind or Neumann function. The applicable boundary conditions are: (i) the pressure in the fluid is equal to the normal component of the stress at the solid interface; (ii) the radial component of the displacement of the fluid equals the normal component of the displacement of the solid interface; (iii) the tangential component of the shearing stress is equal to zero at the surface of the solid. After applying these boundary conditions, the expansion coefficient c_n is found to be of the form

$$c_n = -P_0\left(2n+1\right)(-i)^{n+1} \sin\eta_n \exp\left(i\eta_n\right), \tag{2.25}$$

where η_n is the phase shift of the n^{th} scattered wave, given by the expression

$$\tan\eta_n = \tan\delta_n\left(x_2\right) \frac{\left[\tan\Phi_n + \tan\alpha_n\left(x_2\right)\right]}{\tan\Phi_n + \tan\beta_n\left(x_2\right)}\ , \tag{2.26}$$

and

$$\begin{aligned} x_{1c} &= k_{1c} a \\ x_{1s} &= k_{1s} a \\ x_2 &= k_2 a \end{aligned} \tag{2.27}$$

$$\begin{aligned}
\delta_n(x) &= \tan^{-1}\left[\frac{-j_n(x)}{n_n(x)}\right] \\
\alpha_n(x) &= \tan^{-1}\left[\frac{-xj_n^{'}(x)}{j_n(x)}\right] \\
\beta_n(x) &= \tan^{-1}\left[\frac{-xn_n^{'}(x)}{n_n(x)}\right] \; .
\end{aligned} \tag{2.28}$$

The quantities, k_{1c}, k_{1s} and k_2 denote the compressional wavenumber in the scatterer, the shear wavenumber in the scatterer, and the compressional wavenumber in the fluid outside the scatterer. In addition, the impedance phase-angle Φ_n must be determined to complete the derivation of the phase shift η_n. This impedance phase-angle Φ_n contains the material properties of the sphere and is given by the expression:

$$\tan\Phi_n = -\left(\frac{\rho_2}{\rho_{1c}}\right)\tan\zeta_n\left(x_{1c},\nu\right) \tag{2.29}$$

where,

$$\zeta_n\left(x_{1c},\nu\right) = \tan^{-1}\left[-\frac{x_{1s}}{2}\,\frac{\dfrac{\tan\alpha_n\left(x_{1c}\right)}{\tan\alpha_n\left(x_{1c}\right)+1} - \dfrac{n^2+n}{n^2+n-1-\frac{1}{2}x_{1s}^{\;2}+\tan\alpha_n\left(x_{1s}\right)}}{\dfrac{n^2+n-\frac{1}{2}x_{1s}^{\;2}+2\tan\alpha_n\left(x_{1c}\right)}{\tan\alpha_n\left(x_{1c}\right)+1} - \dfrac{\left(n^2+n\right)\left[\tan\alpha_n\left(x_{1s}\right)+1\right]}{n^2+n-1-\frac{1}{2}x_{1s}^{\;2}+\tan\alpha_n\left(x_{1s}\right)}}\right] . \tag{2.30}$$

Therefore, using the expressions derived above, one can determine the far-field scattered pressure amplitude as

$$P_s \xrightarrow[r\to\infty]{} \frac{P_0 e^{ik_2 r}}{k_2 r}\left|\sum_{n=0}^{\infty}\left(2n+1\right)\sin\eta_n \exp\left(i\eta_n\right)P_n\left(\cos\theta\right)\right| . \tag{2.31}$$

It is sometimes convenient to express results in the standard form used by Morse and Ingard [21] to describe the far-field pressure scattered by an object of arbitrary shape, i.e.

$$p_s\left(r\right) = \frac{P_0 e^{ik_2 r}}{r}\Phi , \qquad (2.32)$$

where Φ is the far-field scattered angular distribution function or form function. Combining Eqs. (2.31) and (2.32), one can solve for Φ, giving

$$\Phi = \frac{1}{k_2}\left|\sum_{n=0}^{\infty}\left(2n+1\right)\sin\eta_n \exp\left(i\eta_n\right) P_n\left(\cos\theta\right)\right| . \qquad (2.33)$$

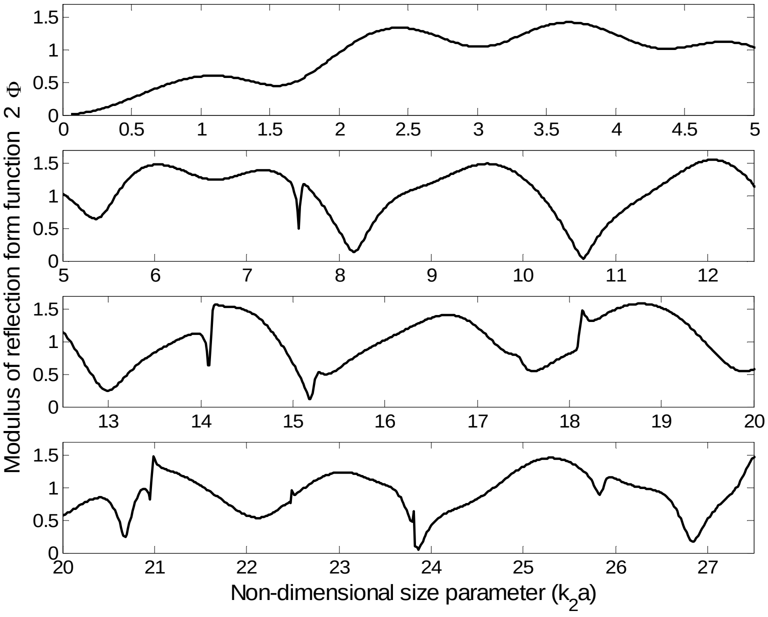

Figure 2.2 Theoretical calculation of the form function (θ = 180^0) vs. k_2a for an aluminum (1100) sphere using the theory from Faran [8] and validated against experimental results and theory given in Neubauer [42] on pg. 166.

The validity of this formulation was verified against previously published experimental measurements and similar theoretical calculations. Neubauer [42, pp 164-171] shows plots of the *modulus of reflection form function* 2Φ versus the *"size parameter"* k_2a, where a is the radius of the sphere. Neubauer's results are plotted for an aluminum (alloy type 1100) sphere at θ = 180^0 and were faithfully replicated in Figure 2.2, using Eq. (2.33) and a shear and longitudinal wave velocity of 3100m/s and 6370 m/s respectively. There is an initial linear region up to $k_2a = 1$, followed by a series of strong shear resonant modes. The initial linear region is also known as the *"Rayleigh regime"*, since it is accurately described by the long-wavelength approximation explored further in Sec. 2.2.3.

2.2.2 The fluid sphere

Since a fluid cannot sustain shear stresses, one can obtain the solution for scattering from a fluid sphere by letting the shear wave speed tend to zero in Eqs. (2.17) - (2.33). A less numerically intensive general solution for the fluid sphere was developed by Anderson [6] in 1950 and is described hereafter.

Similar to the case in Sec. 2.2.1, we consider a plane wave of amplitude P_0 and angular frequency ω traveling through an infinite fluid medium of density ρ_2 in the positive z-direction, and impinging upon a fluid sphere of radius a and density ρ_1. Cast in the general form of Eq. (2.32), Anderson's solution in the far field ($r \gg a$) is given by

$$\Phi = \frac{i}{k_2}\sum_{n=0}^{\infty}\frac{(2n+1)P_n(\cos\theta)}{(1+iC_n)} . \tag{2.34}$$

θ is the scattering angle (180^0 for backscattering), and the coefficient C_n is given by

$$C_n = \frac{\left[\alpha_n'(k_{1c}a)/\alpha_n'(k_2a)\right]\left[n_n(k_2a)/j_n(k_{1c}a)\right]-\left[\beta_n'(k_2a)/\alpha_n'(k_2a)\right]\left[\rho_1c_{1c}/\rho_2c_2\right]}{\left[\alpha_n'(k_{1c}a)/\alpha_n'(k_2a)\right]\left[j_n(k_2a)/j_n(k_{1c}a)\right]-\left[\rho_1c_{1c}/\rho_2c_2\right]} \tag{2.35}$$

with

$$\alpha_n' = nj_{n-1}(kr)-(n+1)\,j_{n+1}(kr) \quad \beta_n' = nn_{n-1}(kr)-(n+1)n_{n+1}(kr) \ , \tag{2.36}$$

where j_n and n_n are the spherical Bessel functions of the first and second (Neumann functions) kind and $P_n(\cos\theta)$ is the Legendre polynomial.

The above expression was validated against the plot of reflectivity factor

$$R_\theta = \frac{2}{a}\Phi \ , \tag{2.37}$$

versus frequency given by Anderson [6] for the backscattering case ($\theta=180^0$) as shown in Figure 2.3.

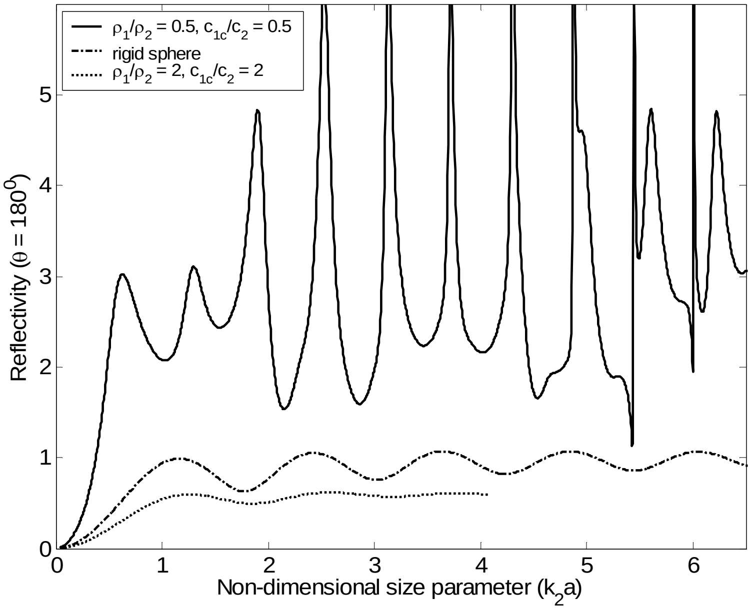

Figure 2.3 Replica of Figure 4 in Anderson's paper [6] depicting the reflectivity (dimensionless) at 180^0 versus the size parameter k_2a for three different cases. The density and sound velocity within the scatterer are given by ρ_1 and c_{1c} while the density and sound velocity outside the scatterer are given by ρ_2 and c_{2c}.

2.2.3 The Rayleigh approximation

The long wavelength approximation, also known as the Rayleigh [1] approximation, assumes that the radius of the sphere scattering the sound is much smaller than the wavelength of the sound in the surrounding medium ($k_2a \ll 1$). This solution is valuable due to the large range of applications to which it may be applied, such as red blood cells being insonified in the region between 5-30 MHz, and due to its simple closed form expression.

Given the exact solution for the scattering from a fluid sphere in Eq. (2.34), truncating all terms except the first two, corresponding to n=0 and n=1, reduces the expression to the following form

$$\Phi = \frac{1}{3} k_2{}^2 a^3 \left[\frac{\kappa_1 - \kappa_2}{\kappa_2} + \frac{3(\rho_1 - \rho_2)}{2(\rho_1 + \rho_2)} \cos\theta \right] , \tag{2.38}$$

where κ_1 and κ_2 correspond to the compressibility of the scatterer and surrounding fluid respectively. Expressions for the compressibility in terms of the densities and speeds of sound inside and outside the scatterer are given by

$$c_{1c} = \frac{1}{\kappa_1 \rho_1} \quad \text{and} \quad c_2 = \frac{1}{\kappa_2 \rho_2} \quad . \tag{2.39}$$

It is important to note that Eq. (2.38) is proportional to the insonifying frequency squared as well as the volume of the scatterer. Roy [43] and Coussios [72] performed a comparison of the exact fluid sphere solution, the solution obtained using the Rayleigh approximation, and the solution obtained using the Born approximation (introduced in the next section). They showed that, for the case of red blood cells suspended in isotonic saline, the scattering cross-section predicted using the Rayleigh approximation exceeds that predicted by the exact fluid sphere solution by no more than 10% up to $k_2 a = 0.35$, beyond which the error becomes significant.

2.2.4 The Born approximation

The Born approximation takes an entirely different approach from the methods introduced earlier in the chapter. In this case, one must consider the spherical scatterer as an inhomogeneous region of volume V in an otherwise homogeneous fluid. Morse and Ingard [21] then give an integral expression for the scattered wave

$$p_s(r) = \iiint_V \left\{ k_2{}^2 \Delta\kappa(\mathbf{r}_0)\, p_t(\mathbf{r}_0)\, g(\mathbf{r}, \mathbf{r}_0) - \Delta\rho(\mathbf{r}_0) \left[\nabla_0 p_t \cdot \nabla_0 g \right] \right\} dv_0 \ , \tag{2.40}$$

where p_t is the total pressure, defined as the sum of the incident and scattered waves and

$$\Delta\kappa = \frac{(\kappa_1 - \kappa_2)}{\kappa_1} \quad \text{and} \quad \Delta\rho = \left(\frac{\rho_1 - \rho_2}{\rho_1} \right) . \tag{2.41}$$

The term $g(\mathbf{r},\mathbf{r}_0)$ is the free space Green function

$$g\left(\mathbf{r},\mathbf{r}_0\right)=\frac{e^{ik_2\left|\mathbf{r}-\mathbf{r}_0\right|}}{4\pi\left|\mathbf{r}-\mathbf{r}_0\right|} \tag{2.42}$$

and V refers to the volume of the inhomogeneous region with density ρ_1 and compressibility κ_1, while the density and compressibility of the fluid are given by ρ_2 and κ_2. The subscript "o" refers to the coordinates within the volume V.

If one assumes that the inhomogeneous scattering region is "weak", such that the incident plane wave remains almost unaltered, and that observation occurs in the farfield ($r \gg a$), then Eq. (2.40) can be reduced to the form in Eq. (2.32) with

$$\Phi=\frac{k_2^{\ 2}}{4\pi}\iiint_V \left\{\Delta\kappa\left(\mathbf{r}_0\right)+\Delta\rho\left(\mathbf{r}_0\right)\cos\theta\right\} e^{\left(iz\mathbf{r}_0\right)} dv_0 \ . \tag{2.43}$$

The underlying assumption of the Born approximation is that the total field, i.e. the sum of the incident and scattered fields, in the scattering region can be approximated by the incident field ($p_t \approx p_i$), since the scattered wave is considered much smaller than the incident one. If one assumes that the inhomogeneous scattering region is a sphere of radius a, and that $\Delta\kappa$ and $\Delta\rho$ are constant, Eq. (2.43) becomes

$$\Phi=\frac{k_2^{\ 2}}{4\pi}\left[\Delta\kappa+\Delta\rho\cos\theta\right]\int_0^a \int_0^\pi \int_0^{2\pi} \sin\theta' r'^2 e^{izr'\cos\theta'} d\phi' d\theta' dr' \ , \tag{2.44}$$

where

$$z=2k_2\sin\left(\theta/2\right) \ . \tag{2.45}$$

After integrating Eq. (2.44) one reaches the final solution for the form function of "weak" scatterers, which takes the following form

$$\Phi=k_2^{\ 2}a^3\left[\frac{\kappa_1-\kappa_2}{\kappa_2}+\frac{\rho_1-\rho_2}{\rho_1}\cos\theta\right]\frac{j_1\left(za\right)}{za} \ , \tag{2.46}$$

where j_1 is the spherical Bessel function of the first kind.

Considering the case in which the $k_2 a \ll 1$, then $j_1(za)/(za) = 1/3$, and the result given in Eq. (2.46) reduces to a form similar to that of the Rayleigh approximation given in Sec. 2.2.3

$$\Phi = \frac{k_2{}^2 a^3}{3}\left[\frac{\kappa_1 - \kappa_2}{\kappa_2} + \frac{\rho_1 - \rho_2}{\rho_1}\cos\theta\right]. \tag{2.47}$$

Figure 2.4 shows a comparison of the backscattering cross sections obtained using each of the four models discussed in Sec. 2.2.1-2.2.4 for the case of a red blood cell in isotonic saline. One can observe that the Born approximation is in much closer agreement with the exact solution than the Rayleigh approximation, and may be used as a good approximation for values up to $k_2 a = 1$ with an error of approximately 6% [43].

2.2.5 Scattering cross-section for red blood cells

After having defined the scattering form function Φ, one can express the differential scattering cross section as [42]

$$\sigma_d = \left|\Phi(\theta)\right|^2 \tag{2.48}$$

and for convenience, the reduced scattering cross-section, which is non-dimensional, as

$$\sigma_r = \frac{\left|\Phi(\theta)\right|^2}{\pi a^2}, \tag{2.49}$$

where a is the radius of the sphere.

The models developed in Sec. 2.2.1- 2.2.4 were mainly used to estimate the scattering cross-section of a spherical red blood cell suspended in isotonic saline. Figure 2.4 shows the non-dimensional differential scattering cross-section evaluated at $\theta = 180^0$ (backscatter). One can observe how the Anderson solution exactly matches the Faran solution evaluated in the limit where the shear velocity tends to zero. In addition, the Rayleigh and Born approximations diverge from the exact solution at about $k_2a \approx 0.35$ but the Born approximation remains in closer agreement with the exact solution as the non-dimensional size parameter k_2a increases.

Red blood cells are known to be shaped as biconcave discs with a diameter that ranges from 7.4 to 9.4 μm [72], but modeling them as spherical scatterers of equivalent volume (mean radius of 2.75 μm) was found to be a very good approximation up to 30 MHz, corresponding to $k_2a \approx 0.35$ [72].

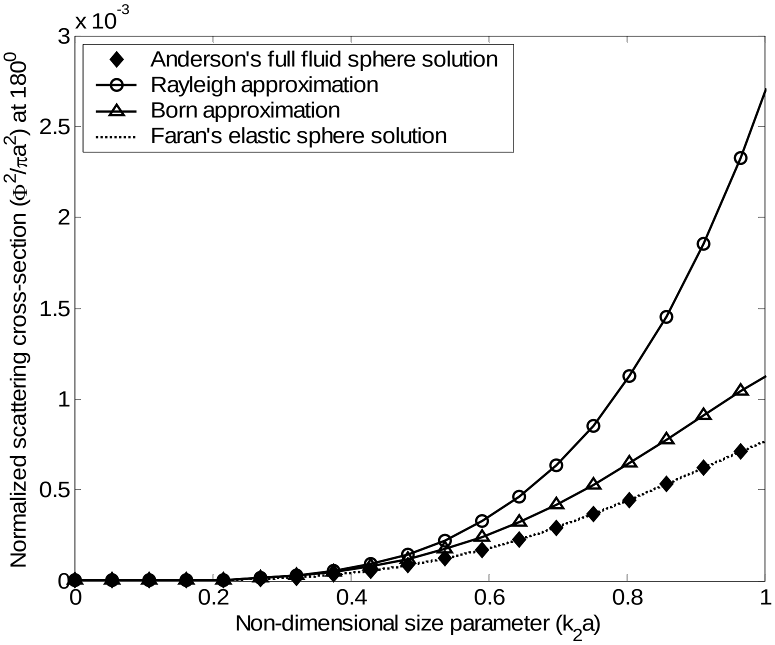

Figure 2.4 Reduced scattering cross-section (dimensionless) for a red blood cell modeled as a fluid sphere in isotonic saline using the Anderson and Faran solutions as well as the Born and Rayleigh approximations for $\theta = 180^0$. Similar plots are given in Roy [43] and Coussios [72].

2.3 Ultrasound Scattering from Cylinders

Our study of the SNR employed a cylindrical elastic scatterer immersed in a suspension of red blood cells. Scattering by cylinders has been investigated by many authors such as Faran [8], Dardy et al. [28], Doolittle an Überall [19], and Scheutz and Neubauer [30]. The formulation used in the derivation below is that obtained from Faran [8] and is very similar to the one depicted in section 2.2.1 for the elastic sphere.

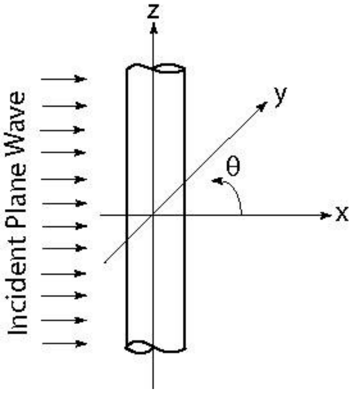

Figure 2.5 Coordinate system used to develop the solution for scattering from an elastic cylinder. Figure replicated from Faran [8].

The coordinate system is given in Figure 2.5, with the plane wave approaching along the negative *x*-axis. The longitudinal and shear wave speeds are the same as those given in Eqs. (2.16) and (2.17). The incident and outgoing pressure fields can be expressed as

$$p_i = P_o \sum_{n=0}^{\infty} \varepsilon_n \left(-i\right)^n J_n\left(k_2 r\right) \cos n\theta \tag{2.50}$$

$$p_s = P_o \sum_{n=0}^{\infty} c_n \left[J_n\left(k_2 r\right) - iN_n\left(k_2 r\right) \right] \cos n\theta \, , \tag{2.51}$$

where J_n and N_n are the cylindrical Bessel functions of the first and second (Neumann function) kind and ε_n is the Neumann factor (ε_0=1; ε_n=2, n>0).

After applying the correct boundary conditions for pressure, displacement, and setting the tangential components of the shearing stress to zero at the surface of the cylinder, the expansion coefficient c_n was found to be of the form

$$c_n = -P_0 \varepsilon_n \left(-i\right)^{n+1} \sin\eta_n \exp\left(i\eta_n\right) \ , \tag{2.52}$$

where η_n is the phase shift of the n^{th} scattered wave and is given by the expression

$$\tan\eta_n = \tan\delta_n\left(x_2\right)\frac{\left[\tan\Phi_n + \tan\alpha_n\left(x_2\right)\right]}{\tan\Phi_n + \tan\beta_n\left(x_2\right)} , \tag{2.53}$$

which is the same as that of the sphere given in Eq. (2.26) and where

$$\begin{aligned} x_{1c} &= k_{1c}a \\ x_{1s} &= k_{1s}a \\ x_2 &= k_2 a \ , \end{aligned} \tag{2.54}$$

and

$$\begin{aligned} \delta_n\left(x\right) &= \tan^{-1}\left[\frac{-J_n\left(x\right)}{N_n\left(x\right)}\right] \\ \alpha_n\left(x\right) &= \tan^{-1}\left[\frac{-xJ_n^{'}\left(x\right)}{J_n\left(x\right)}\right] \\ \beta_n\left(x\right) &= \tan^{-1}\left[\frac{-xN_n^{'}\left(x\right)}{N_n\left(x\right)}\right] \ . \end{aligned} \tag{2.55}$$

The quantities, k_{1c}, k_{1s}, and k_2 denote the compressional wavenumber in the scatterer, the shear wavenumber in the scatterer, and the compressional wavenumber in the fluid outside the scatterer. In addition, the impedance phase-angle Φ_n must be determined to complete the derivation of the phase shift η_n. This impedance phase-angle Φ_n is dependent on the material properties of the cylinder and is the same as that of the sphere given in Eq. (2.29), with

$$\zeta_n\left(x_{1c},\nu\right)=\tan^{-1}\left[-\frac{{x_{1s}}^2}{2}\frac{\dfrac{\tan\alpha_n\left(x_{1c}\right)}{\tan a_n\left(x_{1c}\right)+1}-\dfrac{n^2}{\tan\alpha_n\left(x_{1s}\right)+n^2-\frac{1}{2}{x_{1s}}^2}}{\dfrac{\tan\alpha_n\left(x_{1c}\right)+n^2-\frac{1}{2}{x_{1s}}^2}{\tan\alpha_n\left(x_{1c}\right)+1}-\dfrac{n^2\left[\tan\alpha_n\left(x_{1s}\right)+1\right]}{\tan\alpha_n\left(x_{1s}\right)+n^2-\frac{1}{2}{x_{1s}}^2}}\right]. \qquad (2.56)$$

Therefore, using the expressions derived above, one can determine the farfield scattered pressure amplitude

$$P_s\xrightarrow[r\to\infty]{}P_0e^{ik_2r}\left(\frac{2}{\pi k_2 r}\right)^{\frac{1}{2}}\left|\sum_{n=0}^{\infty}\varepsilon_n\sin\eta_n\exp\left(i\eta_n\right)\cos n\theta\right|. \qquad (2.57)$$

Rewriting Eq. (2.57) in the standard form of Eq. (2.32) [42], the farfield scattered angular distribution function for the cylinder becomes

$$\Phi=\left(\frac{2r}{a}\right)^{\frac{1}{2}}\frac{p_s}{P_0}\ . \qquad (2.58)$$

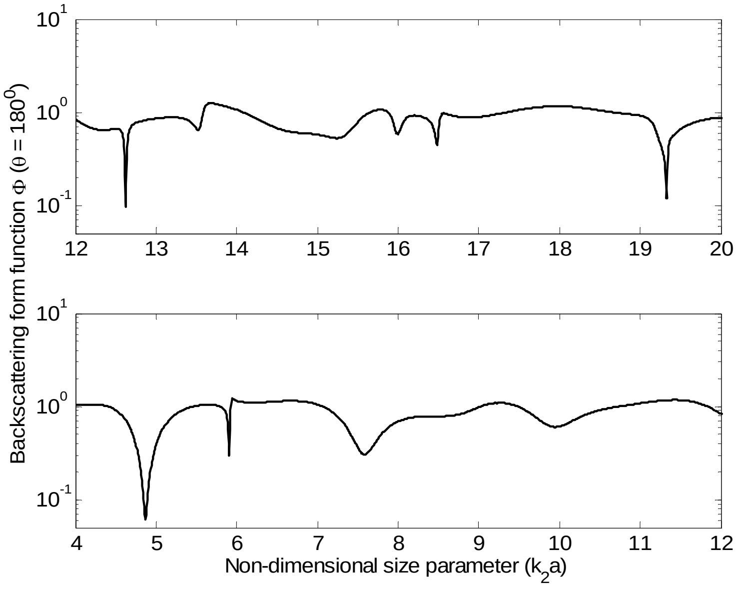

Figure 2.6 Theoretical calculation of the dimensionless form function ($\theta = 180^0$) vs. k_2a for an aluminum cylinder using the theory from Faran in [8] and validated against experimental results given in Neubauer [42] on p. 72.

In order to validate the theory for scattering from a rigid cylinder, a theoretical calculation validated against experimental results by Neubauer [42] was faithfully replicated, as shown in Figure 2.6. This plot displays the form function given in Eq. (2.58) evaluated at $\theta=180^0$ for an aluminum cylinder in water. It is important to note how well the theory developed by Faran (and rederived in the present section) displays the elastic modes within the cylinder, which perfectly matches the experimental results given in Neubauer [42] (not shown on plot).

2.4 Ultrasound Scattering from Contrast Agents

As explained previously, ultrasound contrast agents are gas-filled microbubbles surrounded by a shell often constructed of human serum albumin, preventing the bubble from breaking up or dissolving when injected in the human circulatory system. Attempts to model their response to acoustic excitation can be divided into two different categories: those based on expressing the incident plane wave in spherical harmonics and matching boundary conditions on the surface of elastic spherical shells, such as Ye [64] and Allen [71]; and those based on solving variants of the Rayleigh-Plesset equation [61] describing bubble dynamics, with the inclusion of an additional damping term to account for the properties of the shell, such as de Jong et al. [57], de Jong and Hoff [58], and Church [62]. The following sections will investigate and compare both approaches. It is important to mention that the theoretical formulations explaining the scattering from contrast agents will be derived for a single bubble only. Expressions for the modeling of collections of scatterers, both monodisperse and polydisperse, will be investigated in Chapter 3.

Both the spherical shell model and the bubble dynamics model were found to be in good agreement. This is especially true near resonance, but less so away from resonance, when the scattered wave is no longer isotropic and directionality becomes important. The bubble, when subjected to an acoustic field, is driven into oscillations, and these oscillations are modeled with differential equations of motion which will be introduced in Sec. 2.4.2. Assuming that the bubble is acoustically compact ($a \ll \lambda$), the scattered pressure can be set equal to the pressure radiated by the bubble. This assumption was found to be valid near resonance but starts to break down as the frequency is increased. As ka tends to infinity, the bubble dynamics model predicts that the bubble no longer oscillates and that the radiated pressure therefore tends to zero. On the other had, it is well known from the elastic shell model and the fluid sphere approximation that a bubble beyond resonance behaves as a rigid scatterer, and that the scattered pressure is therefore different from zero.

Bubble dynamics models also assume that the pressure is radiated isotropically, and therefore ignore higher-order resonances that can be predicted by the elastic shell model. As can be seen from Figure 2.9 and Figure 2.10, these higher order vibrations are extremely narrowband, making them almost impossible to detect in a laboratory environment. The fact that the population of scatterers ultimately investigated is not perfectly monodisperse implies that these higher resonances have little practical significance.

An introduction and comparison of both the elastic shell scattering model and the radiating bubble dynamics model will follow in sections 2.4.1 and 2.4.2, demonstrating that the two models are in good agreement over the frequency range considered in the present investigation.

2.4.1 The elastic shell

Important publications for the scattering from elastic spheres are those by Hickling [15, 17], Goodman and Stern [13], Gaunaurd [29] and Hasegawa et al. [59]. The present formulation follows that performed by Zhen Ye [64] who applied the theory developed by Hasegawa et al. [59] to the specific case of an Albunex® bubble.

Figure 2.7 shows the spherical coordinate system used in the formulation for sound scattering from an elastic shell of inner radius *a* and outer radius *b*, surrounded by a non-viscous fluid and excited by an incident plane wave. Following the formulation by Zhen Ye [64] and Hasegawa [59] the incident velocity potential can be written as

$$\Xi_i = \Xi_0 \sum_{n=0}^{\infty} (2n+1)(-i)^n \, j_n(k_2 r) P_n(\cos\theta) e^{i\omega t} \ , \tag{2.59}$$

where Ξ_0 is the amplitude of the incident wave, j_n is the spherical Bessel function of the first kind, P_n is the Legendre polynomial, and k_2 is the wavenumber corresponding to ω/c_2.

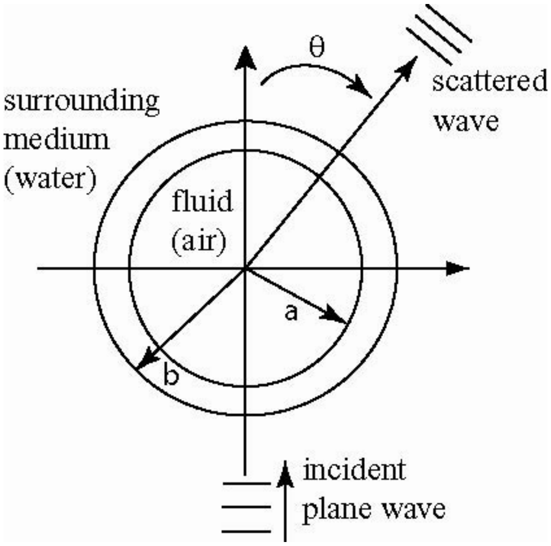

Figure 2.7 Spherical coordinate system used to calculate the acoustic scattering from a spherical shell. Figure obtained from Zhen Ye [64].

The subscript 1 refers to the shell material, 1_g to the gas inside the shell and 2 to the surrounding medium. The pressure is related to the velocity potential by

$$p = \rho \frac{\partial \Xi}{\partial t} \ , \tag{2.60}$$

where ρ is the density. Similarly, the velocity potential for the scattered wave can be written as

$$\Xi_s = \Xi_0 \sum_{n=0}^{\infty} (2n+1)(-i)^n \, a_n h_n^{(2)}(k_2 r) P_n(\cos\theta) e^{i\omega t} \ , \tag{2.61}$$

where $h_n^{(2)}$ is the Hankel function of the second kind and a_n is an unknown coefficient that will be determined by the boundary conditions given in Eq. (2.62). Potentials of the shell and gas are also given but will be excluded from this discussion since our main interest is to determine the scattered wave. For more details one may refer to Zhen Ye [64] and Hasegawa et al. [59].

In order to determine the unknown coefficient a_n one must apply three boundary conditions: the pressure in the gas and in the surrounding medium must equal the normal component of the stress in the shell, there must be continuity of displacement at the interfaces, and assuming the viscosity of the gas and that of the medium are negligible, the tangential component of the shear stress must vanish at the interfaces. Given these boundary conditions a_n becomes

$$a_n = -\frac{F_n j_n\left(k_2 a\right) - k_2 a j_n'\left(k_2 a\right)}{F_n h_n^{(2)}\left(k_2 a\right) - k_2 a h_n^{(2)}\left(k_2 a\right)} \tag{2.62}$$

and F_n is given by

$$F_n = -\rho_2 \frac{\begin{vmatrix} \alpha_{22} & \alpha_{23} & \alpha_{24} & \alpha_{25} & 0 \\ \alpha_{32} & \alpha_{33} & \alpha_{34} & \alpha_{35} & 0 \\ \alpha_{42} & \alpha_{43} & \alpha_{44} & \alpha_{45} & \alpha_{46} \\ \alpha_{52} & \alpha_{53} & \alpha_{54} & \alpha_{55} & \alpha_{56} \\ \alpha_{62} & \alpha_{63} & \alpha_{64} & \alpha_{65} & 0 \end{vmatrix}}{\begin{vmatrix} \alpha_{12} & \alpha_{13} & \alpha_{14} & \alpha_{15} & 0 \\ \alpha_{32} & \alpha_{33} & \alpha_{34} & \alpha_{35} & 0 \\ \alpha_{42} & \alpha_{43} & \alpha_{44} & \alpha_{45} & \alpha_{46} \\ \alpha_{52} & \alpha_{53} & \alpha_{54} & \alpha_{55} & \alpha_{56} \\ \alpha_{62} & \alpha_{63} & \alpha_{64} & \alpha_{65} & 0 \end{vmatrix}}, \tag{2.63}$$

where | | stands for the determinant and the coefficients of Eq. (2.63) are given in Appendix B of Hasegawa et al., in the Appendix of Zhen Ye [64], and are displayed in Appendix A.

Combining Eqs. (2.62) and (2.61) one can obtain an expression for the scattered field in standard form as the farfield scattered angular distribution function or form function given by

$$\Phi = \frac{1}{k_2} \sum_{n=0}^{\infty} (2n+1)(-i)^n a_n P_n(\cos\theta) e^{i(n+1)\pi/2} , \tag{2.64}$$

where Φ is defined as

$$\lim_{r\to\infty} \frac{\Xi_s}{\Xi_i} = \Phi \frac{e^{ik_2 r}}{r} \tag{2.65}$$

and the Hankel function of the second kind is approximated by

$$h_n^{(2)}(x) = \frac{1}{x} e^{ix+i(n+1)\pi/2}, \quad x \gg 1 . \tag{2.66}$$

As in Sec. 2.2.5 the differential scattering cross-section and the reduced scattering cross-section (non-dimensional) can be expressed by Eqs. (2.48) and (2.49).

To check that the above equations are valid, the result given in Eq. (2.64) was approximated for the fluid sphere, where the inner radius *a* tends to the outer radius *b* and compared to the classical paper by Anderson [6].[1] The results given in Figure 2.8 exactly match those by Anderson and those of Figure 2.3, where the sound reflectivity is defined in Eq. (2.37).

Given the results above, one can compute the scattering cross-section for a typical contrast agent with different shell parameters. Figure 2.9 shows a reproduction of Zhen Ye's result given in Figure 13b [64] for an 8 µm radius contrast agent with shell parameters ρ_1 = 1100 kg/m^3, G_s = 88 MPa, and λ_s = 6.1x10^4 MPa, where ρ_1, G_s, λ_s are the density, shear Lamé constant, and elastic Lamé constant. These shear and elastic Lamé constants are related to the shear and elastic sound speeds with the relations given in Eqs. (2.16) and (2.17) where $G_s=\mu$. In addition, one may obtain good insight on the effect of the shell stiffness from Figure 2.10, where one can clearly see how the main resonance peak of the bubble shifts to the right as the stiffness increases.

---

[1] This check was also performed by Zhen Ye in [64] to double check the theoretical implementation by Hasegawa et al. [59].

This same figure is obtained by Zhen Ye [64], Figure 10a. Notice the higher order resonances that appear as the frequency increases. These resonances will not be predicted by the model that uses bubble dynamics discussed in the next section.

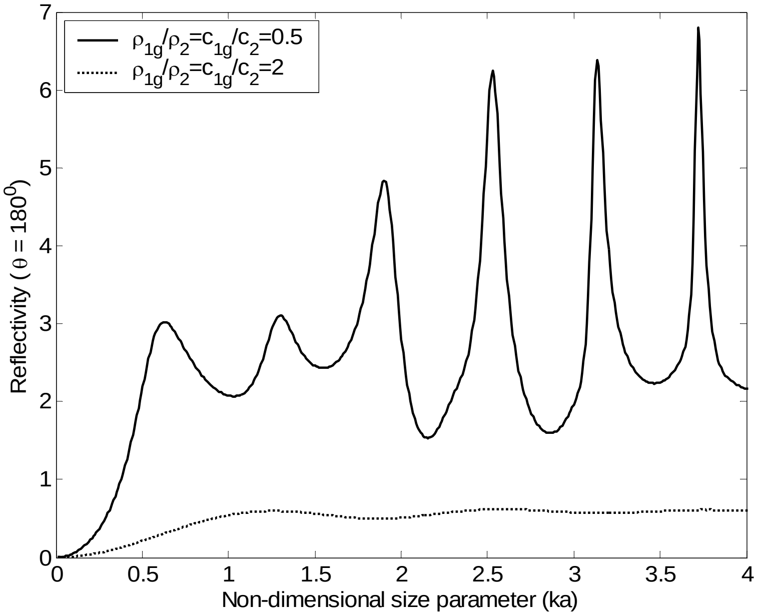

Figure 2.8 Figure used to validate the solution obtained by Zhen Ye [64] and Hasegawa et al. [59], depicting the reflectivity (dimensionless) as a function of the acoustic parameter *ka* for different density and velocity contrasts for a fluid sphere. Same as Anderson's result given in Figure 2.3.

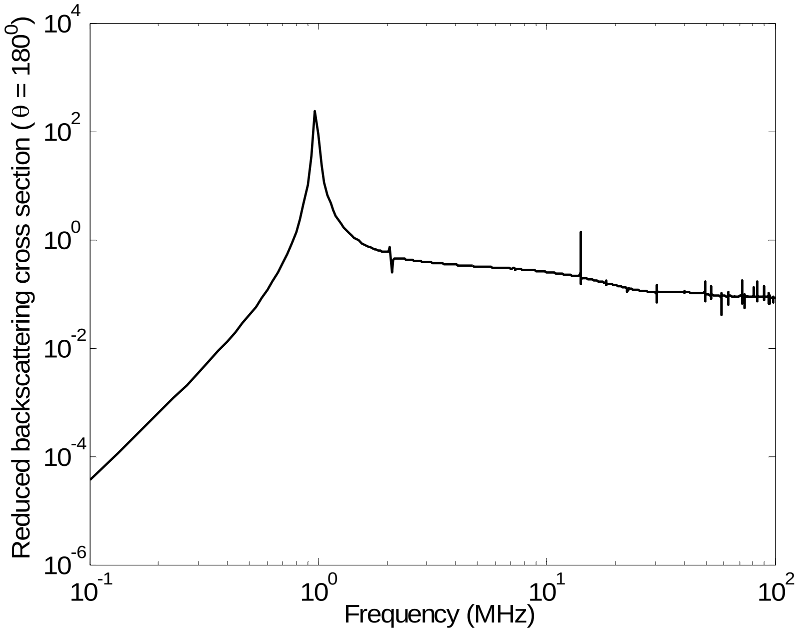

Figure 2.9 Reduced backscattering ($\theta = 180^0$) cross-section (dimensionless) for an 8 μm radius contrast agent with a shell thickness of 15 nm. The shell parameters are G_s=88 MPa, λ_s=6.1x10^4 MPa and ρ_2=1100 kg/m^3.

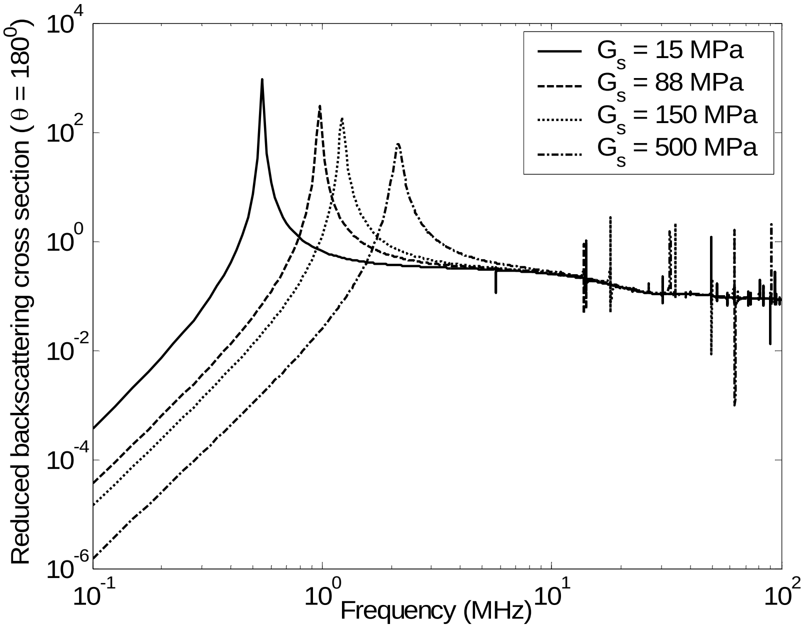

Figure 2.10 Reduced backscattering ($\theta = 180^0$) cross-section (dimensionless) for an 8μm radius contrast agent with a shell thickness of 15 nm and different shell stiffness parameters.

2.4.2 Bubble dynamics and the “Church” model

In the previous section, a contrast agent was modeled as a spherical elastic shell containing a gas inside and embedded in a host fluid. Alternatively, one may consider a contrast agent as a bubble with a surrounding surface layer. Therefore, the behavior of a contrast agent when exposed to an acoustic pressure can be modeled as that of a free bubble with the addition of terms that take into account the presence of the surface layer. Analytical formulations for such a problem have been investigated by de Jong [57], de Jong and Hoff [58], Hoff [73], and Church [62]. These models describe the dynamics of the contrast agent through the use of linear and non-linear bubble dynamics, usually treating the effect of the surface layer as an additional term in the Rayleigh-Plesset equation (see Leighton [61] and Hoff [73]). The basic equations describing bubble dynamics are developed hereafter, starting by treating the bubble as a simple harmonic oscillator and ending with the model developed by Church [62], which accounts for the viscoelasticity of the shell.

The free bubble

Considering a bubble as a simple harmonic oscillator, the differential equation of motion for the displacement in the radial direction ξ is (Chapter 3 in Leighton [61] and Chapter 2 in Hoff [73])

$$m\ddot{\xi} + R\dot{\xi} + s\xi = -4\pi a^2 p_a \ , \tag{2.67}$$

where *m* is the effective mass of an oscillating bubble defined as

$$m = 4\pi a^3 \rho \tag{2.68}$$

and *s* is the spring constant derived by Hooke’s law as

$$s = 12\pi a \kappa p_e \ . \tag{2.69}$$

The constants a, ρ, κ, p_a, and p_e refer to the equilibrium radius of the bubble, density of the liquid outside the bubble, the polytropic exponent, the driving acoustic pressure, and the equilibrium pressure inside the bubble respectively. This equilibrium pressure is equal to the hydrostatic pressure p_0 with the addition of the effect due to surface tension σ

$$p_e = p_0 + \frac{2\sigma}{a} \ . \tag{2.70}$$

Finally, the term denoted by R in Eq. (2.67) is the mechanical resistance of the oscillating bubble, usually modeled as the sum of the radiation (R_c), viscous ($R_{\eta L}$), and thermal resistances (R_{th})

$$R = R_c + R_{\eta L} + R_{th} \ . \tag{2.71}$$

The resistances were specifically found to be

$$R_c = 4\pi a^2 \rho c \left(ka\right)^2 , \tag{2.72}$$

where ρc is the specific acoustic impedance and k is the wavenumber,

$$R_{\eta L} = 16\pi a \eta_L , \tag{2.73}$$

where η_L is the viscosity of the liquid, and

$$R_{th} = \frac{12\pi a p_e}{\omega} \operatorname{Im}\left(\frac{1}{\chi\left(a,\omega\right)} \right) , \tag{2.74}$$

where ω is the angular frequency. The term $\chi(a, \omega)$ was derived by Devin [11] and given by the expression

$$\chi\left(a,\omega\right) = \frac{1}{\gamma}\left(1 + \frac{3\left(\gamma - 1\right)}{\psi^2}\left(\psi \coth\psi - 1\right) \right) , \tag{2.75}$$

with γ being the adiabatic constant and

$$\psi\left(a, l_D\left(\omega\right)\right) = \frac{1}{2}\left(1+i\right)\frac{a}{l_D} , \tag{2.76}$$

where l_D is the thermal diffusion length. The thermal diffusion length relates the density of the gas ρ_g, the heat capacity C_p, and the thermal conductivity K_g

$$l_D(\omega) = \sqrt{\frac{K_g}{2\omega\rho_g C_p}} \quad . \tag{2.77}$$

Given the above results, we can now take the Fourier transform of Eq. (2.67) and obtain

$$\left(-\omega^2 + i\omega\omega_0\delta + \omega_0{}^2\right)\hat{\xi}(\omega) = \frac{1}{\rho a}\hat{p}_a(\omega) \ , \tag{2.78}$$

where ω_0 and δ are the angular resonance frequency and the damping constant defined as

$$\begin{aligned} \omega_0{}^2 &= \frac{s}{m} = \frac{3\kappa p_e}{a^2\rho} \\ \delta &= \frac{R}{\omega_0 m} \quad . \end{aligned} \tag{2.79}$$

From Eq. (2.79), one may therefore determine the linear resonance frequency f_0

$$f_0 = \frac{\omega_o}{2\pi} = \frac{1}{2\pi a}\sqrt{\frac{3\kappa p_e}{\rho}} \tag{2.80}$$

also known as the Minnaert-frequency, which was first derived in [3].

From the Eqs. (2.72) - (2.74) for the mechanical resistance R one can determine expressions for the damping constant, defined as $\delta = \delta_c + \delta_{\eta L} + \delta_{th}$

$$\begin{aligned} \delta_c &= \frac{\omega^2 a}{\omega_0 c} \\ \delta_{\eta L} &= \frac{4\eta_L}{\omega_0 \rho a^2} \\ \delta_{th} &= \frac{3p_e}{\omega\omega_0\rho a^2}\operatorname{Im}\left(\frac{1}{\chi}\right) \quad . \end{aligned} \tag{2.81}$$

Given all of the results above, the radial displacement can be determined from the equation of motion (2.78) as

$$\hat{\xi}(\omega)=\frac{1}{\rho a\omega_0{}^2}\frac{\hat{p}_a(\omega)}{(\omega/\omega_0)^2-1-i\,\omega/\omega_0\delta}\ . \tag{2.82}$$

In order to determine the scattering cross-section of a bubble, one must first determine the scattered pressure at the surface of the bubble. This pressure ($\hat{p}_s$) is set equal to the pressure radiated by the bubble. Considering the scattered wave as a diverging spherical wave and applying the Euler equation (pg. 15 in Hoff [73]), one can determine the radiated sound pressure

$$\hat{p}_s(a,\omega)=a\rho\ddot{\xi}\frac{1}{1+ika}\approx-\omega^2a\rho\hat{\xi}(\omega)\ . \tag{2.83}$$

Inserting the result given in Eq. (2.82) into Eq. (2.83), one obtains the final expression for the radiated pressure at the bubble surface as

$$\Omega=\omega/\omega_0 \tag{2.84}$$

$$\hat{p}_s(a,\omega)=\frac{\Omega^2}{1-\Omega^2+i\Omega\delta}\,\hat{p}_a(\omega)\ . \tag{2.85}$$

Finally, one can determine the scattering cross-section $\sigma_s(a,\omega)$ for a bubble, defined as the scattered power, $\Pi_s(a,\ \omega)$, over the incident sound intensity, $I_i(\omega)$, i.e.

$$\sigma_s(a,\omega)=\frac{\Pi_s(a,\omega)}{I_i(\omega)}\ , \tag{2.86}$$

which in terms of pressure reduces to

$$\sigma_s(a,\omega)=4\pi a^2\left|\frac{\hat{p}_s(a,\omega)}{\hat{p}_a(\omega)}\right|^2=4\pi a^2\frac{\Omega^4}{\left(1-\Omega^2\right)^2+\left(\Omega\delta\right)^2}\ . \tag{2.87}$$

The shelled bubble

As explained previously, contrast agents can be considered as free bubbles surrounded by a shell or surface layer. This shell alters the dynamics of the bubble by reducing its compressibility, increasing its resonance frequency, and increasing the viscous damping due to the shell viscosity. A good explanation of these effects is given in Hoff [73] pg. 36-41 with results outlined below. The expression for the spring constant of the bubble or stiffness of the bubble given in Eq. (2.69) is expanded to include the stiffness of the shell

$$s = 12\pi a\kappa p_e + 48\pi G_s ds_e \quad . \tag{2.88}$$

where G_s is the stiffness of the shell and ds_e is the thickness of the shell. On the other hand, if one assumes that the shell is thin compared to the radius of the bubble ($ds_e \ll a$), the dynamic mass of the shelled bubble remains the same as that of the free bubble given in Eq. (2.68). Finally, the mechanical resistance R given in Eq. (2.71) is altered with the addition of a term due to the viscosity in the shell

$$R = R_c + R_{\eta L} + R_{th} + R_{\eta s} \quad , \tag{2.89}$$

where R_c, $R_{\eta L}$, and R_{th} are the same as those given in Eqs. (2.72)-(2.74), while $R_{\eta s}$ is the resistance due to shell viscosity η_s, given by

$$R_{\eta s} = 48\pi\eta_s ds_e \quad . \tag{2.90}$$

Therefore, the dimensionless damping constant becomes $\delta = \delta_c + \delta_{\eta L} + \delta_{th} + \delta_{\eta s}$, where $\delta_{\eta s}$ takes the form

$$\delta_{\eta s} = \frac{12\eta_s ds_e}{\omega_0 \rho a^3} \quad . \tag{2.91}$$

The modified resonance frequency with the addition of the effects due to the shell is therefore given as

$$f_o = \frac{1}{2\pi a}\sqrt{\frac{3\kappa p_e + 12 G_s \, ds_e / a}{\rho}} \quad . \tag{2.92}$$

Given the results above, the modified scattering cross-section for the shelled bubble can be computed using the same expression as that given in Eq. (2.87) with the use of the modified damping constant $\delta = \delta_c + \delta_{\eta L} + \delta_{th} + \delta_{\eta s}$.

The "Church" model

The theoretical formulations described previously allowed us to have a good insight on the dynamics of a bubble by modeling it as a linear oscillator. Nevertheless, the response of real bubbles was most often found to be nonlinear in nature. Nonlinearities arise due to a variety of effects, such as non-symmetrical expansion and compression, a decrease in bubble radius as the bubble dissolves, an increase in bubble radius due to rectified diffusion (diffusion of gas into the bubble promoted by the sound field), to name but a few. Good descriptions of such effects are explained given in Leighton [61], Chapter 4. In order to account for such non-linear effects when modeling a contrast agent, Church [62] derived a non-linear equation of motion considering a bubble surrounded by a surface layer immersed in a liquid. Church's derivation follows the same procedure as those previously performed for a free bubble by Rayleigh [2], Plesset [5], Noltingk and Neppiras [7], and Neppiras and Noltingk [9], who derived the well-known Rayleigh-Plesset equation for bubble dynamics.

The Rayleigh-Plesset equation is the simplest of all non-linear bubble dynamics models. It assumes an incompressible liquid, low Mach number for the bubble surface, and neglects energy loss by radiation. In general, the Rayleigh-Plesset equation of motion for a free bubble takes the form

$$\ddot{a}a + \frac{3}{2}\dot{a}^2 + \frac{p_0 + p_a(t) - p_L}{\rho} = 0 \ , \tag{2.93}$$

where a is the radius of the bubble, p_0 is the static background pressure, $p_a(t)$ is the driving sound field, and p_L is the pressure of the liquid at the bubble surface. With the use of Eq. (2.93), the Bernoulli equation, the continuity equation, and applying the boundary conditions at the bubble surface, one may derive the far-field radiated pressure, which we call the scattered pressure, as

$$p_s(t)\Big|_{far-field} = \rho\frac{a^2\ddot{a} + 2a\dot{a}^2}{r} \ . \tag{2.94}$$

A Rayleigh-Plesset-like model for a shelled bubble has been derived by Church [62]. This model considers the case of a bubble surrounded by a surface active material in a liquid. Figure 2.11 below shows the idealized model of such a bubble where the liquid is depicted by the letter *L*, the gas by *G*, and the layer of surface material by *S*. The inner radius is denoted by the letter *a* and the outer radius by the letter *b*.

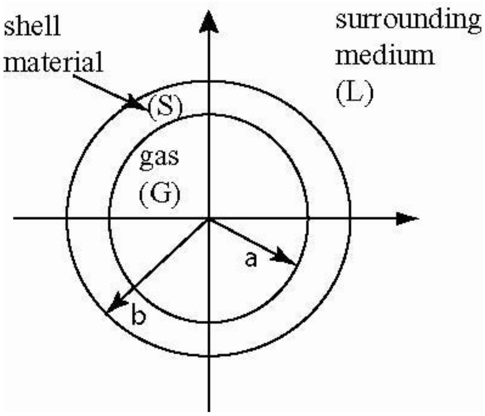

Figure 2.11 Idealized model of a gas bubble surrounded by a surface layer (S) in a liquid (L) used by Church [62] in his model for the dynamics of a contrast agent.

Church begins with expressions for the conservation of mass and radial momentum in a spherically symmetric, incompressible material. The boundary conditions are applied at the two interfaces (gas-shell and shell-liquid). It is further assumed that the gas pressure inside the bubble follows the polytropic relationship, that the liquid *L* is Newtonian and incompressible, and that the shell material is incompressible. The following generalized Rayleigh-Plesset-like equation of motion is obtained for a bubble with a shell of thickness (*b*-*a*)

$$\begin{aligned} &a\ddot{a}\left[1+\left(\frac{\rho_L-\rho_s}{\rho_s}\right)\frac{a}{b}\right]+\dot{a}^2\left[\frac{3}{2}+\left(\frac{\rho_L-\rho_s}{\rho_s}\right)\times\left(\frac{4b^3-a^3}{2b^3}\right)\frac{a}{b}\right] \\ &=\frac{1}{\rho_s}\left[p_G\left(\frac{a_0}{a}\right)^{3\kappa}-p_\infty\left(t\right)-\frac{2\sigma_1}{a}-\frac{2\sigma_2}{b}-4\frac{\dot{a}}{a}\left(\frac{V_s\eta_s+a^3\eta_L}{b^3}\right)-4\frac{V_sG_s}{b^3}\left(1-\frac{a_0}{a}\right)\right], \end{aligned} \tag{2.95}$$

where a_0 is the initial inner radius, p_G is the gas pressure at equilibrium, G_s is the stiffness of the shell, η_s is the viscosity of the shell, η_L is the viscosity of the liquid, σ_1 is the surface tension between the gas and the shell, σ_2 is the surface tension between the liquid and the shell, and $V_s = b_0^3 - a_0^3$.

Given the complexity of Eq. (2.95), analytical solutions can only be found for limiting cases. Church assumed a small pulsation amplitude $a_0x(t)$. Retaining first and second order terms only, Eq. (2.95) reduces to

$$\begin{aligned}&\ddot{x}\left[1+\left(1+\alpha_m\right)x\right]+\frac{3}{2}\left(1+\frac{\alpha_m}{3}\right)\dot{x}^2+\left(\delta_d-\delta_{dn}x\right)\dot{x}+{\omega_0}^2x-{\omega_0}^2x^2\\&=p_A\left(\rho_s{a_0}^2\alpha\right)^{-1}\sin\left(\omega t\right)\ ,\end{aligned} \tag{2.96}$$

where p_A is the acoustic pressure amplitude obtained from $p_\infty(t) = p_0 - p_A\sin(\omega t)$. The linear coefficients in Eq. (2.96) are given as

$$\alpha=\left[1+\left(\frac{\rho_L-\rho_s}{\rho_s}\right)\frac{a}{b}\right] \tag{2.97}$$

$$\delta_d=4\left[\frac{V_s\eta_s+a^3\eta_L}{a^3}\right]\left(\rho_s a^2\alpha\right)^{-1} \tag{2.98}$$

$${\omega_0}^2=\left(\rho_s a^2\alpha\right)^{-1}\left\{3\kappa p_0-\frac{2\sigma_1}{a}-\frac{2\sigma_2 a^3}{b^4}+4\frac{V_sG_s}{b^3}\left[1+Z\left(1+\frac{3a^3}{b^3}\right)\right]\right\}\ , \tag{2.99}$$

where

$$Z=\left[\frac{2\sigma_1}{a}+\frac{2\sigma_2}{b}\right]\left[\frac{b^3}{\mathrm{V_s}}\right]\left(4G_s\right)^{-1} \tag{2.100}$$

and the non-linear coefficients are given as

$$\alpha_m=\left(\frac{\rho_L-\rho_s}{\rho_s}\right)\frac{V_s a}{\alpha b^4} \tag{2.101}$$

$$\delta_{dm}=\delta_d\left(1+\frac{3a^3}{b^3}\right)-\frac{12a\eta_L}{\rho_s b^3\alpha} \tag{2.102}$$

$$\omega_{0n}^{\;2} = \left(\rho_s a^2 \alpha\right)^{-1} \left\{ \begin{aligned} & \frac{3\kappa\left(3\kappa+1\right)}{2} p_0 - \frac{2\sigma_1}{a} \\ & - \frac{2\sigma_2 a^3 \left(a^3 - V_s\right)}{b^7} + 4\frac{V_s G_s}{b^3}\left[\left(1+\frac{3a^3}{b^3}\right) + Z\left(1+\frac{9a^6}{b^6}\right)\right] \end{aligned} \right\} \quad . \qquad (2.103)$$

Finally, Church derived solutions for the scattering cross section at the fundamental frequency and the second harmonic given by the following expressions

$$\sigma_{s1} = \frac{4\pi a^2 \Omega^4}{\left[\left(1-\Omega^2\right)^2 + \delta^2 \Omega^2\right]} \frac{\rho_L^{\;2}}{\alpha \rho_s^{\;2}} \qquad (2.104)$$

$$\sigma_{s2} = \frac{\left\{\left[1+\left(\frac{5}{2}+\frac{3\alpha_n}{2}\right)\Omega_n^{\;2}\right]^2 + \delta_n^{\;2}\Omega_n^{\;2}\right\}}{\left[\left(1-\Omega^2\right)^2+\delta^2\Omega^2\right]^2\left[\left(1-4\Omega^2\right)^2+4\delta^2\Omega^2\right]} \frac{4\pi a^2 \Omega^8 p_A \rho_L^{\;2}}{\left(\alpha\rho_s a \omega_0 \Omega_n\right)^4} \quad , \qquad (2.105)$$

where

$$\Omega = \frac{\omega}{\omega_0}, \qquad \Omega_n = \frac{\omega}{\omega_{0n}}, \qquad \delta = \frac{\delta_d}{\omega_0}, \qquad \delta_n = \frac{\delta_{dn}}{\omega_{0n}} \quad . \qquad (2.106)$$

An example of the fundamental reduced scattering cross-section ($\sigma_{s1}/\pi a^2$) as a function of bubble radius for different frequencies is given in Figure 2.12. This figure replicates Figure 6 in the paper by Church [62] and was computed using the following parameters: p_0=0.1 MPa, ρ_L=1.0 g/cm^3, η_L=0.01 P, σ_1=40 dyne/cm, c=1500 m/s, ρ_s=1.1 g/cm^3, η_s=17.7 P, σ_2=5 dyne/cm, G_s=88.8 MPa, and b-a=15 nm. One can clearly see how the first harmonic resonance peak shifts to the right as the frequency decreases, as expected from free bubble theory. Also, from Figure 2.13 and Figure 2.14 one can observe the effect of the shell stiffness. As the shell stiffness (G_s), increases, both the resonance frequency and the resonance radius increase. The relationship between resonance frequency and radius is given in Figure 2.15 for different values of the shell stiffness G_s. Figure 2.14 exactly mimics the result obtained in Figure 2.10 with the elastic shell theory, but fails to predict the higher order resonance modes.

Finally, the two models developed for the scattering of contrast agents (elastic shell and bubble dynamics) are compared in Figure 2.16. The resonance frequency obtained by both models is the same even though the amplitude and sharpness of the peak differ. In addition, the elastic shell model displays higher order resonances that the bubble dynamics model fails to predict.

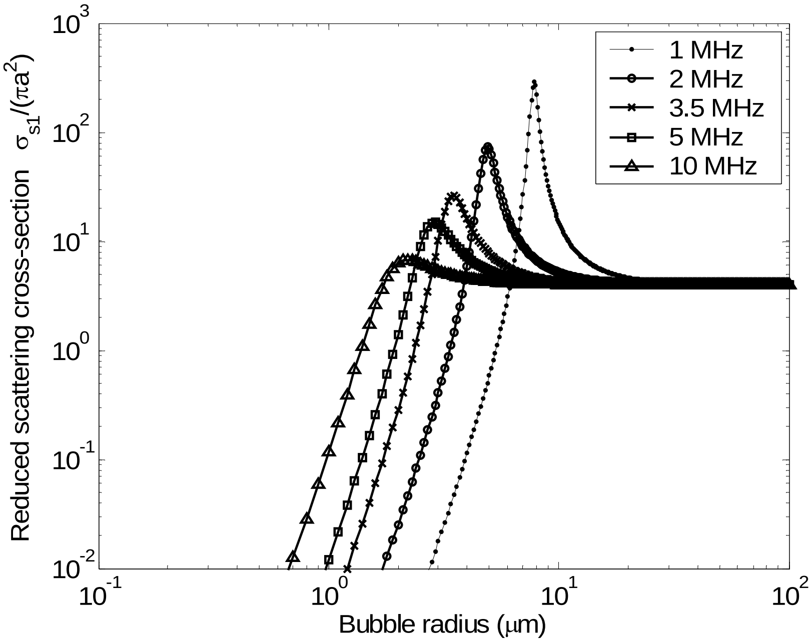

Figure 2.12 Replica of Figure 6 from Church [62] displaying the fundamental reduced scattering cross-section (dimensionless) for a shelled bubble as a function of radius for different driving frequencies.

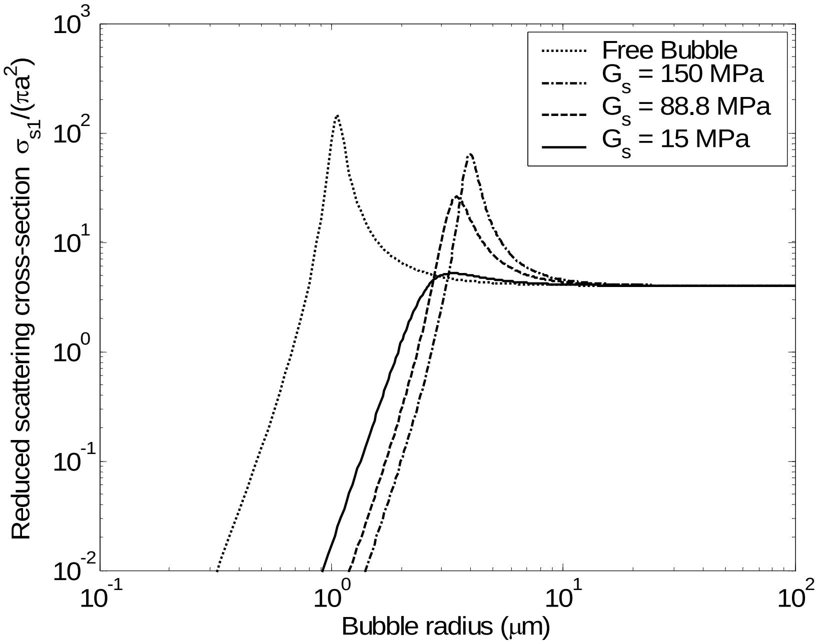

Figure 2.13 Replica of Figure 8 from Church [62] displaying the fundamental reduced scattering cross-section (dimensionless) for a shelled bubble as a function of radius for different stiffnesses G_s = 15, 88.8, and 150 MPa at a driving frequency of 3.5 MHz.

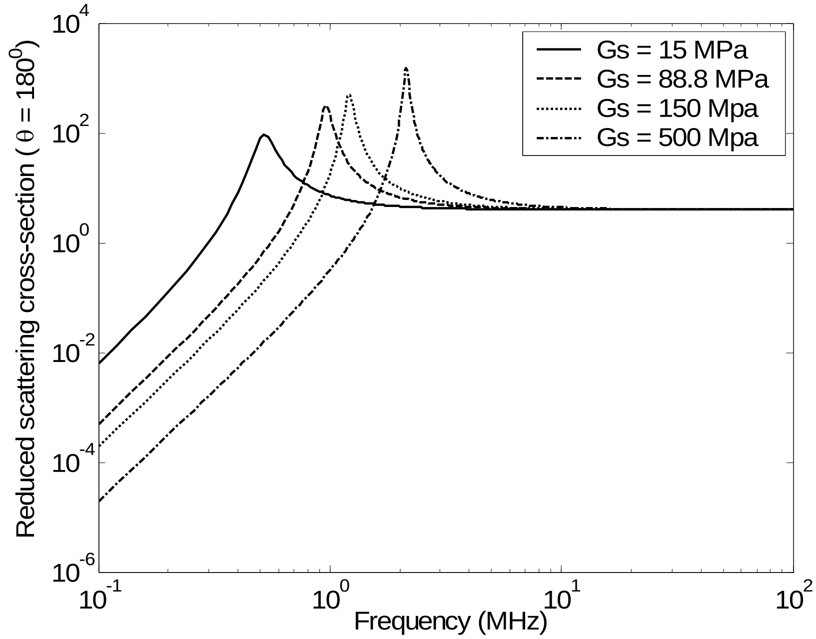

Figure 2.14 Reduced backscattering cross-section (dimensionless) for an 8 μm radius contrast agent with different shell stiffnesses Gs = 15, 88.8, 150, and 500 MPa.

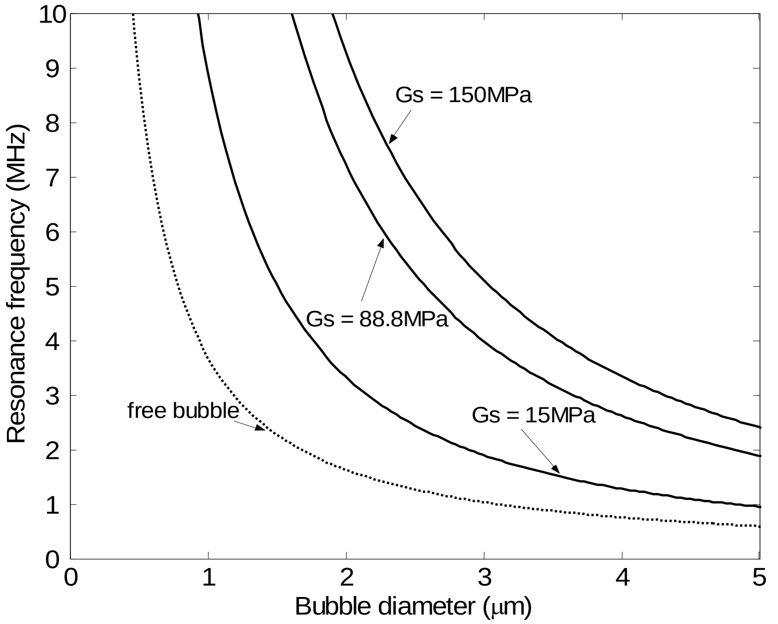

Figure 2.15 Resonance frequency as a function of bubble diameter for a contrast agent with shells of different stiffness Gs = 15, 88.8, and 150 MPa and for a free bubble.

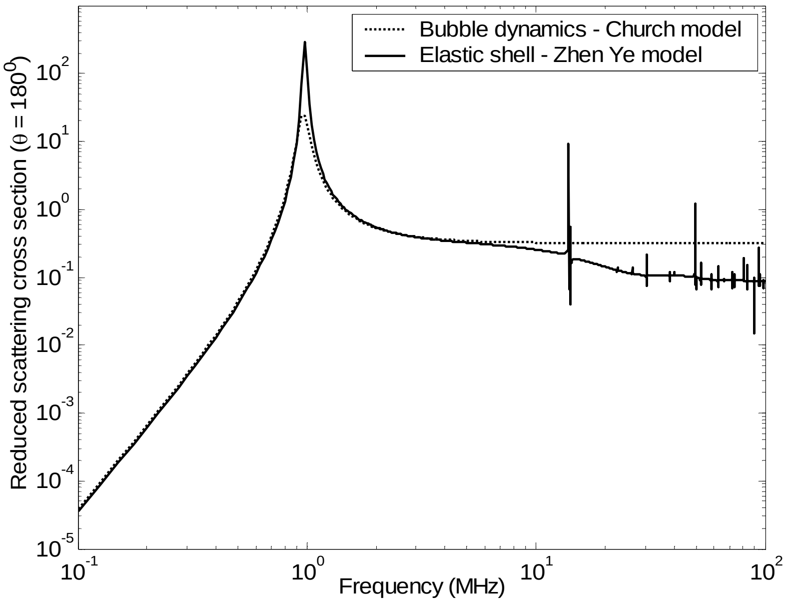

Figure 2.16 Comparison of the reduced scattering cross section (dimensionless) versus frequency of an 8 μm radius contrast agent with shell stiffness Gs = 88.8 MPa using both the bubble dynamics and elastic shell models.

2.5 Summary

In the present chapter a variety of single-particle models were introduced, which enabled us to predict and understand the way sound scatters from spheres, cylinders, and microbubble contrast agents. The purpose of this investigation was to use the developed models to compare scattering from red blood cell suspensions to scattering by a single rigid scatterer or by suspensions of microbubble contrast agents. The next chapter will therefore introduce a convenient formulation, known as the signal-to-noise ratio (SNR), which facilitates this comparison, and accounts for the presence of multiple scatterers.

It is important to note that not all the models produced in this chapter will ultimately be used for validating experimental data. For computational convenience, red blood cells were modeled using the Born approximation (Sec. 2.2.4) and assuming the scatterers were acoustically small. When comparing a rigid cylindrical scatterer to suspensions of red blood cells, the full elastic solution (Sec. 2.3) was used for the cylinder. Finally, the modeling of microbubble contrast agents used the first-order scattering cross-section predicted by the Church model for sound radiation by a shelled microbubble (Sec. 2.4.2). The Church model was ultimately implemented due to its computational simplicity and because the effect of higher order resonance modes, which it fails to predict, was not deemed important in practice.

Chapter 3

Modeling a Collection of Scatterers

After having studied single particle scattering models, the next question is: “How can a collection or suspension of scatterers be modeled?” The problem is simple if one assumes that the scatterers do not interact, because then scattering from a collection of particles is the sum of the contributions from each individual scatterer. This is also known as the single scattering approximation. The problem is significantly more complicated if the field scattered by an individual particle affects the response of its neighbors. Such multiple scattering effects have been investigated by Waterman and Truell [12], Foldy [4], and Commander and Prosperetti [49]. A criterion, known as the Waterman and Truell condition [12], was developed to assess the significance of multiple scattering effects and whether these can be safely ignored. Single scattering holds if

$$\frac{\eta\sigma_s}{k} \ll 1 \,, \tag{3.1}$$

where η is the number of scatterers per unit volume or number density, σ_s is the scattering cross-section of each individual scatterer, and $k = 2\pi/\lambda$ is the real part of the wavenumber. Equation

(3.1) states that in the case where the multiple scattering field produced by the insertion of one particle is much smaller than the field produced by the incident wave, multiple scattering effects can be neglected.

The experimental conditions of the present study were such that the Watermann and Truell condition was always fulfilled. For the case of red blood cells, in the limit where $k_2a \ll 1$, the scattering cross-section (Secs. 2.2.3-2.2.5) is of order $k_2^4a^6$. Since the maximum allowable number density is $\eta=a^{-3}$ (at which point the scatterers fill the entire volume), the criterion in Eq. (3.1) becomes $(ka)^3 \ll 1$, which is always satisfied. On the other hand, the worst-case scenario for suspensions of microbubble contrast agents occurs at the largest mean radius ($a=2.25\ \mu m$), lowest frequency ($f=5\ MHz$) and maximum concentration ($\eta=6.5x10^5$ $microbubbles/cm^3$) used in the experiments. For these values, Eq. (3.1) reduces to $\eta\sigma_s/k \approx 5\times10^{-4} \ll 1$. It is therefore concluded that multiple scattering effects can be neglected when modeling scattering by suspensions of red blood cells or contrast agents in the present context.

3.1 The Backscatter Coefficient

In many experimental configurations, including the one used in the present study, the transducer is used both as a transmitter and as a receiver. This configuration is termed “monostatic” and implies that, the receiver detects backscattering from the target. In addition, the aperture of the acoustic receiver is of finite size, allowing only a portion of the scattered power to be detected. A standard expression, called the “Backscatter Coefficient” (BSC) has therefore been developed to model this specific scenario. This coefficient quantifies the acoustic power backscattered, per unit incident intensity, per unit solid angle, per unit volume of insonified medium. It has units of $\text{cm}^{-1}\text{sr}^{-1}$ [25, 65].

Based on its definition, the BSC is equal to the differential backscattering cross-section of the entire medium containing the inhomogeneities, per unit volume of insonified material. For a suspension of scatterers of a known number density (η), and assuming single scattering, the BSC can be written as

$$BSC = \eta \sigma_{dbs} , \tag{3.2}$$

where σ_{dbs} is the differential backscattering cross-section for one scatterer. Given the single-particle scattering models derived in Chapter 2, the differential backscattering cross-section in Eq. (3.2) can be computed as

$$\sigma_{dbs} = \left| \Phi\left(\theta = 180^0 \right) \right|^2 , \tag{3.3}$$

where Φ is the angular distribution function for the elastic sphere and cylinder, fluid sphere, and elastic shell given in Secs. 2.2.1-2.2.4, Sec. 2.3 and Sec. 2.4.1.

For the case of microbubble contrast agents given in Sec. 2.4.2 using the Church model, the differential backscattering cross-section can be written as

$$\sigma_{dbs} = \frac{\sigma_s}{4\pi} , \tag{3.4}$$

where σ_s is the scattering cross-section for a single bubble. In the latter case, a specific formulation for the angular distribution function was not derived and the differential backscattering cross-section was therefore determined from the scattering cross-section, assuming omni-directional scattering.

The BSC defined in Eq. (3.2) provides a very convenient way of relating theory to experiment when investigating a specific volume containing a suspension of scatterers, assuming multiple scattering effects can be ignored. Section 3.1.1 will illustrate a specific derivation of the BSC for the case of red blood cells.

3.1.1 Case of red blood cells

Backscattering from a suspension of red blood cells has been a topic of investigation by Reid et al. [24], Atkinson et al. [26], Shung et al. [27], Borders et al [32], and Angelsen [34]. Experimental measurements indicate that the BSC increases linearly up to a hematocrit of about 5% [72], followed by a slower increase up to about a 15-20% hematocrit value. Beyond this level, the BSC exhibits a decrease and tends to zero after 70% hematocrit. With the use of a stochastic theory developed by Twersky [16, 33], Shung [39] elaborated a theoretical expression for determining the backscattering coefficient from a suspension of red blood cells.

The first case considered is that of incoherent scattering. In this case the hematocrit values are very low (0-5% hematocrit) and therefore scattering by each particle can be considered to be completely uncorrelated. As explained in Sec. 3.1, the BSC can then be defined as the differential backscattering cross section for a single scatterer, σ_{dbs}, multiplied by the number of scatterers per unit volume η

$$BSC = \eta\sigma_{dbs} = \frac{H}{V_c}\sigma_{dbs}\,, \tag{3.5}$$

where H is the hematocrit value, and V_c the mean cell volume. However, as the hematocrit is increased and the particles are brought into closer proximity, the scattered waves from each of the scatterers may interact in either a constructive or a destructive manner. At this point, the positions of the particles are no longer uncorrelated leading to what is known as "coherent scattering". An expression that accounts for such coherent effects was first proposed by Shung [39] using statistical mechanics theorems developed by Twersky [16, 33] with the introduction of the so-called "packing factor (*W*)"

$$BSC = W\eta\sigma_{dbs} \tag{3.6}$$

where W is

$$W = \frac{(1-H)^4}{(1+2H)^2}. \tag{3.7}$$

As shown in Figure 3.1, the expression for the BSC of red blood cells obtained by combining Eqs. (3.6) and (3.7) predicts an increase in the BSC up to 13% hematocrit, followed by a decrease tending to zero. This formulation was found to be in excellent agreement with data taken by Wang and Shung [65], Yuan and Shung [47, 48], and Maruvada et Al. [75].

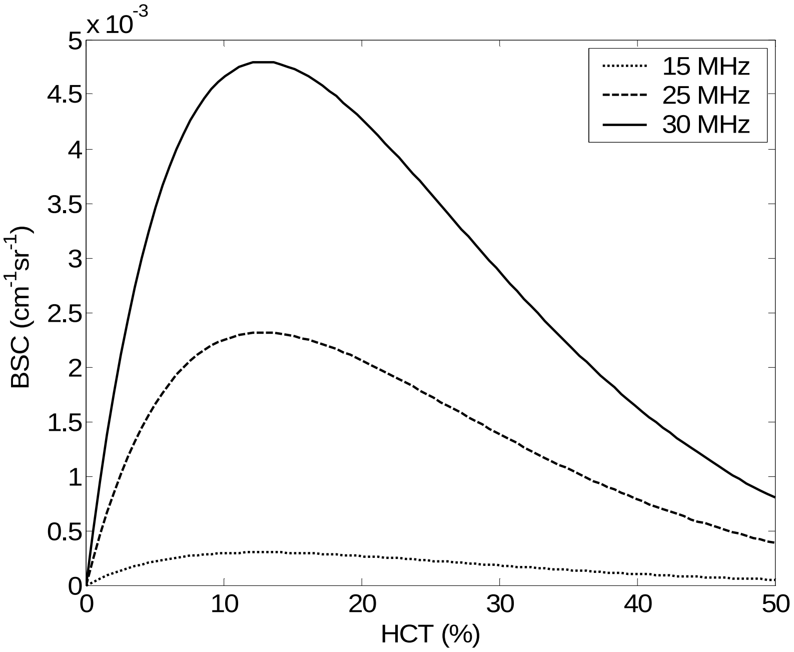

Figure 3.1 Theoretical calculation of the BSC for a suspension of red blood cells in saline as a function of hematocrit (HCT) at 15, 25, and 30 MHz.

3.2 Attenuation

So far, all theoretical formulations have been performed assuming a non-lossy medium. In reality, media that contain populations of scatterers such as red blood cells or contrast agent microbubbles attenuate sound waves traveling through them. The term ‘attenuation’ includes both the energy lost through absorption (conversion of acoustic energy into thermal energy via viscous heating), and the energy lost through scattering. Assuming no multiple scattering is present, the intensity of a plane wave of initial intensity I_0, traveling through a medium of thickness y can be written in standard form as [21]

$$I = I_0 \exp\left[-\left(\sum_r \eta(r)\sigma_e(r,f)\right)y\right] = I_0 \exp\left[-\alpha_I y\right]. \tag{3.8}$$

The term $\eta(r)$ represents the number of scatterers of radius r per unit volume and $\sigma_e(r,f)$ is the extinction cross-section of a scatterer of radius r, which is defined as the total power extinguished by the scatterer per unit incident intensity at frequency f. The attenuation coefficient for intensity is then given by α_I and has units of nepers (*Np*) over length, where a neper is a dimensionless quantity given as $10\log_e(power\ ratio)$.

It is important to mention that the attenuation coefficient given by α_I in Eq. (3.8) differs from the theoretical linear amplitude attenuation coefficient α_A by a factor of 2. Knowing that the intensity is proportional to the square of the pressure amplitude, Eq. (3.8) can be rewritten as

$$I = I_0 e^{[-2\alpha_A y]}, \tag{3.9}$$

which allows us to relate the intensity and amplitude attenuation coefficients by

$$\alpha_I = 2\alpha_A. \tag{3.10}$$

It is important to notice that the attenuation coefficients α_I and α_A are defined in Np/cm. The conversion to the more commonly used units of dB/cm, is given by

$$\begin{aligned} \alpha_{dB} &= \alpha_A(20\log e) = 8.69\alpha_A \\ \alpha_{dB} &= \alpha_I(20\log e) = 4.34\alpha_I \quad . \end{aligned} \tag{3.11}$$

All the attenuation coefficients determined experimentally or computed in the present work will be given as α_{dB}.

3.3 Signal-to-Noise-Ratio (SNR)

The main focus of the current investigation is to determine how the power backscattered by a strong scatterer (“signal”) and the power backscattered by a suspension of weak scatterers (“noise”) vary relative to each other as a function of frequency. It is therefore important to devise a theoretical model describing this quantity that can then be compared to experimental results.

In the present section, solutions for the SNR in the 5-30 MHz frequency range will be determined with the use of the single particle scattering models explained in Chapter 2. The first investigation will consider the case of a wire (strong scatterer) in a suspension of red blood cells (weak scatterers). This example will be used as a proof of concept to demonstrate that there is a decrease in the SNR as the frequency increases, and was implemented due its simple geometry, and ease in the experimental setup and data collection. The investigation will then look at the case of a suspension of microbubble contrast agents (strong scatterers) in a suspension of red blood cells (weak scatterers). The latter model will account for the size distribution of the particular suspension of microbubbles used but will again assume that the two populations of scatterers, namely the microbubbles and red blood cells, do not interact with each other.

3.3.1 Elastic cylinder in a suspension of red blood cells

The first experiment performed in the present investigation consisted in embedding a 35 μm fiberglass wire in a suspension of red blood cells at 13% hematocrit (see Sec. 4.3.2 for a detailed description of the experimental setup). The goal was to compare the return from a single strong scatterer (cylinder), to the return from a suspension of weak scatterers (red blood cells). The model is based on a comparison of the BSC for an elastic cylinder and the BSC for a suspension of red blood cells. The SNR is defined as the sum of the BSC of the elastic cylinder and the BSC of blood over the BSC of blood alone:

$$SNR_{cyl} = 10\log\left(\frac{BSC_{cyl} + BSC_{rbc}}{BSC_{rbc}}\right), \qquad (3.12)$$

where the subscript *cyl* represents the cylinder and *rbc* the suspension of red blood cells. Solutions for BSC_{cyl} were obtained by solving for Eqs. (3.2) and (3.3) using the angular distribution function (Φ) for an elastic cylinder as in Sec. 2.3 and setting the number density η to unity. Figure 3.2 shows a plot of the BSC_{cyl} for a 35 μm fiber glass wire with a density of $3.8\text{x}10^3$ kg/m^3, Young's modulus of 65 GPa, and a Poisson's ratio of 0.24 compared to the BSC_{rbc} of a 13% hematocrit suspension of red blood cells with a mean cell volume of $87\text{x}10^{-12}$ m^3, a density of $1.087\text{x}10^3$ kg/m^3, and a compressibility of $3.55\text{x}10^{-11}$ cm^2/dyne. From the results given in Figure 3.2 one can then compute the SNR using Eq. (3.12) with the resulting plot given in Figure 3.3. As the frequency increases, the BSC of the suspension of red blood cells approaches the BSC of the cylinder causing a reduction in the SNR of about 20 dB in the 5-30 MHz frequency range.

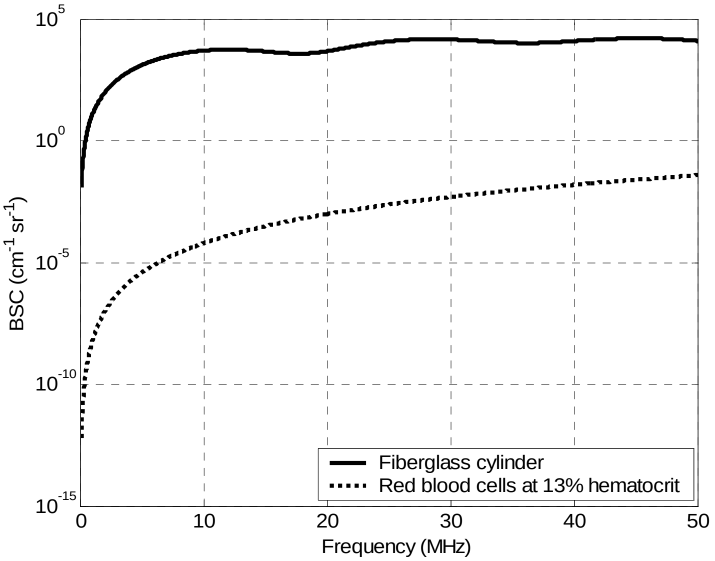

Figure 3.2 Computed BSC for a 35 μm fiberglass cylinder compared to that of a suspension of red blood cells at 13% hematocrit.

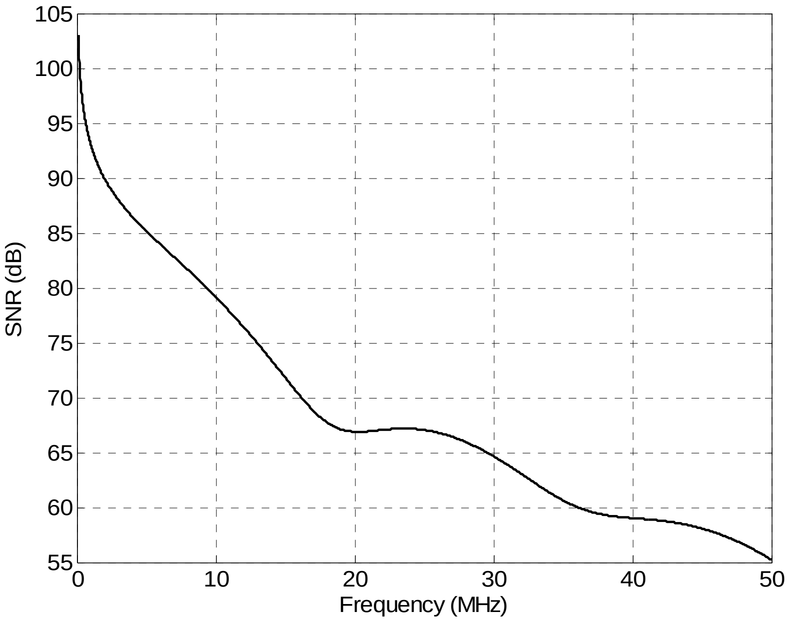

Figure 3.3 Predicted signal-to-noise-ratio (SNR) as a function of frequency for a fiberglass wire in a suspension of red blood cells at 13% hematocrit.

3.3.2 *Optison*® microbubbles in a suspension of red blood cells

Similarly to the case of the elastic cylinder in a suspension of red blood cells, the SNR was also computed for a suspension of *Optison*® microbubbles (strong scatterers) in a suspension of red blood cells (weak scatterers). Consequently, the SNR for microbubbles in blood can be written in a similar fashion as that given in Sec. 3.3.1 with

$$SNR_{opt} = 10\log\left(\frac{BSC_{opt} + BSC_{rbc}}{BSC_{rbc}}\right), \tag{3.13}$$

where the subscript *opt* refers to the *Optison*® microbubbles and the subscript *rbc* to the red blood cells. As previously stated, the solution for $\mathrm{BSC_{rbc}}$ was derived in Sec. 3.1.1 while $\mathrm{BSC_{opt}}$ can be computed using either the elastic shell theory developed by Ye and Hasegawa and explained in Sec. 2.4.1 or by the Church model given in Sec. 2.4.2. Any of the two models can be effectively implemented, with the Church model being less computationally intensive. Due to the fact that

Optison® microbubbles are not monodisperse but have a rather large size distribution [76], this size distribution must also be included in the model. In the following section a derivation of the SNR for a suspension of *Optison*® microbubbles will be illustrated using the Church model with the addition of the size distribution of microbubbles.

BSC of microbubbles with size-distribution

Given that every batch of *Optison* microbubbles has a specific size distribution [70], a method of discretization was used to take this size distribution into account. At each frequency the differential backscattering cross-section was discretized as a function of radius by defining a specific bin size. An example given in Figure 3.4 shows the discretization for a contrast agent with shell parameter *Gs* = 88.8 MPa, at 10 MHz and a 0.25 µm bin size.

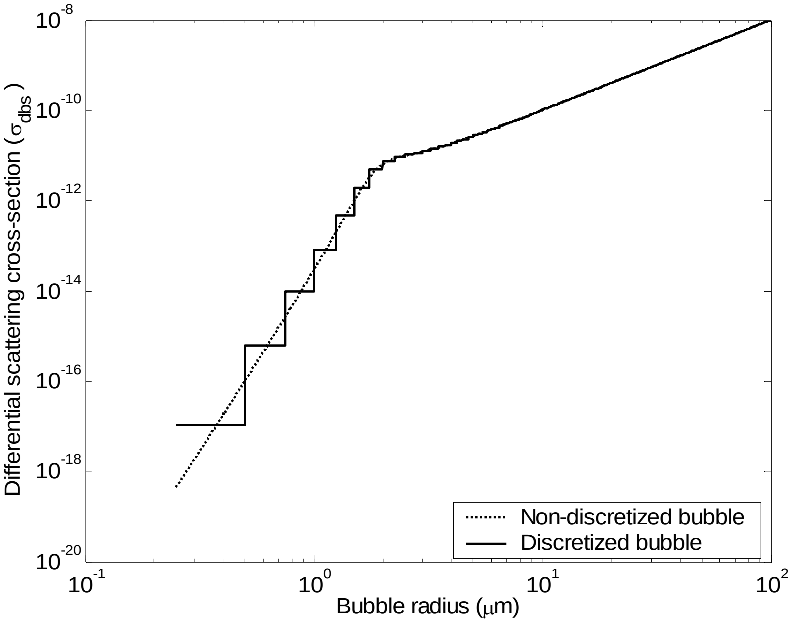

Figure 3.4 Comparison between the continuous and discretized curves of the differential backscattering cross section as a function of radius for a contrast agent with shell parameter Gs = 88.8 MPa at 10 MHz.

Given the formulation of the BSC in Eq. (3.2), one may define a corrected BSC as a function of bubble radius for a specific frequency using the discretized differential scattering cross-section shown in Figure 3.4

$$BSC_{corr}\left(r,f\right)=\sum_{n=1}^{\#bins}\eta_n\left(r\right)\sigma_n(r,f)\,. \tag{3.14}$$

The number density $\eta_n(r)$ is that corresponding to bubbles of radii falling within each specific bin and the differential scattering cross-section $\sigma_n(r,f)$ is the discretized one given in Figure 3.4. The resulting BSC is therefore the sum of the BSC's in each bin for a specified range of radii and a specific frequency. Repeating the process at every frequency for the desired bubble radius size distribution and bin size, one can obtain the BSC as a function of frequency for a given size distribution of *Optison*® microbubbles.

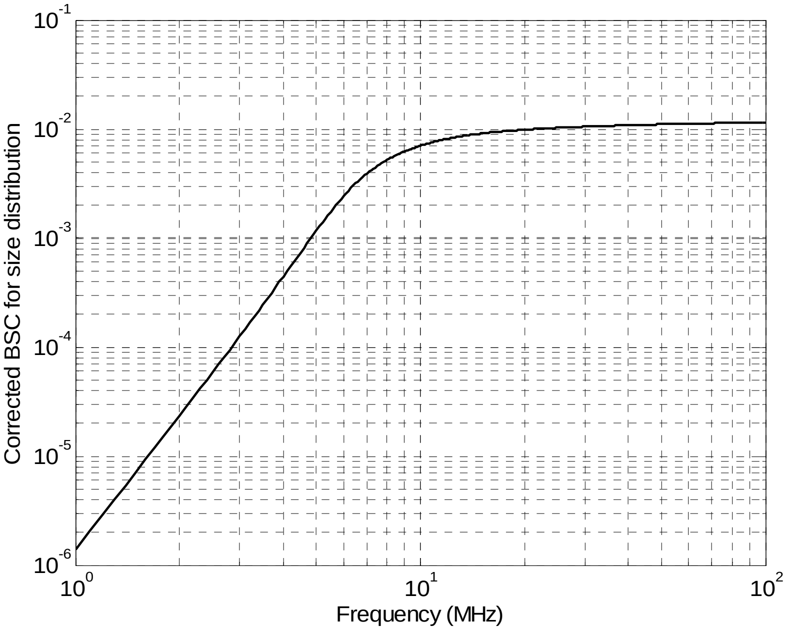

Figure 3.5 BSC as a function of frequency for a suspension of *Optison*® microbubbles with shell parameter Gs= 88.8 GPa, a number density of 6x10^5 bubbles/ml and a size distribution given by batch #2 in Ostensen [76].

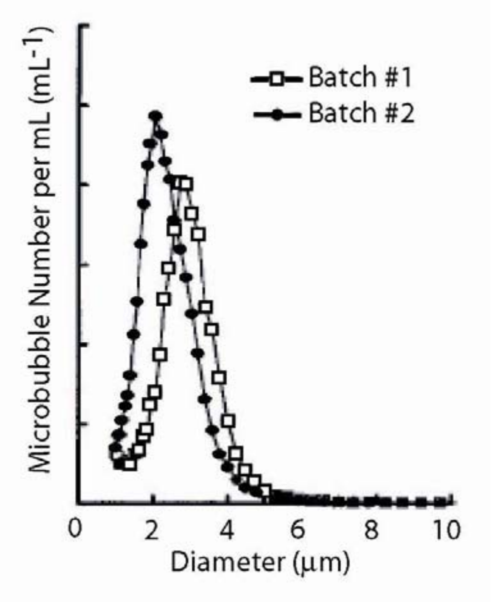

Figure 3.6 Size distribution of *Optison®* microbubbles used for determining the BSC plot given in Figure 3.7. Figure obtained from Ostensen [76] and Batch #2 was used for the BSC calculation.

Figure 3.5 shows the resulting BSC corrected for a size distribution (batch #2) given in a recent study by Ostensen et al. [76], where two batches of *Optison*® microbubbles were measured. This size distribution is shown in Figure 3.6. It is important to notice how the effect of having bubbles of different sizes has caused the curve to not display a resonance any more.

After having implemented a model for determining the BSC of a suspension of microbubbles, one can now compare the given result with that of a suspension of red blood cells, and consequently determine the SNR given by Eq. (3.13). Figure 3.7 shows the BSC of a suspension of red blood cells at 13% hematocrit and that of a suspension of *Optison*® microbubbles at three different concentrations.

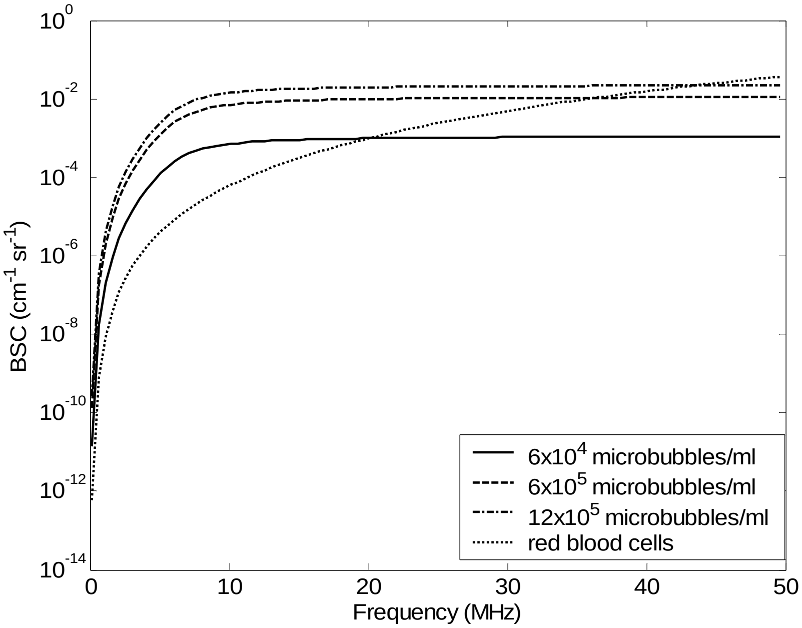

Figure 3.7 BSC for a suspension of different concentrations of *Optison*® microbubbles corrected for size distribution and a suspension of red blood cells at 13% hematocrit as a function of frequency.

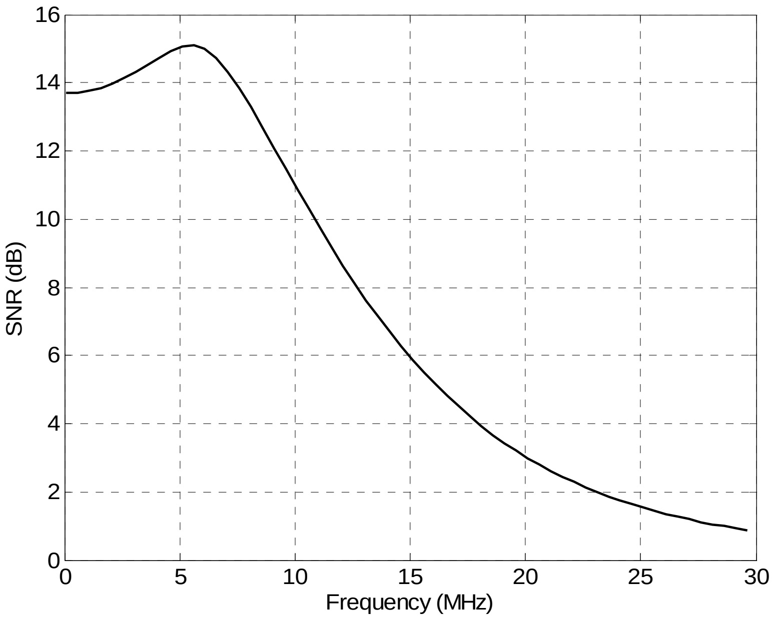

Figure 3.8 SNR of a suspension of *Optison*® microbubbles with a 6x10^4 microbubbles/ml number density and a suspension of red blood cells at 13% hematocrit.

From the results in Figure 3.7 one can observe how the BSC from the suspension of red blood cells is about the same as that of a 6x10^4 microbubbles/ml suspension of *Optison*® (the typical clinical dosage) at around 20 MHz. This result demonstrates how the microbubble contrast agents do not provide image enhancement above 20 MHz at that particular concentration, as illustrated by the SNR in Figure 3.8. Similarly to what was predicted in the previous plot, one can observe from Figure 3.8 how the SNR approaches 0 dB as the frequency increases, where the scattering from the red blood cells dominates over the scattering from the microbubbles.

It is important to note that when computing the SNR both in the case of an elastic cylinder in a suspension of red blood cells and a suspension of *Optison*® microbubbles in a suspension of red blood cells, we are assuming that no multiple scattering effects occur and that the two populations of scatterers do not interact.

Chapter 4

Experimental Setup and Procedure

4.1 Apparatus

We seek an experimental apparatus for distinguishing and comparing the scattering from single strong scatterers (elastic spheres and cylinders), collections of strong scatterers (microbubble contrast agents), and a collection of weak scatterers (red blood cells) at different frequencies. The decision was made to implement an active cavitation detector (ACD) operating at 5, 15, 25, and 30 MHz in a general setup that allowed high flexibility (quick exchange of investigated medium such as blood, water, and saline), three-dimensional movement capabilities, and high repeatability of measurements. The following sections will provide an overview of the apparatus and a more detailed description of the main components.

4.1.1 General overview

The general layout of the experimental setup can be split into three main components: the tank assembly, the transducer, and the ACD (see Figure 4.1). The tank assembly consisted of a water-filled plexiglass tank mounted on an optical table with a sample holder placed in it. The sample holder consisted of a square pipe with an opening in its front and back faces wrapped in a latex membrane, containing the investigated fluid (blood or saline). It was mounted on three micrometer stages for three-dimensional positioning. The focused narrowband ultrasonic transducer (see Table 4.1) was placed directly in front of the opening in the sample holder as shown in Figure 4.1. The ACD is a customized instrumentation package that served to drive the focused transducer (transmit mode) and sensed the backscattered echo signals, routing these RF signals to a digital oscilloscope (receive mode). The oscilloscope was then connected via GPIB to a data-acquisition computer that collected the relevant data. The following sections will describe each instrumentation component in greater detail.

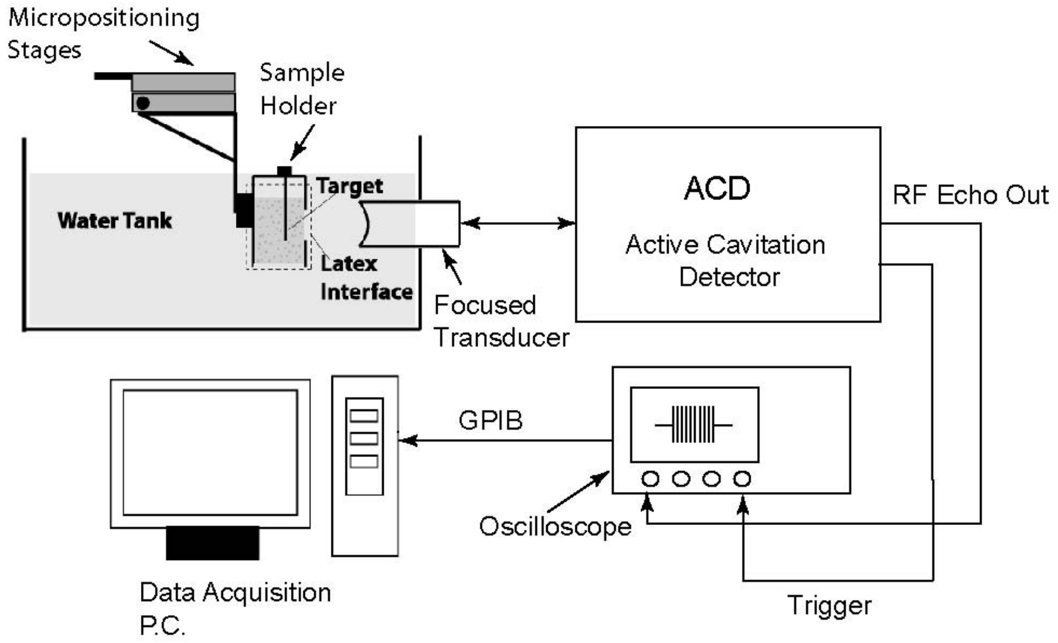

Figure 4.1 General overview of the experimental setup used for the present investigation.

4.1.2 Tank assembly

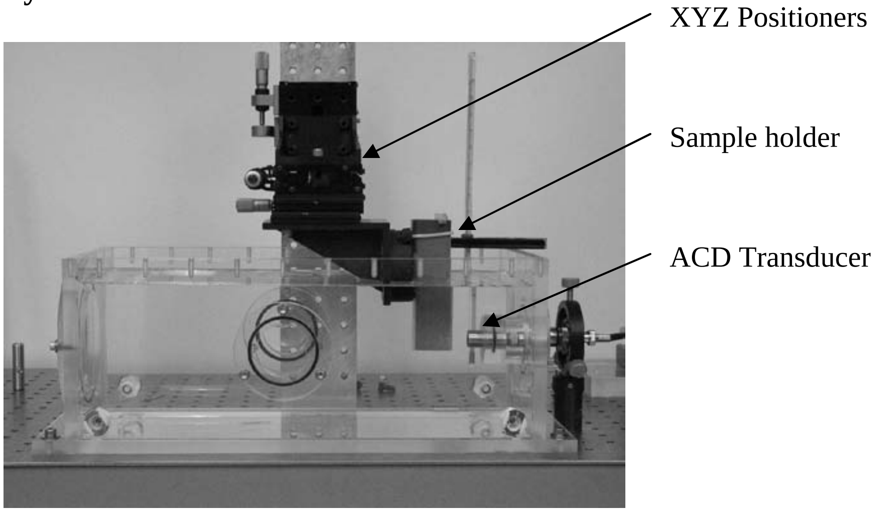

Figure 4.2 Photograph of the tank assembly, consisting of a plexiglass tank, sample holder with micrometer stages, thermometer, and high frequency submersible transducer.

Figure 4.2 illustrates the tank assembly. The assembly consisted of a 41 cm x 18 cm x 16 cm tank filled with distilled and degassed water, with a high frequency submersible transducer wall-mounted on one side (described in Sec. 4.1.3), a sample holder covered with a latex membrane (see Figure 4.3 and Figure 4.4), and a thermometer for monitoring the water temperature.

Attention was placed on the design of the sample holder since it contained the suspensions of red blood cells as well as the cylindrical wire targets used for the SNR experiments and the attenuation experiments. The holder consisted of a 3.5 cm x 3.5 cm x 11.5 cm PVC pipe with a 3 mm wall thickness and openings on two opposite sides. A latex membrane was stretched over the top of the pipe forming a sealed container with acoustically transparent windows. The latex membrane was used because it is known to be a very good acoustic transmitter [27], allowing most of the incident intensity to reach the sample. It was of great importance to keep the latex membrane as taut as possible in order to keep the surface of the interface unaltered between measurements.

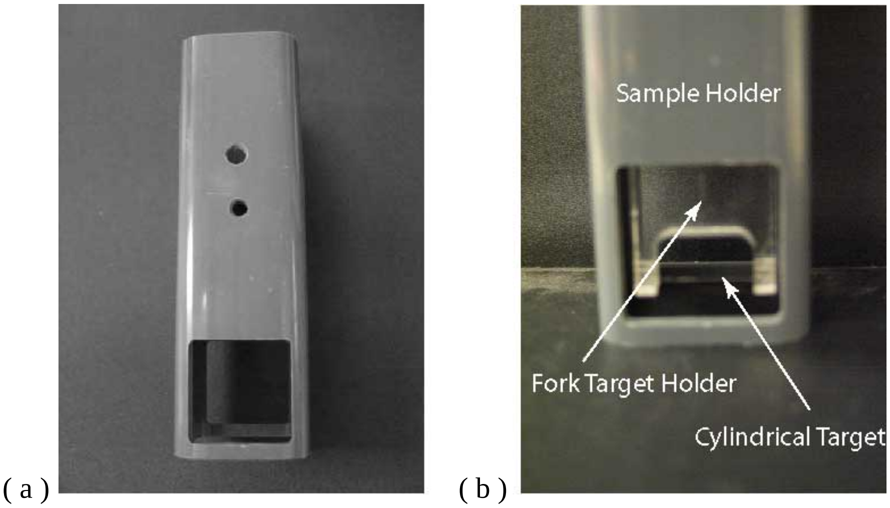

Figure 4.3 (a) Sample holder used as a chamber for the blood and consisting of a PVC pipe with an opening on each side. (b) Sample holder and fork target holder assembly with the cylindrical target attached.

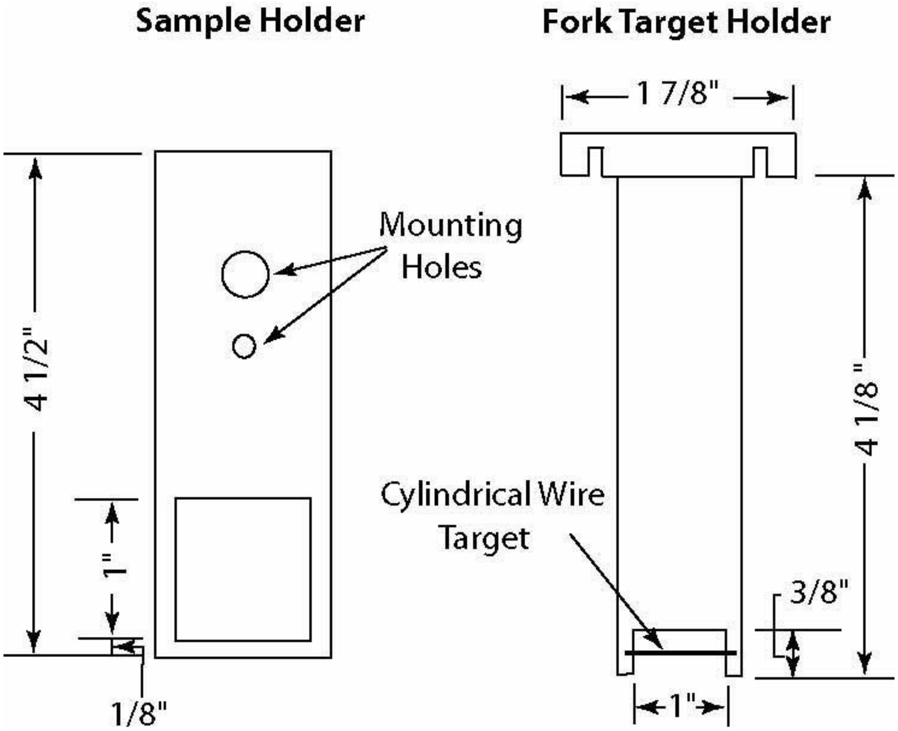

Figure 4.4 Schematic of the sample holder and fork target holder with some relevant dimensions. The thickness of the sample holder wall is 1/8” and that of the fork target holder is 1/4”.

In order to mount the cylindrical targets (fiberglass and tungsten wire) inside the sample holder, an additional element was designed. This element consisted of a plexiglass fork with the target stretched across it that fastened to the top of the sample holder and had the ability to slide along the propagation axis of the wave. In this way, the fork could be placed at the desired distance from the latex interface and had enough frictional force to prevent it from moving throughout the whole experiment.

The sample holder assembly was mounted on three orthogonal micropositioning stages (Newport 423 Series) which allowed movement along three different axes with a resolution of approximately 5 µm. Three-dimensional movement capabilities were key to the experiment and allowed the target to move within the water tank until it lay exactly in the focus of the sound field. The targets used were either 25 µm diameter tungsten cylindrical wires or 35 µm diameter cylindrical fiberglass wires.

4.1.3 Transducer characteristics

Four different transducers were used in the present investigation (see Table 4.1 for specifications). Each transducer consisted of an unbacked, high frequency, single element, focused transducer with a 2.5 cm focal length with the exception of the 5 MHz Panametrics transducer which was backed with a quarter wavelength matching layer. The appropriate transducers were determined by four main factors: resonance frequency, bandwidth, focal length, and beam diameter.

The frequency range was based on the clinical relevance, to mimic typical diagnostic frequencies, and the long wavelength scattering theory approximation ($ka \ll 1$), for a simplification in the modeling. In addition, there was a need for a large enough range that could allow a relevant decrease in the SNR and a similar backscatter from the strong scatterers and the weak scatterers as the frequency was increased. The 5-30 MHz range was found to satisfy these specifications for scattering in blood.

Transducer	Frequency (MHz)	Focal Length (cm)	Element Diameter (cm)	Computed -3 dB Beam Diameter (μm)
Panametrics A309S	5	2.54	1.27	612
Harisonic D8500	15	2.54	0.64	408
Harisonic T3315	25	2.54	0.64	245
Harisonic G1010	30	2.54	0.95	136

Table 4.1 Transducer characteristics provided by the manufacturer.

Bandwidth was important because it is a means of broadband noise rejection. In the present experiment, the bandwidth of the transducer signal also depended on the bandwidth of the bandpass filter used for each experiment. It was therefore decided to always excite the transducer with a pulse duration long enough to achieve 20 cycles at steady state. Twenty cycles at steady state were found to give a sufficiently narrowband signal (250 kHz at 5 MHz, 750 kHz at 15 MHz, 1.25 MHz at 25 MHz, and 1.5 MHz at 30 MHz) while maintaining a short enough pulse to distinguish between the latex and target reflections.

The focal length of each transducer was mainly determined by the availability and manufacturing cost. All available transducers had a 2.5 cm focal length which was also found to be particularly suitable for avoiding interference between the incident and scattered pulses.

Another important parameter to consider when using focused transducers was the -3 dB beam diameter (BD). In order to use a plane wave approximation in the theoretical formulations, the scatterer or scatterers taken into consideration must be much smaller than the beam diameter of the transducer. For the case of the elastic cylinder of diameter d, for example, $d \ll$ BD must be satisfied. The BD sizes given in Table 4.1 were calculated from the following relation [78]

$$BD = \frac{1.02Fc}{f_0 D} , \tag{4.1}$$

where F is the focal length of the transducer, c is the speed of sound in the investigated medium, f_0 is the frequency, and D is the element diameter.

4.1.4 The Active Cavitation Detector (ACD)

Overview

The ACD consisted of the signal generation and signal detection circuitry developed by Roy [43, 50] and designed to be used for the detection of cavitation *in vitro*. The initial purpose of the ACD was to implement a device with sufficient sensitivity for detecting the presence of micron-sized cavitation microbubbles lasting less than a microsecond. The main differences between the present setup and the original were the use of only one transducer both for the transmit signal and the receive signal as well as the employment of four frequencies (5, 15, 25, and 30 MHz) rather than a single 30 MHz center frequency.

The basic functions performed by the ACD consisted in gating a continuous-wave signal to produce an RF tone burst of a desired duration and repetition frequency. When transmitting, the amplified tone-burst drove a narrowband transducer producing the acoustic field. On the other hand, when receiving, the transducer detected the backscattered signal which was preamplified and displayed on the oscilloscope.

The ACD can be split into four main components: the signal generation circuitry (main bang), the transmit-receive (T-R) switch, the signal detection circuitry, and the time base circuitry. The main bang consisted of a gated continuous wave used to produce a tone burst of the appropriate length with a center frequency of either 5, 15, 25 or 30 MHz. The T-R switch was an electronic switch that connected the transducer to the signal generation (transmit mode) or the signal detection circuitry (receive mode) respectively. The signal detection circuitry amplified the signal from the T-R switch and filtered it with a bandpass filter centered at the correct frequency. The signal could then be digitized, displayed (LeCroy LT 264 oscilloscope) and stored. Finally, the time base generation circuitry provided the gating signal of the main bang, the pulse repetition frequency, the oscilloscope trigger, the T-R switch transmit enable pulse, the backscattered signal gate, as well as all the control signals in the system.

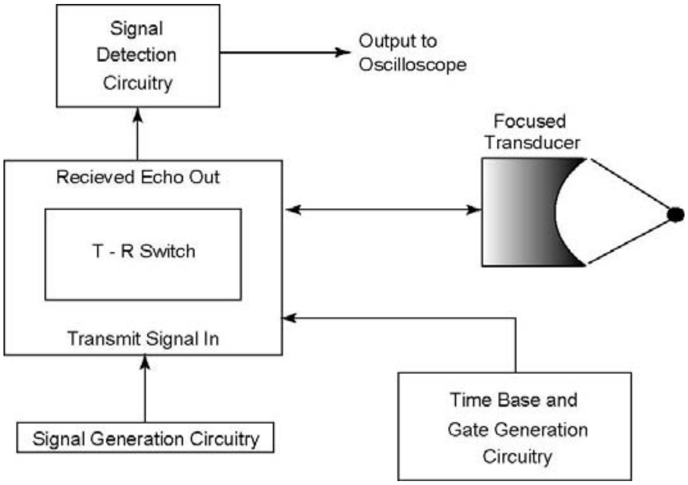

Figure 4.5 Block Diagram of the ACD.

Signal generation

Figure 4.6 shows a block diagram of the signal generation circuitry that produced the input signal to the T-R switch. A function generator (Agilent 8116A) produced a continuous wave of the desired frequency which was fed into a double balance mixer (DBM - Mini Circuits model ZAD-1HB) configured as an RF gate. The control signal into the gate consisted of a 20 mA current pulse produced by the system time base that could be adjusted to obtain the desired pulse length. The combination of the two signals produced the desired tone burst, which was output to a variable attenuator for signal level adjustment, followed by a variable gain RF power amplifier (Amplifier Research 10A110) for amplification.

Typical output voltages from the power amplifier with the function generator operating at 30 MHz and 950 mVpp and the variable attenuator set to -10 dB were 2.5 Vpp at minimum gain and 40 Vpp at maximum gain. The noise floor was measured to be 10 mVpp at all times.

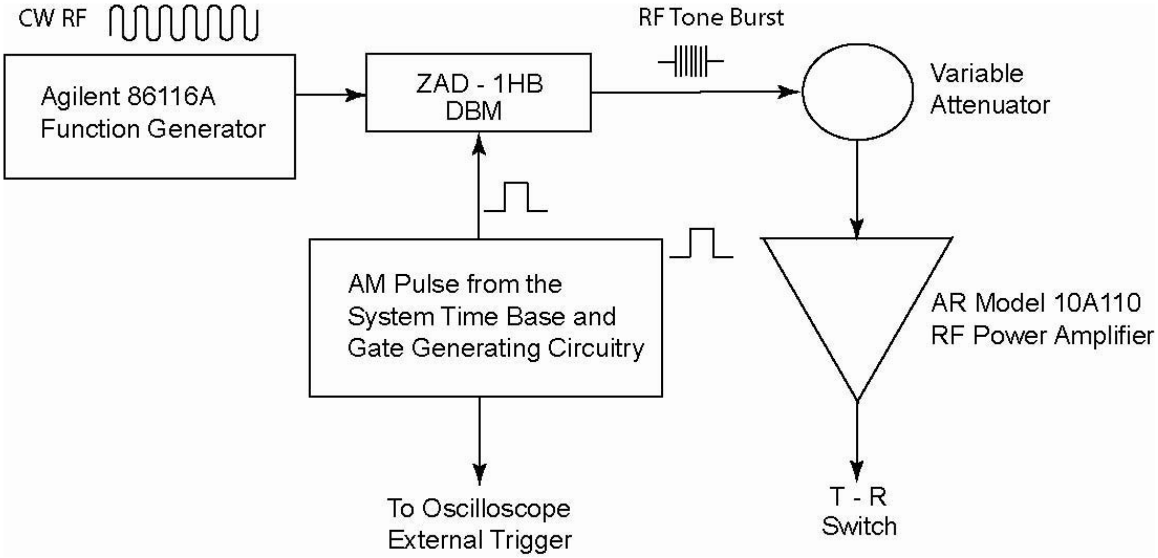

Figure 4.6 Block diagram of the signal generation system that delivers a tone burst to the T-R switch.

Transmit-Receive Switch (T-R switch)

The T-R switch was based on a design developed by Roy, which used pin diodes and a transmission line as a means of RF switching. While the full details will not be discussed here (see Roy [43, 50]), a detailed circuit diagram is presented in Figure 4.7. The functioning of the switch can be described by two modes: transmit mode and receive mode.

In transmit mode, a 60 mA dc current signal from the system time base was fed through the resistor labeled R1, causing the pin diodes P1 and P3 to conduct. When activated, the pin diodes had a very low impedance (0.75 Ω). The low impedance of pin diode P3 at the end of the transmission line was reflected as a very high impedance at the transducer side [43] causing the RF signal from the signal generation circuitry to travel through the pin diode P1, the back to back diodes P2 and to the transducer. The back to back diodes labeled P2 were used to reduce any broadband amplifier noise that leaked through P1. Because the impedance of the transducer (~50 Ω) was much smaller than the impedance looking into the transmission line, the detection circuitry was isolated from the main bang signal.

In receive mode, the 60 mA current pulse was turned off, causing the pin diodes to have a very high impedance (50 kΩ). This caused the RF signal exiting the transducer to go through the quarter-wave transmission line and into the signal detection circuitry, both of which had 50 Ω impedances and were therefore matched to the transducer. In addition, the pin diode P1 protected the power amplifier and the signal generation circuitry by isolating them from the transducer.

Typical transmit mode insertion loss defined as $20\log\left(V_T/V_{SG}\right)$ for the ACD operating at 30 MHz was found to be -4.2 dB, where V_T is the input voltage to the transducer and V_{SG} is the output voltage from the signal generation circuitry. Similarly, the transmit mode isolation, defined as $20\log\left(V_{SD}/V_T\right)$, where V_{SD} is the voltage entering the signal detection circuitry, was found to be -24.7 dB. Receive mode insertion loss was also determined for the 30 MHz ACD. This value was defined as $20\log\left(V_{SD}/V_T\right)$ with the T-R switch operating in receive mode and was found to be -0.9 dB. It is to be kept in mind that these loss and isolation figures apply to the T-R switch alone. They do not account for additional isolation elements contained in the signal detection circuitry (described below).

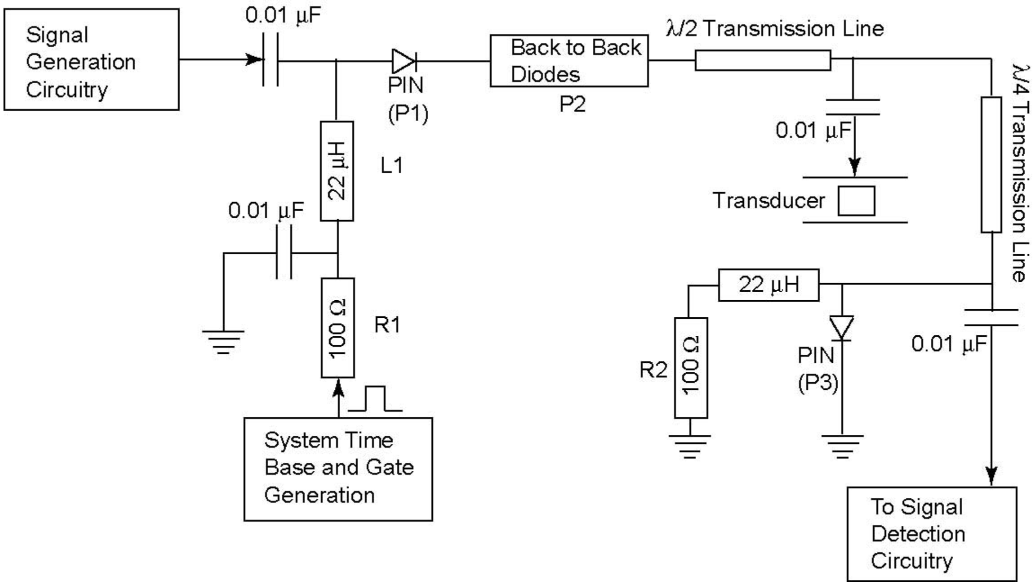

Figure 4.7 Transmit-Receive switch as given in Roy [43].

Signal detection

The signal detection circuitry was used to time gate and preamplify the receive signal from the transducer. The receive signal was fed through a voltage to current attenuator (VCA - Mini Circuits ZAS-3B) followed by a DBM (Mini Circuits model ZAD-1HB), both gated by the system time base. When operating the ACD at 30 MHz, the isolation of the VCA and DBM were measured to be 58.3 dB and 45.3 dB respectively, while their insertion loss was only -1.5 dB and -3.4 dB respectively. Thus, with these elements in place, the receive mode insertion loss and transmit mode isolation for the system became -5.8 dB and -128.3 dB respectively.

Following the mixers, the receive signal was then preamplified (Trontek W40D 65 dB) and passed through a narrowband passive bandpass filter centered at the same natural frequency as the transducer. Table 4.2 displays the specifications of the four bandpass filters used for the four different frequencies. Finally, the signal was displayed on a digital oscilloscope (LeCroy LT264) sampling at 1 GHz. Figure 4.8 gives a block diagram schematic of the signal detection circuitry. When operating at 30 MHz, the insertion loss of the bandpass filter was found to be about 6 dB, leading to a total receive mode *gain* of about 53.2 dB, after accounting for the mixers and the T-R switch receive mode loss, while maintaining a transmit mode isolation of 69.3 dB. With such a system, the transducer can be driven by a signal of the order of volts while detecting signals in receive mode on the order of microvolts.

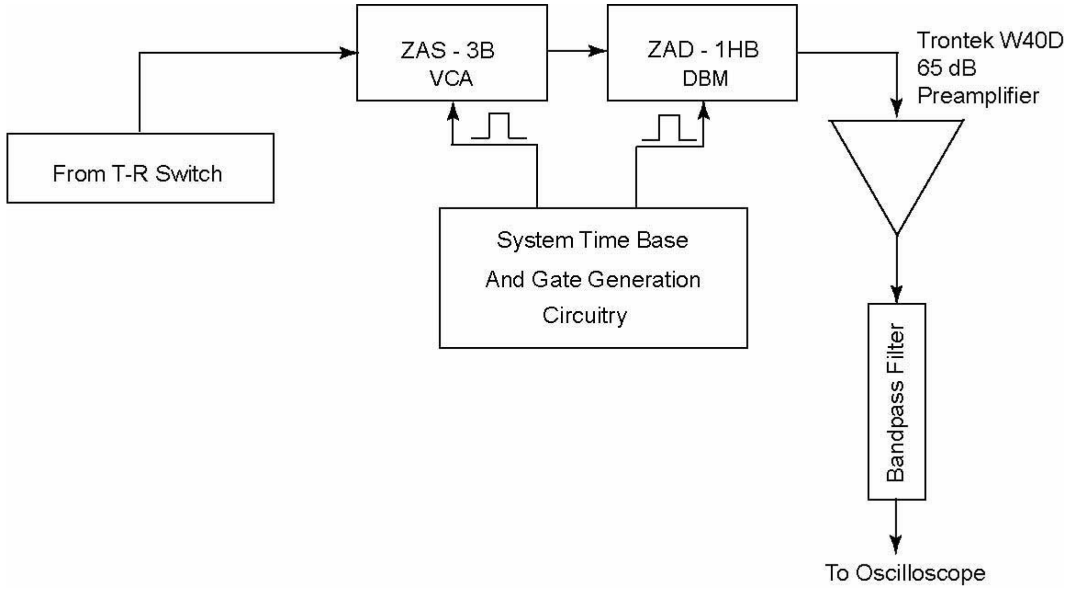

Figure 4.8 Block diagram of the signal detection circuitry.

Bandpass Filter	Center Frequency (MHz)	Bandwidth (MHz)	Insertion Loss (dB)	Stop-Band Attenuation (dB)
Wavetek BB4BB5/1	5	1	1.5	51
Wavetek AB4BB15/.75	15	0.75	4.5	46
Allen Avionics F062	25	1.25	2.5	50
Wavetek AB4BB29.4/1.5	29.4	1.5	6	47

Table 4.2 Bandpass filter specifications.

Time base circuitry

The system time base and gate generating circuitry shown in Figure 4.5-Figure 4.8 was used to create the control signals of the ACD. This circuitry was designed and built by Roy [43] and details of the circuit will not be included in the present discussion. The time base circuitry produced a clock signal that established the desired pulse repetition frequency for timing the T-R switch. A second gate was used for enabling the T-R switch. An additional pulse was created for triggering the oscilloscope and driving the mixer that produced the transmit RF tone burst. This gate was of variable size, allowing the outgoing pulse length to be changed. Finally, the last gate was used to drive the receive mixer for the backscattered signal. The delay of this gate could be varied to adjust the time of arrival of the scattered pulses. A diagram of how the system time base gates were arranged is given in Figure 4.9.

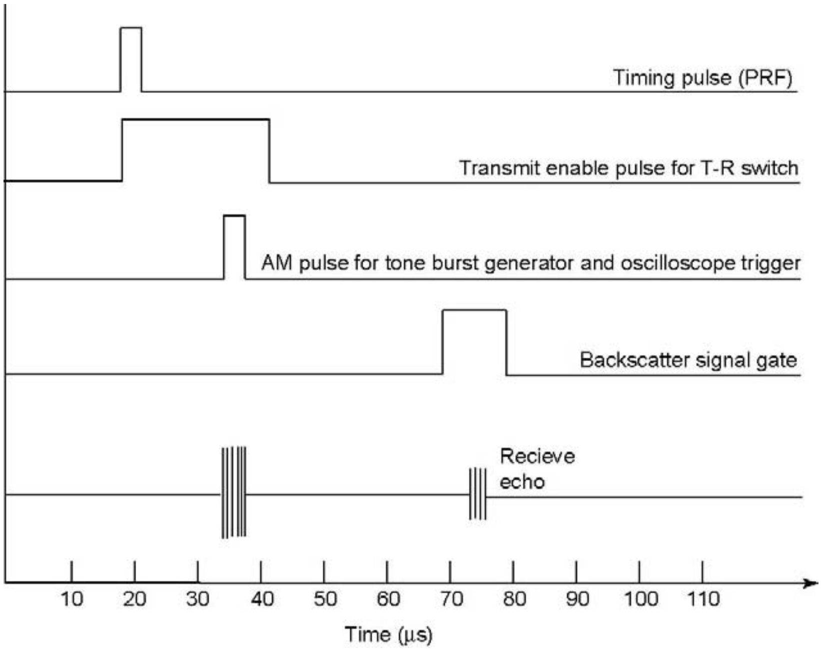

Figure 4.9 System time base used for controlling the ACD.

4.2 Experimental Methods

4.2.1 Preparation of red blood cell suspensions

In the present research all experiments using red blood cells suspensions were performed using fresh porcine blood obtained from Animal Biotech Industries Inc. (ABI). The blood was drawn from a live animal, mixed with sodium heparin anticoagulant, and kept in 1 liter bottles at 4-8° C both during and after shipping. Upon arrival, four 500 µl samples were pipetted out of the 1 liter blood bottle with a programmable micropipette (Eppendorf) and placed in four 75 mm length by 1.1 mm inner diameter plastic capillary tubes. The capillary tubes were then placed in a micro hematocrit centrifuge (Damon/IEC) for five minutes, causing sedimentation of the red blood cells. Following centrifugation, the tubes were placed in a hematocrit reader that allowed the correct hematocrit for the blood sample to be determined.

After the hematocrit value of each batch of blood was known, the suspensions were prepared. Depending on the final suspension hematocrit, the correct volume of whole blood had to be centrifuged. This volume, V_{in}, was calculated with the following formula

$$V_{in} = V_{sample} \frac{H_{final}}{H_{initial}} \tag{4.2}$$

where V_{sample} corresponds to 50 ml and was the final volume of the sample suspension placed in the sample holder, H_{final} was the desired final hematocrit, and $H_{initail}$ was the initial hematocrit measured for each batch of blood.

The volume of blood was then placed in a test tube and centrifuged using a refrigerated centrifuge (Mistral 2000) set to 4° C and 4500 rpm for 10 minutes. Centrifugation caused the red blood cells to sediment at the bottom of the test tube leaving the “buffy coat” of white cells and platelets and the plasma on top. A schematic of centrifuged blood is given in Figure 4.10.

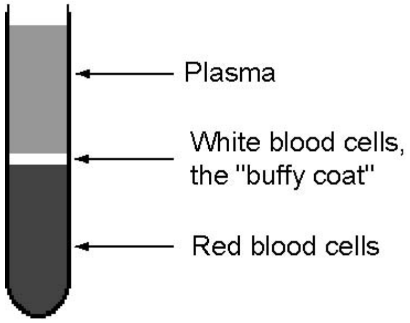

Figure 4.10 Schematic of the blood constituents after separation through centrifugation.

Following centrifugation, the buffy coat and plasma were carefully removed with a micropipette. Each sample was carefully mixed with an isotonic saline solution (0.9% NaCl) until the final desired sample volume (50 ml) was reached and a uniform color was achieved. Isotonic saline has the same osmotic pressure as plasma and can therefore be used to create suspensions of red blood cells without alteration. Following a thorough mixing, 500 µl from each sample was pipetted into a capillary tube and the exact final hematocrit of the suspension was measured. This was also done to double check that the no error was made when preparing the suspensions. All samples were then kept at a constant 4° C temperature using a constant temperature bath (Neslab RTE-210) whilst performing the experiments.

4.2.2 Measurement of the return from a strong cylindrical target

In order to measure the attenuation in suspensions of red blood cells with and without microbubbles and to determine the SNR for a cylindrical wire target in blood, the backscattered rms voltage from the cylindrical wire target was needed. This measurement was performed by inserting the fork target holder in the sample holder with either the 25 µm tungsten wire or the 35 µm fiberglass wire stretched and glued across it. Using the micropositioning stages, the target was placed at the focus of the sound field where the backscattered return was maximized. The return rms voltage was then measured for 100 individual single-shot waveforms, acquired and digitized using the oscilloscope sampling at 1 GHz, transferred to a PC via GPIB, and saved and displayed using MatLab. A typical trace of the return signal from an elastic cylinder is given in Figure 4.11. This trace corresponds to the backscattered echo from a cylindrical wire target and consists of sixty acoustic cycles, twenty of which are at steady state. All the voltage returns measured in the experiments presented herein accounted for only the twenty cycles at steady state, which were gated out by the oscilloscope, as can be seen from Figure 4.11. An average rms voltage was then computed from the 100 single-shot waveforms obtained.

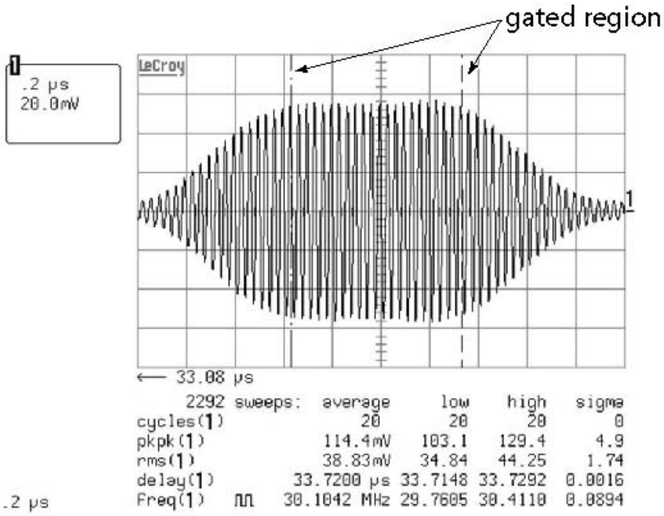

```
← 33.08 µs
      2292 sweeps:   average      low     high    sigma
cycles(1)                 20       20       20        0
pkpk(1)             114.4mV    103.1    129.4      4.9
rms(1)              38.83mV    34.84    44.25     1.74
delay(1)         33.7200 µs  33.7148  33.7292   0.0016
Freq(1)    ⎍⎍    30.1042 MHz 29.7605  30.4110   0.0894
```

Figure 4.11 Sample backscattered return waveform from a 35 µm cylindrical fiberglass wire target in a suspension of 13% hematocrit red blood cells at 30 MHz.

Assuming a normal distribution in the echo voltages, the precision uncertainty in the measurements was taken as the fluctuation from the mean rms voltage and defined as

$$\delta_{vrms} = t_{v,p} S_{\bar{x}} \, . \tag{4.3}$$

The term δ_{vrms} is the precision uncertainty in the rms voltage, $t_{v,p}$ is the student t-value for a given confidence interval, and $S_{\bar{x}}$ is the standard deviation of the mean defined as

$$S_{\bar{x}} = \frac{S_x}{\sqrt{N}} \, , \tag{4.4}$$

where S_x is the standard deviation of N measured voltage values, which in our case corresponded to 100. A histogram showing the rms echo voltage distribution of a typical set of measurements is given in Figure 4.12, illustrating that the distribution is approximately normal.

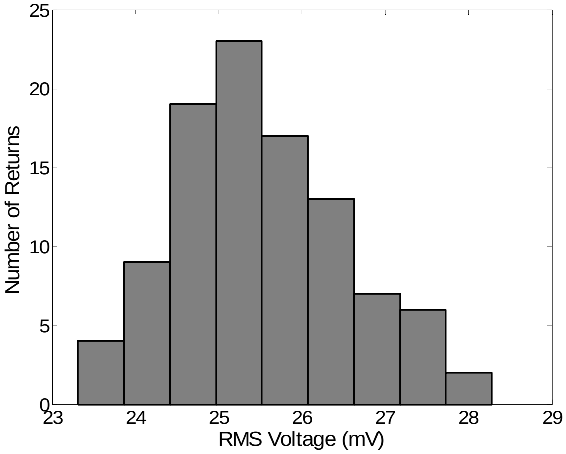

Figure 4.12 Histogram showing the distribution of the rms voltage data for a typical cylindrical target.

4.2.3 Measurement of the return from a suspension of particles

In order to experimentally determine the SNR for a strong cylindrical wire target in blood and for microbubbles in blood, a measure of the backscattered rms voltage return from suspensions of particles was needed. This measurement was performed by acquiring 100 single-shot waveforms from the insonified suspension, which were acquired and digitized using the oscilloscope sampling at 1 GHz, transferred to a PC via GPIB, and saved and displayed using MatLab. Since we were looking at collections of particles, the backscattered return did not have a definite shape as that from a single target seen in Figure 4.11. The acquired waveforms were therefore gated over the same time length as those acquired for the strong targets, illustrated in Sec. 4.2.2, and were kept consistent for each frequency and experiment. A sample trace of the scattering from a suspension of particles is given in Figure 4.13. An average rms voltage was then computed from the 100 single-shot waveforms obtained.

Similarly to the case of scattering from a cylindrical wire target in blood, the precision uncertainty in the measurements was taken as the fluctuation from the mean rms voltage and is given in Eq. (4.3). Figure 4.14 shows that the distribution in the echo voltages from suspensions of particles can also be assumed to be normal.

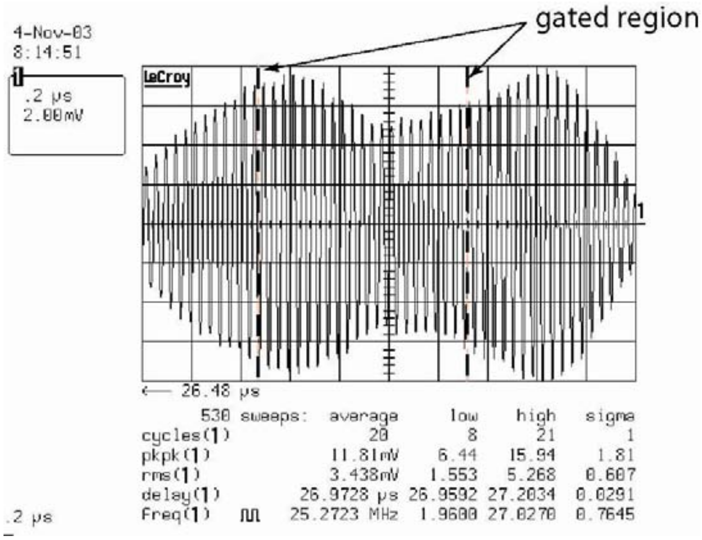

```
        530 sweeps:  average       low     high    sigma
cycles(1)                 20         8       21        1
pkpk(1)              11.81mV      6.44    15.94     1.81
rms(1)               3.438mV     1.553    5.268    0.607
delay(1)          26.9728 µs 26.9592 27.2034   0.0291
Freq(1)    ΠΠ   25.2723 MHz   1.9600 27.0270   0.7645
```

Figure 4.13 Sample oscilloscope trace showing the scattering from a suspension of red blood cells at 13% hematocrit with statistics at 25 MHz.

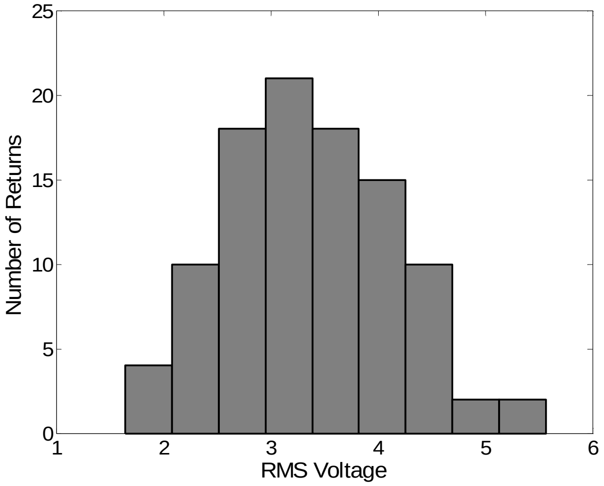

Figure 4.14 Histogram showing the distribution of the rms voltage data for the return from a suspension of red blood cells at 45% hematocrit.

4.2.4 Measurement of the round-trip time-of-flight and the transducer beam diameter

Measurements of the attenuation and SNR for the cylindrical wire target in blood required a precise measure of the distance traveled by the acoustic wave through the investigated medium and a measure of the beam diameter of each transducer respectively.

The distance traveled by the acoustic pulse was determined by measuring the round-trip time-of-flight (Δt) between the latex interface of the sample holder and the cylindrical wire target used for measuring attenuation. This measurement was performed by placing the cursors of the oscilloscope on the peak of the second cycle of the backscattered return from the latex interface and on the peak of the second cycle of the backscattered return from the cylindrical wire target. The difference between the two measured points yielded the round-trip time-of-flight. Figure 4.15 shows a sample oscilloscope trace used for performing the measurement of the Δt.

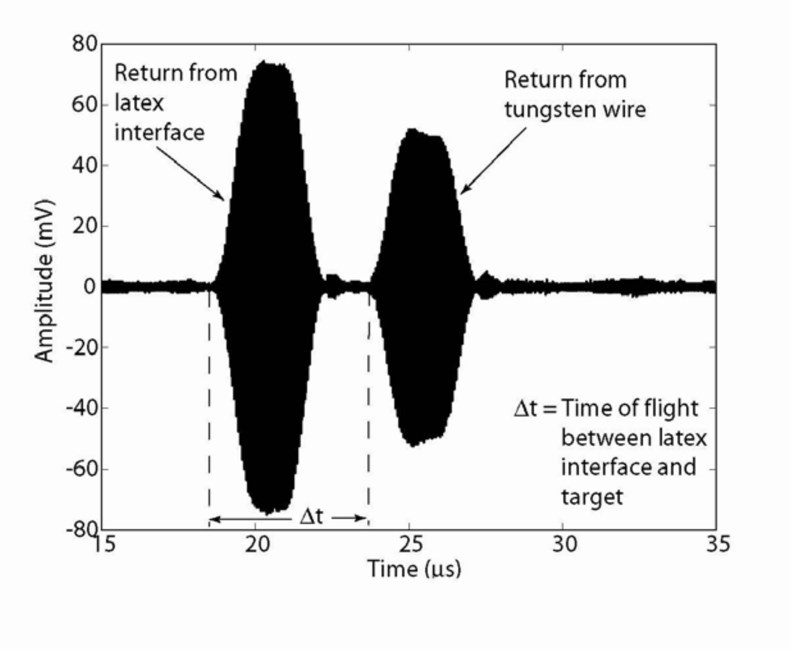

Figure 4.15 Sample oscilloscope trace of a single-shot 15 MHz waveform in isotonic saline seen during attenuation measurements. The first pulse corresponds to the return from the latex interface while the second is that from the tungsten wire cylindrical target.

Measurements of the -3 dB beam diameter for each transducer were performed experimentally by first placing the cylindrical wire target at the focus of the sound field and measuring the maximum return voltage and positioner settings. Using the micrometer stages, the target was subsequently moved away from the focus perpendicular to the sound field, until the signal reached a level that was -3 dB below the maximum level. The positioner settings were once more recorded and the procedure was repeated for the opposite side of the beam. The difference between the positioner settings then yielded the beam diameter. It is important to consider that the method just outlined for measuring the beam diameter is only valid if the target diameter is much less than the beam diameter of the transducer. For the current experiments, the diameters of the cylindrical wire targets used were either 25 µm or 35 µm which are much less than the beam diameter of all the transducers used (see Table 5.6). The uncertainty in the measured beam diameter was taken as one half the resolution of the micropositioning stages, corresponding to ±5 µm.

4.2.5 Measurement of the size distribution of *Optison*®

In order to apply the correct theoretical model for the SNR of *Optison*® microbubbles in blood, the size distribution of the microbubbles had to be known. A method was therefore devised for measuring the aforementioned distribution.

Prior and after the SNR of *Optison*® microbubbles in blood experiment, a sample of *Optison*® microbubbles was placed on a glass microscope slide and imaged using an 40x microscope (Olympus BX51). Approximately 150 images at different locations of the slide were recorded and saved.

After obtaining the bubble images, an image processing program (X-Cap, EPIX Inc.) was used to determine the radius of each individual bubble. This program used a routine called Blob

Analysis to count the number of pixels comprising the area of each bubble, from which a bubble radius could then be determined. A representative microscope image is given in Figure 4.16.

The procedure initially required calibration of the pixel size calibration by loading an image of a target of known dimensions taken with the same 40x microscope used for imaging the bubbles. This calibration was subsequently entered in the program which then executed a script that performed the following tasks[2]: (i) prompted the user to load an image file; (ii) used the Blob Analysis routine to count the number of pixels in each bubble (excluding bubbles touching the edge of the image); (iii) Saved the resulting data in an Microsoft Excel spreadsheet, which was appended for each new measurement. Following the image processing routine, the data was imported into Microsoft Excel, sorted in bins using the histogram routine and plotted.

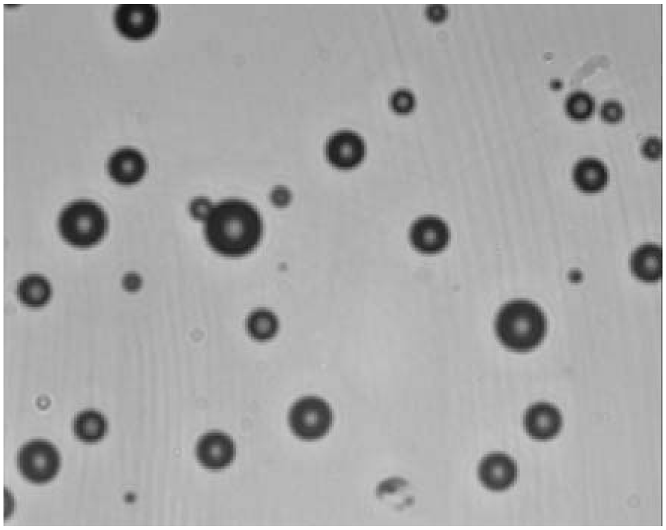

Figure 4.16 Sample image used for measuring the size distribution of *Optison®* microbubbles. The field of view of each image is 110 x 90 µm.

---

[2] The aforementioned script was written by Dr. Charles R. Thomas, whose help and experience made this experimental procedure possible.

4.3 Experimental Procedure

4.3.1 Attenuation through a suspension of red blood cells

The first experiment consisted of measuring the attenuation through a suspension of red blood cells at different hematocrits as a function of frequency. Six different hematocrits were chosen in the range of 3.5% to 50% to go from a scenario in which the scatterers are very far apart, to a scenario in which the scatterers are tightly packed. The physiological range of human males and females (35%-50% hematocrit [18]) was included to make the problem clinically relevant.

Initially, red blood cell suspensions were prepared using the technique described in Sec. 4.2.1. Four suspensions were prepared for each hematocrit for a total of 24 samples. Table 4.3 gives a detailed outline of all the suspensions prepared. The ultrasound apparatus was then set up to operate at the first desired frequency. A new, clean latex membrane was placed on the sample holder and tightly stretched. Fifty milliliters of isotonic saline were pipetted in the chamber and the fork target holder was inserted with a 25 μm tungsten wire stretched and glued across it. Using the micrometer stages, the tungsten wire was placed at the focus of the sound field and the positioner settings were recorded. The rms return voltages from the tungsten wire in pure saline were measured for 100 individual single-shot waveforms. The roundtrip time-of-flight between the latex interface and the tungsten wire was recorded, as well as the temperature of the water in the tank. The saline was then pipetted out of the chamber, disposed of and the first blood sample at the lowest hematocrit was pipetted in. The procedure was performed while ensuring that the target did not move out of the focus. The red blood cell suspension was then gently stirred to distribute the red cells evenly and the voltage returns and time-of-flight of the target were measured in the same way as with the saline measurement. The blood was then pipetted out, disposed of, and the return voltages and time-of-flight were measured for all other suspensions in increasing hematocrit order. See Figure 4.11 for a sample oscilloscope trace.

Nominal Hematocrit (%)	Sample Volume (ml)	Hematocrit Sample #1 (%)	Hematocrit Sample #2 (%)	Hematocrit Sample #3 (%)	Hematocrit Sample #4 (%)
3.5	50	3.8	3.7	3.2	4.0
12.5	50	12.5	12	12.5	12.5
20	50	19	20	20	20
30	50	29.5	29.5	30	30
40	50	40	40	40	40
50	50	50.5	47	50	50

Table 4.3 Red blood cell suspensions for attenuation experiment.

Once all the returns were measured for the red blood cell suspensions at all hematocrits, the tank was emptied, and the transducer and bandpass filter were changed for the next frequency measurements. At this point, the sample holder was detached, cleaned and rinsed with isotonic saline, and the latex membrane was replaced. The same procedure was repeated at the other frequencies considering a few important issues: (i) the voltage driving the transducer and the voltage return signals from the transducer had to be below the saturation limit of any of the electronic components in the circuit; (ii) the target had to be far enough away from the latex interface to distinguish both returns clearly and at the same time stay as close as possible to the interface to minimize the time of travel, preventing the return echoes from dropping below noise levels due to attenuation. The shorter time of travel was needed especially at the high hematocrits and high frequencies when the attenuation was more pronounced; (iii) the suspensions had to be well stirred before taking any data.

Finally, the attenuation coefficient was measured by comparing the rms voltage return $v_{rms}(TB)$ from a 25 μm diameter (cylindrical) wire target in a suspension of red blood cells at different hematocrits with the rms voltage return $v_{rms}(TS)$ in pure (0.9% NaCl) isotonic saline. The amplitude attenuation coefficient α introduced in Chapter 3 was therefore computed as

$$\alpha = \left[20 \log \frac{v_{rms}(TS)}{v_{rms}(TB)} \right] \Big/ L\,, \tag{4.5}$$

where L is the round-trip distance traveled by the sound wave from the latex interface to the target and back. In the following measurements, it was always assumed that the attenuation through water and isotonic saline was negligible compared to that of red blood cell suspensions [27, 74]. The distance L was calculated from the round-trip time-of-flight Δt (in saline) as

$$L = c\Delta t\,, \tag{4.6}$$

where c was the speed of sound at the appropriate temperature.

4.3.2 SNR of an elastic cylinder in a suspension of red blood cells

The SNR for an elastic cylinder in a suspension of red blood cells was determined for two different targets: a 30 μm diameter fiberglass wire and a 25 μm diameter tungsten wire. The experimental procedure was identical for both wires. Both experiments were performed with a suspension of 13% hematocrit red blood cells. A 13% hematocrit corresponds to the concentration that produces the largest scattering based on the theory presented in Sec. 3.1.1 as can be seen from Figure 3.1.

Four 50-ml suspensions of 13% hematocrit red blood cells were prepared as explained in Sec. 4.2.1. The ultrasound apparatus was set up to operate at the first desired frequency and the backscattered voltage returns from the target were measured in saline as previously explained for the attenuation experiment (Sec. 4.3.1).

The saline was then pipetted out and disposed of. The first suspension of red blood cells at 13% hematocrit was carefully inserted in the chamber and stirred. The voltage returns from the target in blood were measured for 100 individual single-shot waveforms and the data was recorded and saved as explained in Sec. 4.2.2. Next, the -3 dB beam diameter was measured by moving the 25 µm target away from the focus as given in Sec. 4.2.4. The target was then moved out of the focus, the red blood cell suspension was re-stirred, and the return voltages were measured from just the red blood cells as explained in Sec. 4.2.3. Subsequently, the tank was emptied out and the transducer and bandpass filter were changed for the next frequency measurement. At this point, the sample holder was detached, cleaned and rinsed with isotonic saline, and the latex membrane was replaced. The same experiment was then repeated at the other frequencies using the remaining three suspensions of red blood cells, one for each frequency, taking into consideration the same issues as described in Sec. 4.3.1.

In order to determine the SNR of a cylinder in a suspension of red blood cells, the rms voltage returns from the cylindrical target in blood were compared to the rms voltage returns from the scattering of red blood cells present in the absence of the target. The conceptual challenge in this case was to determine how to best compare the return from a single, discrete target, such as the elastic cylinder, to the return from a region containing multiple, distributed targets, such as red blood cells. The two measurements were related by normalizing each return by the volume of the insonified region. Thus, the returns from the cylindrical target were normalized by the insonified volume of the target and returns from the suspension of red blood cells were normalized by the volume of insonified red blood cells.

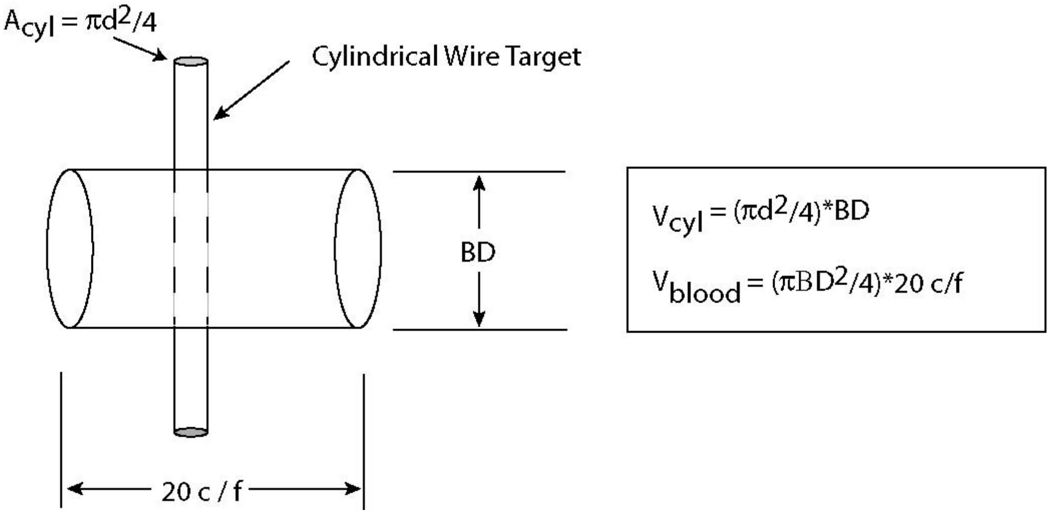

Figure 4.17 Schematic of the different insonified volumes of the cylindrical wire target and the suspension of red blood cells.

For the case of the cylindrical target, the insonified volume consisted of the cross-sectional area of the wire multiplied by a length corresponding to the -3dB beam diameter of each transducer. Figure 4.17 gives a schematic the insonified region of the cylindrical target V_{cyl} which can be computed as

$$V_{cyl} = \frac{\pi d^2}{4} BD, \tag{4.7}$$

where d is the diameter of the wire and BD is the -3 dB beam diameter of the specific transducer used.

The insonified volume for the suspension of red blood cells consisted of the cross-sectional area of the ultrasound beam times the length of the pulse used to investigate the medium. Assuming that the ultrasound beam is a cylinder of diameter BD, the investigated blood volume V_{blood} can be written as

$$V_{blood} = \frac{\pi BD^2}{4}\left(20\frac{c}{f}\right), \tag{4.8}$$

where c is the speed of sound at the desired hematocrit and f is the insonifying frequency. The SNR can therefore be determined experimentally with the following expression

$$SNR = 20\log\left(\frac{v_{rms}(TB)/V_{cyl}}{v_{rms}(B)/V_{blood}}\right), \tag{4.9}$$

where $v_{rms}(TB)$ is the rms backscattered voltage return of the cylindrical wire target in blood and $v_{rms}(B)$ is the rms voltage return of solely blood.

4.3.3 SNR and attenuation of *Optison*® microbubbles in a suspension of red blood cells

Experimental procedures for measuring the SNR and attenuation of *Optison*® microbubbles in a suspension of red blood cells were similar to those described in Sec. 4.3.1 and 4.3.2. The SNR was determined by measuring the voltage returns from blood and a mixture of blood and microbubbles. Similarly, the attenuation was determined by comparing the voltage returns from a 25 μm tungsten wire target in pure blood or in blood with microbubbles against the return for the wire in saline, accounting for the distance of travel, as given in Sec. 4.3.1. This experiment was performed at two different hematocrits, 1% and 45%, and two different concentrations of microbubbles, $6.5\text{x}10^4$ and $6.5\text{x}10^5$ microbubbles/ml. The two hematocrit values were chosen because their BSC is very similar (see Figure 3.1) but in one case (1%), the red blood cells are very sparse while in the other (45%), the red blood cells are closely packed. In addition, 45% hematocrit is the average physiological hematocrit for a human being. In the case of microbubble contrast agents, the lower concentration corresponds to the clinical dose while the higher one corresponds to the maximum allowed dose in any 10 min period [70]. Low and high hematocrits and bubble concentrations were used to see how the packing of red blood cells affected the response of the bubbles and vice-versa.

Optison® microbubbles were stored in 3 ml vials that always had to be kept at a temperature of 4-8° C. These vials were equipped with septa to ensure sealing. The clinical procedure for using *Optison*® consists of injecting 0.5 ml in the peripheral vein [70] which is distributed throughout the blood stream. Considering that there are approximately 5 l of blood circulating in an average human [18], one can determine the corresponding clinical dose for a sample volume of 50 ml of blood as

$$Clinical\ Dose = \frac{0.5ml\ dosage}{5000ml\ blood} 50ml\ sample = 5\mu l\ . \tag{4.10}$$

The clinical dose volume (5 μl) in 50 ml corresponds to a concentration of 0.1 μl/ml (6.5×10^4 microbubbles/ml) [70].

Prior to each experiment, a sample of *Optison*® microbubbles was imaged as described in Sec. 4.2.5 and eight suspensions of 1% hematocrit and 45% hematocrit were prepared as given in Sec. 4.2.1. After measuring the voltage returns from the 25 μm target in saline, the target was then moved out of the focus using the micrometer stages and the voltage returns from just saline were measured.

Next, five microliters of *Optison*® microbubbles were carefully drawn from the vile using a 10 μl syringe (Hamilton Gastight) without a venting needle and injected into the saline. The suspension was carefully stirred and the target was brought back to the focus, exactly at the same location where it was previously. The return voltages of the target in saline plus microbubbles were then measured and saved.

Subsequently, the saline was pipetted out of the sample holder and disposed of. The first suspension of 1% hematocrit red blood cells was carefully inserted in the chamber and stirred. The voltage returns from the target in blood were measured and the target was moved out of the focus to measure the return from just blood. Five microliters of *Optison*® microbubbles were then drawn from the vile and injected in the red cell suspension. The voltage returns were then measured for the blood with the microbubbles suspension. Next, the tungsten wire target was carefully moved back to the focus, making sure it was in the same exact location as for the measurements in saline. The suspension was remixed, and the return voltages were measured for the target in blood plus microbubbles. The 1% hematocrit suspension of red blood cells with the clinical dose of *Optison*® was pipetted out of the sample holder and disposed of. The same procedure was repeated for the 45% hematocrit suspension measurement.

Next, the tank was emptied out and the transducer and bandpass filter were changed for the next frequency measurement. At this point, the sample holder was detached, cleaned and rinsed with isotonic saline, and the latex membrane replaced. The same experiment was repeated for the other three remaining frequencies.

Once the experiment was finished for all four frequencies, it was repeated using the maximum allowable concentration (1 µl/ml or 6.5×10^5 microbubbles/ml) of *Optison*®. The only change in the experimental procedure was the way the *Optison*® microbubbles were drawn from the 3 ml vile. Since 50 µl is about 2% of the total volume of the *Optison*® left in the vile, it was important to replace the volume of *Optison*® drawn with an equal amount of air, to avoid a change in pressure within the vile that might damage the fragile microbubbles. Therefore a venting needle was used when drawing the 50 µl dose and was immediately removed once the microbubbles were drawn.

Finally, after the experiment was performed, a sample of the same *Optison*® microbubbles used for the experiment was placed on a microscope slide and imaged once again. About 150 images were taken using the same 40x microscope to observe whether the size distribution of the bubbles had changed while performing the experiment and if any of the bubbles were altered or damaged in the process. Having a good idea of the size distribution and the number density was crucial for modeling the scattering from *Optison*® in the manner described in Chapters 2 and 3.

The resulting experimental SNR was computed by comparing the rms voltage return of a suspension of red blood cells plus *Optison*® microbubbles $v_{rms}(BB)$ to that of pure red blood cells $v_{rms}(B)$

$$SNR = 20\log\left(\frac{v_{rms}(BB)}{v_{rms}(B)}\right). \tag{4.11}$$

In order to apply Eq. (4.11) the attenuation introduced by the addition of the microbubbles to the blood had to be accounted for. This was done by measuring the attenuation coefficient for suspensions of microbubbles in blood as explained in Sec. 4.3.1.

The amplitude attenuation coefficient for suspensions of 1% and 45% hematocrit red blood cells with and without *Optison*® microbubbles was therefore calculated using Eq. (4.5). The term $v_{rms}(TB)$, in this case, was either the rms voltage return from the cylindrical wire target in a suspension of pure red blood cells or in suspensions of red blood cells with the addition of *Optison*® microbubbles.

Chapter 5

Experimental Results and Analysis

This Chapter is dedicated to presenting the results of the experiments described in Chapter 4. The experimental results can be divided into two main categories: measurements of attenuation and signal-to-noise ratio (SNR). The amplitude attenuation coefficient will be displayed for suspensions of red blood cells as a function of frequency and hematocrit, with regression fits and regression parameters. Measurements of the attenuation coefficient will also be performed for suspensions of red blood cells with the addition of *Optison*® microbubbles at two different hematocrits (1% and 45%) as a function of frequency. Similarly, the SNR will be measured, initially for an elastic cylindrical wire target in a suspension of 13% hematocrit red blood cells, followed by a suspension of *Optison*® microbubble contrast agents at two concentrations (0.1 µl/ml and 1 µl/ml) in 1% and 45% hematocrit red blood cell suspensions. The lower microbubble concentration corresponds to the clinical dose or 6.5×10^4 microbubbles/ml while the maximum concentration corresponds to the maximum allowable dose or 6.5×10^5 microbubbles/ml. SNR results will be compared with different theoretical formulations presented in Chapters 2 and 3, accounting for the distribution of *Optison*®. This bubble size distribution will also be presented and discussed. Finally, a detailed uncertainty analysis will be performed for all the experimental results.

5.1 Attenuation Through Suspensions of Red Blood Cells

Figure 5.1 displays the amplitude attenuation coefficient α as a function of frequency in the 5-30 MHz range for six different hematocrit values, while Figure 5.2 displays the attenuation coefficient as a function of hematocrit in the 3.5-50% range for four different frequencies. Results are tabulated in Table 5.1. The dotted lines represent power law regression fits of the data with the equation for each fit and the correlation coefficient specified on the plot and summarized in Table 5.2 and Table 5.3.

Results from Figure 5.1 indicate an increasing attenuation coefficient with increasing frequency. As the hematocrit is increased, the attenuation increases but the frequency dependence exhibits a slight decrease, from $f^{1.6}$ for 3.5% hematocrit to $f^{1.1}$ for 50% hematocrit. Results published by previous researchers for different frequency ranges and different hematocrit levels exhibited linear-like behavior with fits ranging from f^{1} to $f^{1.2}$. A frequency dependence of $f^{1.2}$ for the attenuation coefficient was measured by Lockwood et Al. [53] in the 30-60 MHz range for a 38% hematocrit suspension and a similar result was obtained by Carstensen et al. [10] in an 85% hematocrit human blood residue in the 0.5–20 MHz range. However, results by Maruvada et al. [75] (30-60 MHz and 6-30% hematocrit) and Yuan and Shung [48] (3.5-12.5 MHz and 11-48% hematocrit) indicated a linear relationship of the attenuation coefficient with frequency. Experimental results given in Figure 5.1 suggest that a linear regression fit can successfully be used to fit the data in the physiological hematocrit range (30-50%) but this regression starts breaking down as the hematocrit level decreases.

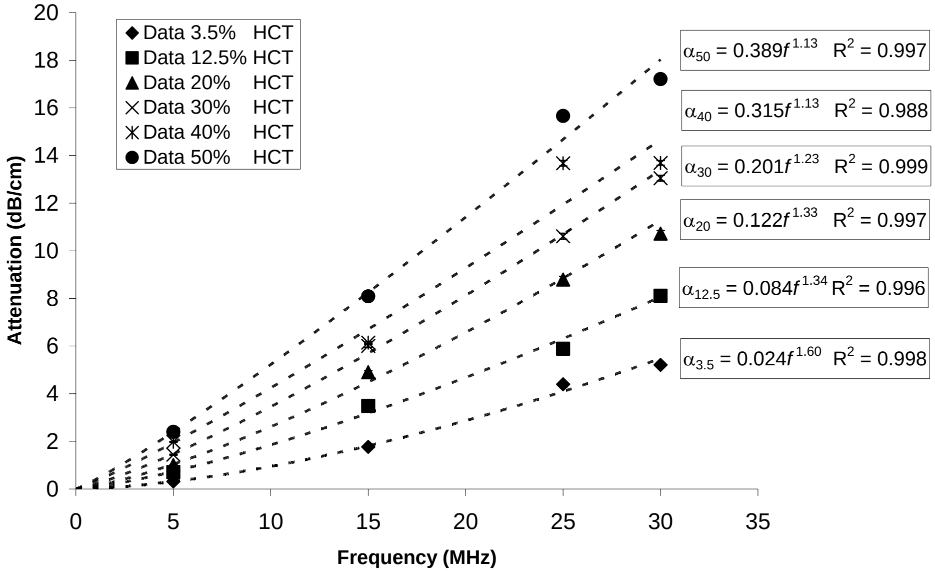

Figure 5.1 Attenuation coefficient as a function of frequency for 6 different hematocrit values with precision error bars (almost not visible). Dotted lines indicate power law regression fits with their respective equations displayed on the side.

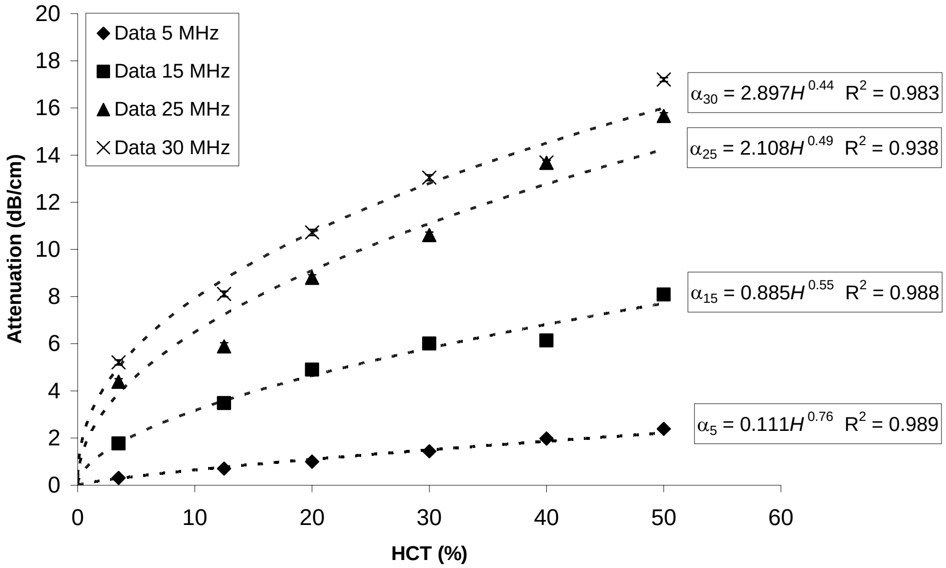

Figure 5.2 Attenuation coefficient as a function of hematocrit at four frequencies with precision error bars (almost not visible). Dotted lines indicate power law regression fits with their respective equations displayed on the side.

	3.5% HCT (dB/cm)	12.5% HCT (dB/cm)	20% HCT (dB/cm)	30% HCT (dB/cm)	40% HCT (dB/cm)	50% HCT (dB/cm)
5 MHz	0.31±0.01	0.71±0.01	1.00±0.02	1.44±0.02	1.98±0.02	2.39±0.01
15 MHz	1.77±0.04	3.48±0.05	4.90±0.06	6.01±0.06	6.14±0.03	8.09±0.03
25 MHz	4.39±0.12	5.88±0.16	8.79±0.13	10.61±0.12	13.68±0.12	15.66±0.14
30 MHz	5.21±0.11	8.11±0.12	10.72±0.13	13.05±0.12	13.69±0.10	17.20±0.08

Table 5.1 Results of the amplitude attenuation coefficient α as a function of frequency and hematocrit with the precision uncertainty. Uncertainties are computed in Sec. 5.1.1.

	3.5% HCT	12.5% HCT	20% HCT	30% HCT	40% HCT	50% HCT
a	0.024	0.084	0.122	0.201	0.315	0.389
b	1.60	1.34	1.33	1.23	1.13	1.13
R^2	0.998	0.996	0.997	0.999	0.988	0.997

Table 5.2 Values of the power law regression parameters for the attenuation coefficient (α in dB/cm) as a function of frequency (f) for different hematocrits (HCT) in the form $\alpha(f) = af^b$. R^2 is the correlation coefficient.

	5 (MHz)	15 (MHz)	25 (MHz)	30 (MHz)
a	0.111	0.885	2.108	2.897
b	0.76	0.55	0.49	0.44
R^2	0.989	0.988	0.938	0.983

Table 5.3 Values of the power law regression parameters for the attenuation coefficient (α in dB/cm) as a function of hematocrit (H) for different frequencies in the form $\alpha(H) = aH^b$. R^2 is the correlation coefficient.

The results given in Figure 5.2 display the hematocrit dependence of the attenuation at the four investigated frequencies. These results indicate an increase of the attenuation coefficient with increasing hematocrit. As frequency increases, the attenuation levels are higher but the hematocrit dependence becomes weaker, from $H^{0.76}$ at 5 MHz to $H^{0.44}$ at 30 MHz, where H is the hematocrit level of each blood sample. The present results deviate slightly from what was observed by Wang and Shung [65], who suggested a linear relationship between the attenuation coefficient and the hematocrit in the range 5-45% over the same frequency range. Additional measurements performed by Maruvada et al. [75] and Yuan and Shung [48] display a linear hematocrit dependence of the attenuation at higher (30-90 MHz) and lower (3.5-12.5 MHz) operating frequencies. The data in Figure 5.2 exhibits a nearly linear hematocrit dependence of the attenuation coefficient for the lowest frequency of 5 MHz while there is a clear departure from linear behavior as the frequency increases to 15, 25 and 30 MHz.

In summary, sound attenuation in a suspension of red blood cells was found to display a linear-like behavior with frequency at the higher hematocrits (30-50%) and a linear behavior with hematocrit at the lower frequencies (up to 5 MHz) but the general trend followed by the data points was determined to accurately match a power law behavior.

5.1.1 Uncertainty analysis

The precision error computed for the data tabulated in Table 5.1 corresponds to the precision uncertainty over the 100 measurement sample whose average constitutes each data point. This error was calculated using a standard procedure for the propagation of precision uncertainties given in Figliola and Beasley [69]. Assuming a normal distribution in the measured echo voltages (as can be seen from Figure 4.12), the attenuation coefficient α can be written as

$$\alpha = \alpha_{avg} \pm \delta_{\alpha}, \tag{5.1}$$

where α_{avg} is the average value over the 100-point sample and δ_α is the uncertainty given as

$$\delta_\alpha = \sqrt{\left(\frac{\partial\alpha}{v_{rms}\left(TS\right)}\right)^2 \delta v_{rms}\left(TS\right)^2 + \left(\frac{\partial\alpha}{v_{rms}\left(TB\right)}\right)^2 \delta v_{rms}\left(TB\right)^2} \ , \tag{5.2}$$

with partial derivatives given by

$$\frac{\partial\alpha}{v_{rms}\left(TS\right)} = \left(\frac{20}{v_{rms}\left(TS\right)L}\right)\frac{1}{\ln\left(10\right)} \tag{5.3}$$

$$\frac{\partial\alpha}{v_{rms}\left(TB\right)} = \left(\frac{-20}{v_{rms}\left(TB\right)L}\right)\frac{1}{\ln\left(10\right)} \ . \tag{5.4}$$

The terms δv_{rms}*(TS)* and δv_{rms}*(TB)* are the precision uncertainties (assumed to be statistically independent) of the rms backscattered voltage returns from the target in blood and just blood. These uncertainties are given as

$$\delta v_{rms}\left(TS\right) = t_{v,p}S_{\bar{x}}\left(TS\right) \qquad \delta v_{rms}\left(TB\right) = t_{v,p}S_{\bar{x}}\left(TB\right), \tag{5.5}$$

where $t_{v,p}$ is the student t-value for a given confidence interval and $S_{\bar{x}}$ *(TS)* and $S_{\bar{x}}$ *(TB)* are the standard deviation of the mean of the rms voltage returns from the target in blood and only blood defined as

$$S_{\bar{x}}\left(TB\right) = \frac{S_x(TS)}{\sqrt{N}} \qquad S_{\bar{x}}\left(B\right) = \frac{S_x(TB)}{\sqrt{N}} \ . \tag{5.6}$$

S_x *(TS)* and S_x*(TB)* are the standard deviations of the *N* measured voltage values that were taken for each round of measurements. One-hundred measurements were taken for each experiment and the confidence interval used was 95%, corresponding to a student t-value of 1.960. The precision errors were small, falling in the range between 0.01 and 0.16 dB/cm, and decreasing as the hematocrit increased. The results are summarized in Table 5.4.

	3.5% HCT δ_α (dB/cm)	12.5% HCT δ_α (dB/cm)	20% HCT δ_α (dB/cm)	30% HCT δ_α (dB/cm)	40% HCT δ_α (dB/cm)	50% HCT δ_α (dB/cm)
5 MHz	0.01	0.01	0.02	0.02	0.02	0.01
15 MHz	0.04	0.05	0.06	0.06	0.03	0.03
25 MHz	0.12	0.16	0.13	0.12	0.12	0.14
30 MHz	0.11	0.12	0.13	0.12	0.10	0.08

Table 5.4 Precision uncertainty in the attenuation coefficient for suspensions of red blood cells.

In addition to the precision error, bias uncertainties are introduced in the data. The most influential parameter whose uncertainty can lead to a significant change in the attenuation coefficient is the measure of the hematocrit. This error can be taken as half the resolution of the hematocrit reader (0.5% hematocrit) plus any additional error due to the lyzing (rupture) of red blood cells in the time frame of the experiment. Hematocrit readings of red blood cell suspensions prior to and after the experiments showed a maximum decrease in the hematocrit of 0.5%. Combining these two errors, the total error due to the hematocrit measurement can be quantified as $\sqrt{0.5^2 + 0.5^2} = \pm 0.71\%$ hematocrit. This error can therefore result in a change of the attenuation coefficient from ±0.1 dB/cm at 5 MHz to ±2.5 dB/cm at 30 MHz based on the power law data fits given in Table 5.3. The introduction of such an error can help explain the slight discrepancy between some of the data points in Figure 5.1 and Figure 5.2 and the regression fit. All errors associated with bias uncertainties introduced by the experimental apparatus and setup need not be considered since the attenuation is a ratio of rms voltages, causing these errors to cancel out.

Additional uncertainty in the hematocrit can be induced by red cell aggregation. This aggregation can occur either naturally or driven by a variety of phenomena associated with the presence of the acoustic field. Natural red cell aggregation can be neglected because it only occurs in the presence of proteins (fibrogen and globulin) found in plasma, which was removed for all experiments. Red cell aggregation due to the acoustic forcing is a little more complicated, however.

There are three basic forces associated with the propagation of a beam of sound through a suspension of particles. First, one has the transfer of momentum from the sound beam to the liquid due to absorption. The resulting acoustic streaming field [61] is manifested as a steady streaming flow that accelerates the host liquid through the focus. The Primary-Bjerknes (P-B) Force [40] is a direct radiation stress on the particle that is associated with scattering and points in the direction of sound propagation. Both the streaming and P-B forces serve to convect particles through the acoustic focus. This effect is readily observed in the laboratory, for as the particles traverse the acoustic focus, the echo arrival times also increase smoothly. Indeed, when viewed on an oscilloscope, the echo returns seem to march from left to right on the screen. Acoustic streaming and Primary-Bjerknes Forces are both second order phenomena that scale with the time-average acoustic intensity and depend on the attenuation of the medium (streaming) and the contrast of the particle (P-B forces).

There is a third type of acoustic force that deserves consideration. The Secondary-Bjerknes (S-B) Force [40] exists between particles undergoing volume pulsations. It is most commonly seen between bubbles and the sign of the force (attractive versus repulsive) depends on the distance between the particles and the relative phase of the motion of the two objects. This is also a second order effect that scales with time-average intensity, and the impact of S-B forces is less than P-B forces, all else being equal. Both of these forces will be *considerably* more pronounced in a suspension of bubbles than red blood cells owing the much greater contrast of the former over the latter.

Having said all this, we now point out that experimental observations of echo returns from a suspension of contrast agent exhibited no evidence of acoustic streaming; no echo returns were seen “moving” from left to right on the oscilloscope in a systematic fashion. From this we conclude that (i) the acoustic intensities were not sufficient to induce streaming in the liquid phase and (ii) the acoustic intensities were not sufficient to excite P-B forces in a suspension of bubbles. If P-B forces were not evident with bubbles, then we are confident that the same is also true for blood cells, for they are much weaker scatterers. Also, the lack of P-B forces also suggests that S-B forces can also be ignored.

In conclusion, the absence of any coagulating proteins, acoustic streaming, or radiation pressure forces lead us to believe that red blood cell aggregation is not a factor in our experiments. The suspensions are uniform and unaltered by the presence of the sound field. Indeed, the acoustic duty cycles employed in the experiments were intentionally kept low in order to ensure that this would be the case.

5.2 SNR of an Elastic Cylinder in a Suspension of Red Blood Cells

The signal-to-noise ratio was computed experimentally using Eq. (4.9) for both a 35 μm fiberglass wire in blood at 13% hematocrit and a 25 μm tungsten wire in blood at 13% hematocrit. This hematocrit value was chosen because it is the one that gives the highest backscattered return based on the theory by Twertsky [16, 33] and Shung [39]. SNR measurements were compared to the theoretical formulation given in Sec. 3.3.1. Results are shown in Figure 5.3 and Figure 5.4 and summarized in Table 5.5. Experimental measurements of the beam diameter were also performed and compared with those calculated using Eq. (4.1) and given in Table 5.5. These results are plotted in Figure 5.5.

	SNR Fiberglass Target (dB)	SNR Tungsten Target (dB)
5 MHz	93.0±0.4	116.7±0.6
15 MHz	81.9±0.5	104.2±0.7
25 MHz	67.6±0.9	88.6±0.8
30 MHz	65.7±0.5	78.3±0.7

Table 5.5 Results of the SNR for a fiberglass wire target and a tungsten wire target in a suspension of red blood cells at 13% hematocrit with precision uncertainties given in Sec. 5.2.1.

From the data points in Figure 5.3 and Figure 5.4, it can be seen that the increase in frequency has caused a reduction in SNR of almost 30 dB for the fiber glass wire and almost 40 dB for the tungsten wire. The theoretical formulation developed in Sec. 3.3.1 follows the same trend as the data points, with a tendency of underestimating the decrease in SNR at the higher frequencies, especially for the tungsten wire. This indicates that the contribution of the red blood cells to the overall scattering becomes more significant as the insonifying frequency increases. Discrepancies between theory and experiment could be attributed to a series of errors that can incur in the measurements. These errors will be discussed in Sec. 5.2.1 and can include the precision uncertainty in the rms voltage returns, the uncertainty in the target diameters, the uncertainty in the beam diameter, the uncertainty in the hematocrit, and the uncertainty in the speed of sound for the suspensions.

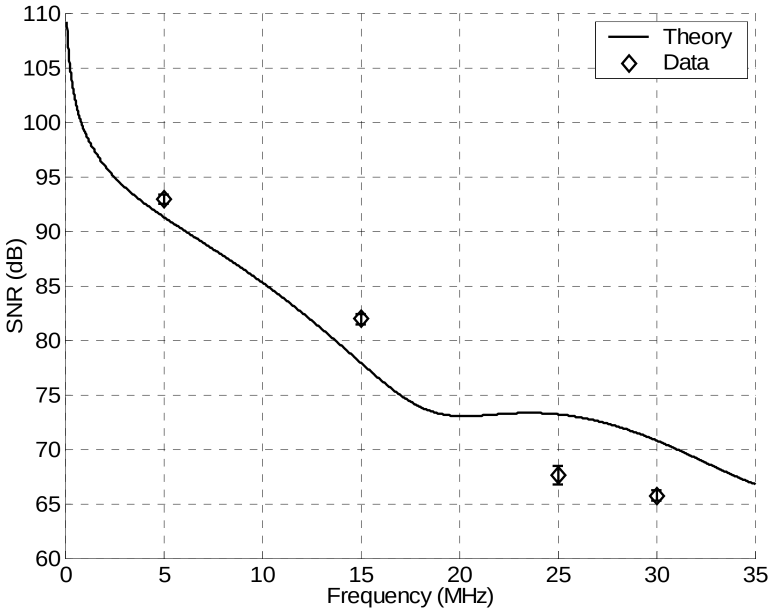

Figure 5.3 SNR for a 35 μm fiberglass cylindrical target in a suspension of 13% hematocrit red blood cells. Solid line indicates theoretical plot obtained from the formulation given in Sec. 3.3.1. Error bars indicate precision error for each specific measurement.

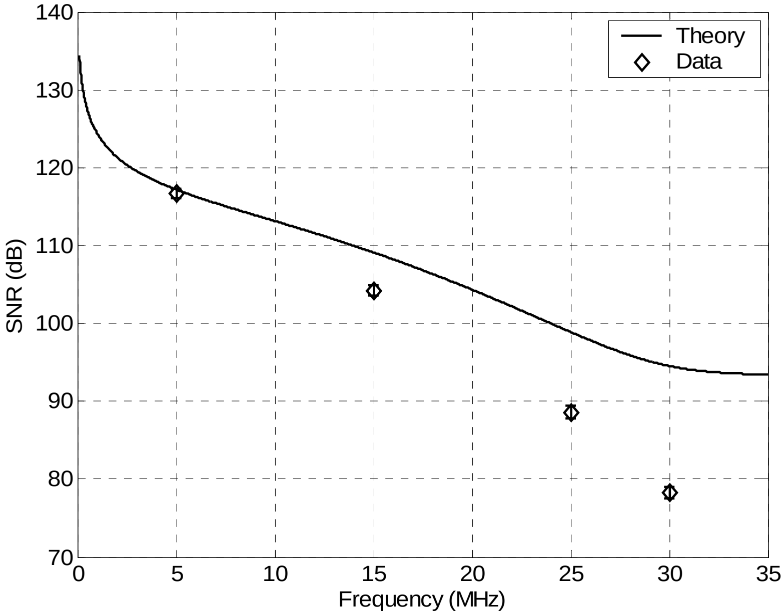

Figure 5.4 SNR for a 25 μm tungsten cylindrical target in a suspension of 13% hematocrit red blood cells. Solid line indicates theoretical plot obtained from the formulation given in Sec. 3.3.1. Error bars indicate precision error for each specific measurement.

Figure 5.5 gives a plot of the measured beam diameter of each transducer in blood and compares it to the beam diameter calculated using the theoretical formulation given in Eq. (4.1). The error of the measured diameters can be taken as 2.5 µm, half the resolution of the micrometer positioning stages and is given in Table 5.6. On the other hand, the error in the calculated beam diameter was computed by considering the uncertainties in the speed of sound of the suspension, element diameter and focal length. There seems to be a discrepancy between the calculated and measured beam diameter values, especially at the lower frequencies of 5 and 15 MHz. This small discrepancy was taken into account when determining the SNR for the fiberglass and tungsten targets but seemed to have a negligible effect on the final results. The results are tabulated in Table 5.6 with their corresponding calculated values.

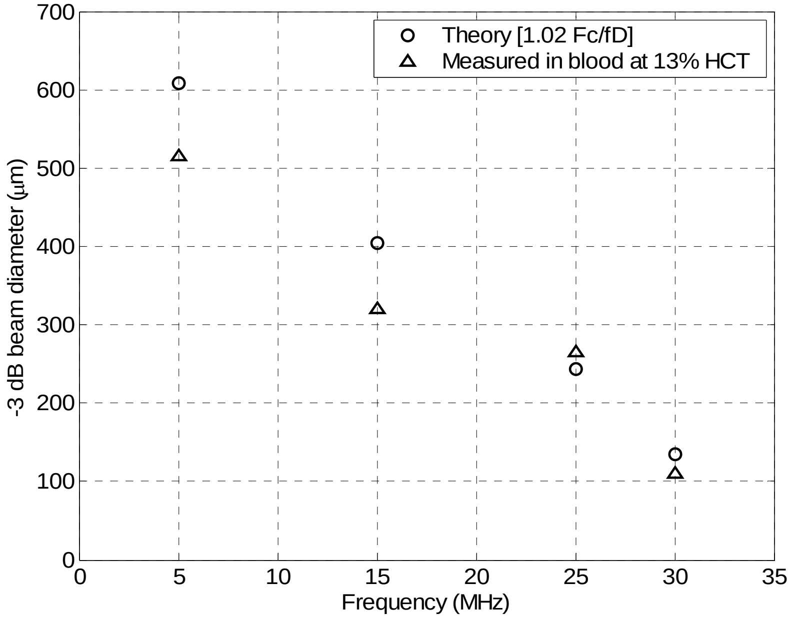

Figure 5.5 Comparison between the measured beam diameter in blood for each transducer and the beam diameter computed using Eq. (4.1). The error was found to be approximately 2.5 µm.

Frequency (MHz)	Calculated -3 dB beam diameter (μm)	Measured -3dB beam diameter (μm)
5	612±3.9	515±2.5
15	408±5.2	320±2.5
25	245±3.1	265±2.5
30	136±1.1	110±2.5

Table 5.6 Comparison between calculated and measured -3 dB beam diameters for the transducers with their respective uncertainties.

5.2.1 Uncertainty analysis

The error bars shown in Figure 5.3 and Figure 5.4 correspond to the precision error for each specific measurement. This error was calculated using the same technique as in Sec. 5.1.1 with the SNR defined as

$$SNR = SNR_{avg} \pm \delta_{SNR}\ , \tag{5.7}$$

where SNR_{avg} is the average SNR and δ_{SNR} is the precision uncertainty given as

$$\delta_{SNR} = \sqrt{\left(\frac{\partial SNR}{v_{rms}\left(TB\right)}\right)^2 \delta v_{rms}\left(TB\right)^2 + \left(\frac{\partial SNR}{v_{rms}\left(B\right)}\right)^2 \delta v_{rms}\left(B\right)^2}\ , \tag{5.8}$$

with partial derivatives given as

$$\frac{\partial SNR}{v_{rms}\left(TB\right)} = \left(\frac{20}{v_{rms}\left(TB\right)}\right)\frac{1}{\ln\left(10\right)} \tag{5.9}$$

$$\frac{\partial SNR}{v_{rms}\left(B\right)} = \left(\frac{-20}{v_{rms}\left(B\right)}\right)\frac{1}{\ln\left(10\right)}\ . \tag{5.10}$$

The terms $\delta v_{rms}(TB)$ and $\delta v_{rms}(B)$ are the precision uncertainties for the target in blood and pure blood defined as

$$\delta v_{rms}\left(TB\right)=t_{v,p}S_{\bar{x}}\left(TB\right) \qquad \delta v_{rms}\left(B\right)=t_{v,p}S_{\bar{x}}\left(B\right). \tag{5.11}$$

Precision errors range from ±0.4 dB to ±1.3 dB and are tabulated in Table 5.7. Two histograms of collected rms voltage returns for the fiberglass wire in blood and for just blood are given in Figure 4.12 and Figure 4.14.

	δ_{SNR} Fiberglass Target (dB)	% Error Fiberglass Target	δ_{SNR} Tungsten Target (dB)	% Error Tungsten Target
5 MHz	0.4	0.4	0.6	0.6
15 MHz	0.5	0.6	0.7	0.7
25 MHz	0.9	1.3	0.8	1.0
30 MHz	0.5	0.8	0.7	1.0

Table 5.7 Precision uncertainty in the measurements of the SNR of a fiberglass wire target and tungsten wire target in a suspension of 13% hematocrit red blood cells.

Additional errors that must be considered are the uncertainty in the sizing of the target, the uncertainty in the beam diameter, the uncertainty in the speed of sound of the suspension, and the uncertainty in the measured hematocrit level. The hematocrit uncertainty was found to be ±0.71%, as given in Sec. 5.1.1. The bias error associated with measuring the diameter of the wire target can be taken as half the resolution of the micro-calibration ruler used. This error can therefore be quantified as ±5 µm. Similarly, the uncertainty in the measurement of the beam diameter of the transducer can be taken as half the resolution of the micropositioning stages used as ±2.5 µm. Lastly, the error associated with the speed of sound was taken as ±1.7 m/s which corresponded to the maximum variation in our measurements. Assuming a worse case scenario situation, the maximum uncertainties in the SNR for both the fiberglass and tungsten wire targets can be obtained and are given in Table 5.8.

	Max Uncertainty in Fiberglass Target (dB)	Max Uncertainty in Tungsten Target (dB)
5 MHz	+ 2.6 - 2.3	+ 3.4 - 4.2
15 MHz	+ 2.7 - 2.2	+ 3.3 - 4.1
25 MHz	+ 2.6 - 2.2	+ 3.4 - 4.1
30 MHz	+ 2.6 - 2.1	+ 3.2 - 4.0

Table 5.8 Maximum uncertainties (both positive and negative) for the worse-case scenario for both a fiberglass cylindrical wire target in 13% hematocrit red blood cells and a tungsten wire target in 13% hematocrit red blood cells.

Figure 5.6 and Figure 5.7 show the effect of the maximum uncertainty in SNR for both the fiberglass and the tungsten wire targets. For the fiberglass wire case (Figure 5.6) the theoretical curves and error bars almost bracket the experimental data, except for the 30 MHz data point. On the other hand, in the case of the Tungsten wire (Figure 5.7), the theoretical solutions still do not match the data points beyond 25 MHz. It was found that the theoretical formulations were mostly affected by the small changes in estimated wire diameter. These changes cause a significant shift in the location of the elastic resonances predicted by the theoretical model, and also affect the experimental results, since those depend on the insonifyied wire volume, as shown in Figure 5.6 and Figure 5.7. Conversely, the errors in hematocrit, beam diameter, and sound speed were found to cause a minimal influence in the uncertainty of our measurements.

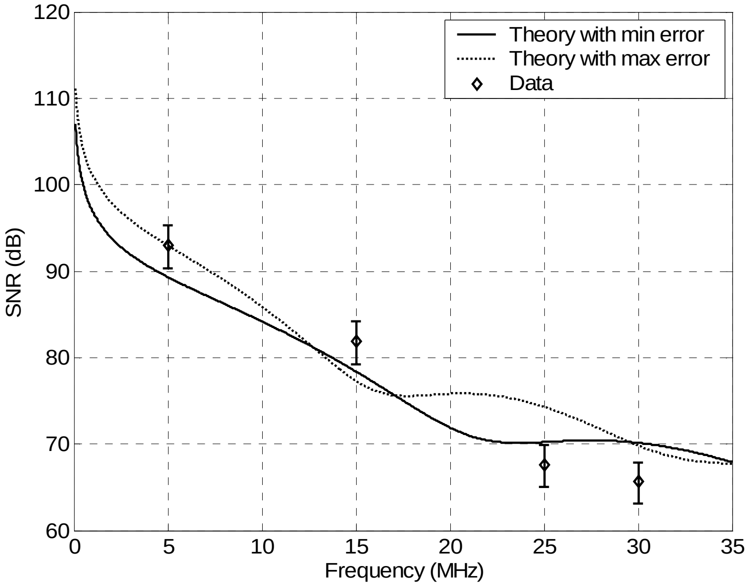

Figure 5.6 SNR for a 35 μm diameter fiberglass cylindrical wire target in a suspension of 13% hematocrit red blood cells showing the maximum and minimum theoretical curves and assuming a worse-case scenario uncertainty. Error bars also indicate the maximum achievable uncertainty in the measurements.

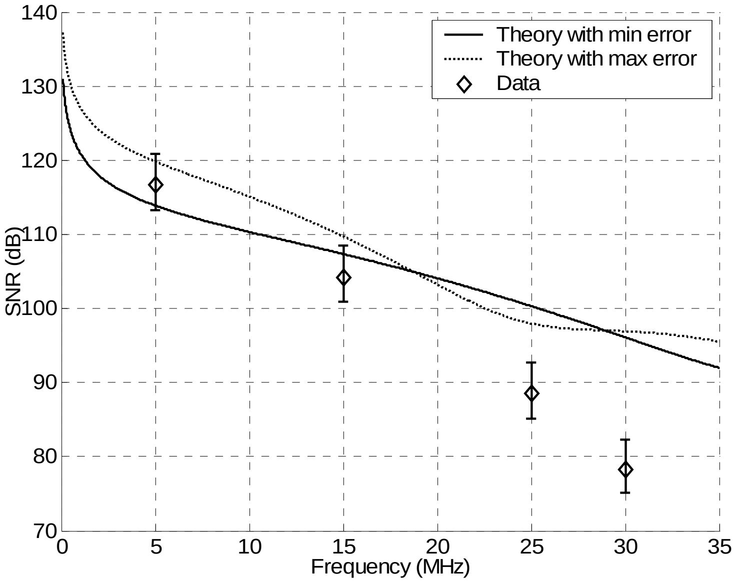

Figure 5.7 SNR for a 25 μm diameter tungsten cylindrical wire target in a suspension of 13% hematocrit red blood cells showing the maximum and minimum theoretical curves and assuming a worse-case scenario uncertainty. Error bars also indicate the maximum achievable uncertainty in the measurements.

5.3 Size Distribution of *Optison*® Microbubbles

In order to apply the correct theoretical model to the SNR data for the backscatter of *Optison*® microbubbles in blood, a measure of the size distribution was needed before and after the SNR experiment was performed. Any observable changes in the size and concentration of the microbubbles within the time-period of the SNR experiment could then be accounted for and corrected. The method for obtaining this size distribution was explained in Sec. 4.2.5 and plots of the size distributions are given in Figure 5.9 and Figure 5.10.

From Figure 5.9 one can observe that, in the initial pre-experimental concentration of *Optison*® microbubbles, the mean radius is around 1 µm and ranges from 0.2-2 µm with a maximum of 9 µm. This result agrees with the measure provided by Mallinckrodt Inc., the manufacturer of *Optison*®, which specifies a mean radius of 1-2.25 µm [70]. Similar results were also obtained by Ostensen et al. [76], who measured two batches of *Optison*® using a coulter counter, obtaining size distributions of 0.25-2 µm radius with peaks at 1.1 µm and 1.5 µm respectively (see Figure 3.6).

The size distribution given in Figure 5.10 also displays results that are in agreement with what was measured by previous authors and within the limits stated by the manufacturing company, with a mean radius ranging from 0.2-3 µm and a maximum radius of 7.7 µm. On the other hand, if compared to Figure 5.9, it is clear that the distribution has gotten broader with time, and the mean radius has shifted slightly to the right. The tendency of microbubbles to get larger over time can be attributed to the introduction of air in the vial when it is first opened, and every time *Optison*® is drawn out of the vial. The vial initially contains octofluoropropane (C_3F_8), which is also the gas encapsulated within the microbubbles. As the amount of air in the vial increases, so does the air concentration dissolved in the liquid containing the mircrobubbles, imposing a gas concentration gradient across the microbubble shell. Because C_3F_8 has very low solubility in the surrounding fluid, it cannot exit the microbubbles to equilibrate the gas concentrations inside and outside the contrast agent. Air therefore diffuses into the microbubbles across the penetrable albumin shells, leading to an increase in bubble size.

The images depicted by the letters a, b, and c, in Figure 5.8 showing the size-distribution of *Optison*® microbubbles before the experiment are much darker in color than those depicted by the letters d, e, and f, showing the size distribution after the experiment. The difference in the darkness of the microbubbles is caused by the change in the gas that they contain, from near-pure C_3F_8 to C_3F_8 plus air, causing a different refraction of the incident light from the microscope. Both distributions depicted in Figure 5.8 show a visible size variation, with the occasional anomalously large bubble. It is interesting to observe from the post-experimental images the presence of the albumin shell surrounding the microbubbles.

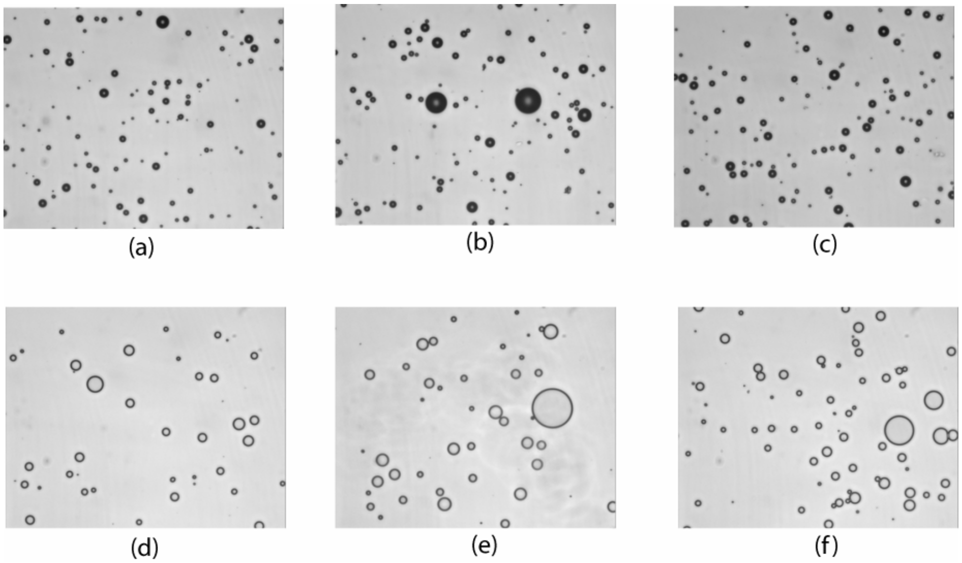

Figure 5.8 Sample images of *Optison*® microbubbles taken with a 40x microscope before the SNR experiment was performed (a, b, c) and after the SNR experiment was performed (d, e, f). The field of view of each image is 110 x 90 μm.

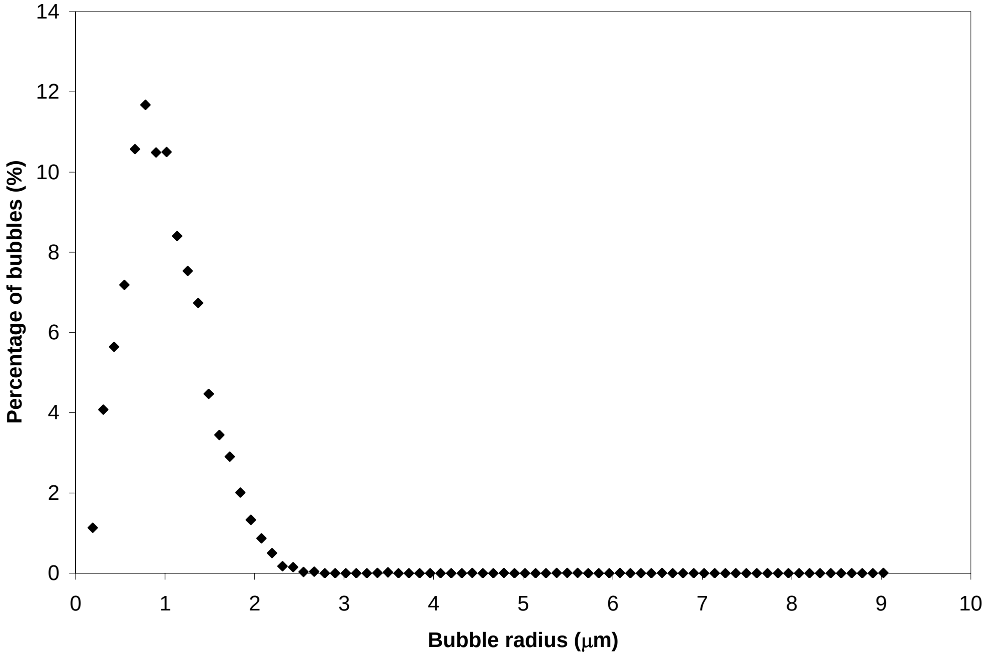

Figure 5.9 Size distribution of *Optison*® microbubbles before the SNR experiment was performed. Measurement based on approximately 9000 individual bubbles.

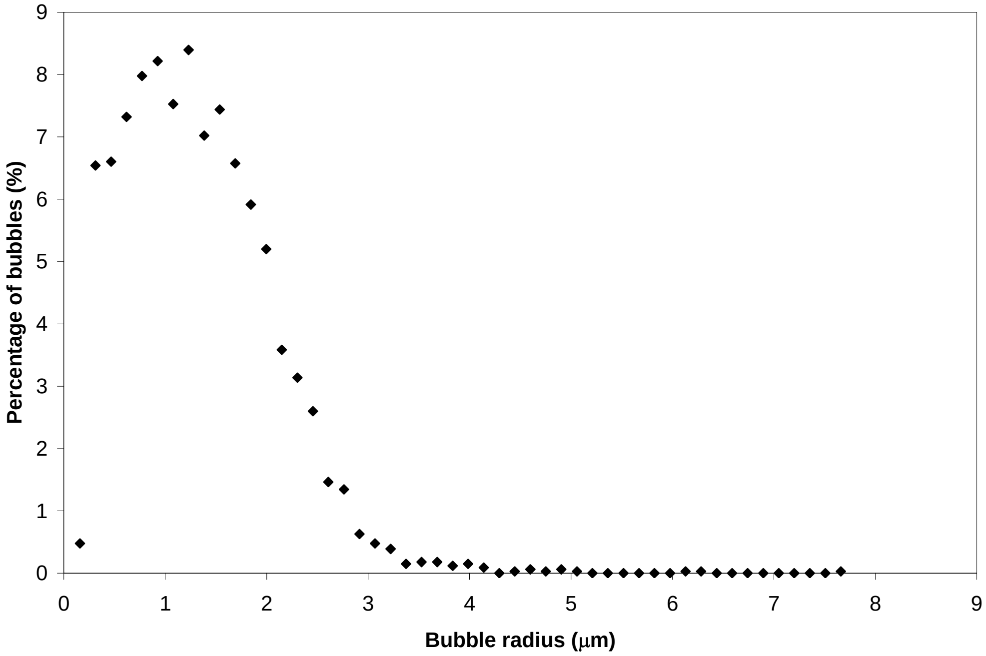

Figure 5.10 Size distribution of *Optison*® microbubbles after the SNR experiment was performed. Measurement based on approximately 3300 individual bubbles.

5.3.1 Uncertainty analysis

A detailed uncertainty analysis for using the image processing software X-Cap was performed by Thomas [77], the main results of which will be outlined in the present section. The Blob Analysis routine performed by X-Cap and introduced in Sec. 4.2.5 measured the number of pixels forming each bubble. Using the calibration settings from a known 50 μm ruler target, the program was able to determine the size of each pixel, found to be 0.19 μm in the vertical direction and 0.15 μm in the horizontal direction, and give a resulting bubble area in micrometers. From the given bubble area, the radius of each bubble was calculated as

$$a = \sqrt{\frac{A_b}{\pi}}\,, \tag{5.12}$$

where a is the radius of the bubble and A_b is the area provided by the X-Cap software. The error associated with the radius δ_R can therefore be written as [69]

$$\delta_R = \frac{\partial a}{\partial A_b}\delta_A = \frac{1}{2}\left(\frac{A_b}{\pi}\right)^{-\frac{1}{2}}\delta_A\,, \tag{5.13}$$

where δ_A is the error associated with the measurement of the area A_b. Assuming that the area of each bubble image can be expressed as

$$A_b = p_N\, p_H\, p_V\,, \tag{5.14}$$

where p_N is the number of pixels in the bubble image, p_H is the horizontal length (0.15 μm), and p_V the vertical length (0.19 μm), the error in the area δ_A can be expressed as [77]

$$\delta_A = \left[\left(p_v\, p_H\, \delta_{PN}\right)^2 + \left(p_H\, p_N\, \delta_{PV}\right)^2 + \left(p_v\, p_N\, \delta_{PH}\right)^2\right]^{\frac{1}{2}} \tag{5.15}$$

with δ_{PN}, δ_{PV}, δ_{PH} being the errors associated with p_N, p_V, and p_H. The errors δ_{PV} and δ_{PH} were found to be 0.007 μm and 0.006 μm respectively, assuming an uncertainty of 2 μm when determining the length of the calibration target and an uncertainty of 1 pixel when determining the number of pixels corresponding to that target length, in both the vertical and horizontal directions [77]. The error in the number of pixels δ_{PN} was determined by the way the X-Cap software counts pixels. When the Blob Analysis is performed, the program requires the user to enter a threshold intensity level in order to separate the bubbles from the rest of the background. Pixels below this threshold level are recognized by the program as part of the bubble and pixels above this level are considered background noise. Based on measurements made by Thomas [77], this error can be set to approximately δ_{PN} =8 pixels. The results above can then be inserted in Eq. (5.15) to determine the error in the area of the bubble, which can then be used in conjunction with Eq. (5.13) to determine the uncertainty in the radius measurement. Table 5.9 summarizes this computed error for a range of bubble sizes.

As one can observe, the error is very large for the smaller bubbles and becomes smaller as the bubble size gets larger and the number of pixels increases. Bubbles on the order of 1 μm to 1.5 μm, which were present in the largest numbers according to the distributions in Figure 5.9 and Figure 5.10, have an error that ranges from 8% to 12% of their radius.

Radius (μm)	Area (pixels)	Area (μm)	δ_A (μm)	δ_R (μm)	δ_R (%)
0.2	4	0.14	0.22	0.59	290
0.5	29	0.8	0.22	0.22	44
1.0	116	3.2	0.26	0.12	12
1.5	257	7.1	0.35	0.12	8
2.0	460	12.7	0.52	0.13	6.5
3.0	1039	28.6	1.1	0.18	6.1

Table 5.9 Calculated precision error for different bubble sizes using Eq. (5.13) and (5.15).

Additional systematic bias errors caused by the experimental setup were ignored when determining the size distribution of the *Optison*® microbubbles. These errors include an increase in the bubble radius due to the force exerted by the cover slip of the microscope slide on the microbubbles and slight variations in the light intensity of the imaging system used from one measurement to the next.

5.4 Attenuation Through *Optison*® and Red Blood Cells

An important part of the present investigation is a measure of the attenuation of blood with the addition of microbubbles. This assessment will allow us to quantify the extent to which microbubbles affect the attenuation in blood and will allow us to correct for this effect when computing the SNR of microbubbles in blood. It was therefore decided to measure the attenuation of the clinical dose (0.1 µl/ml or 6.5×10^4 microbubbles/ml) and the maximum dose (1 µl/ml or 6.5×10^5 microbubbles/ml) of *Optison*® microbubbles in the same suspensions of 1% and 45% hematocrit red blood cells also used for the SNR measurements.

Figure 5.11 illustrates the attenuation coefficient for 0.1 µl/ml of *Optison*® in a suspension of 1% and 45% red blood cells and results are given in Table 5.10. Almost no attenuation is present at 1% hematocrit, while at 45% the increase of the attenuation coefficient with frequency follows the same trend as that of pure blood, given in Sec. 5.1. The *Optison*® contrast agent does not significantly contribute to the attenuation both at the low and the high hematocrit as the data points of the attenuation of the red cell suspension almost exactly match those for blood plus the microbubbles. Only at 30 MHz is there a 1 dB/cm difference between the attenuation value with and without the clinical dose of *Optison*®.

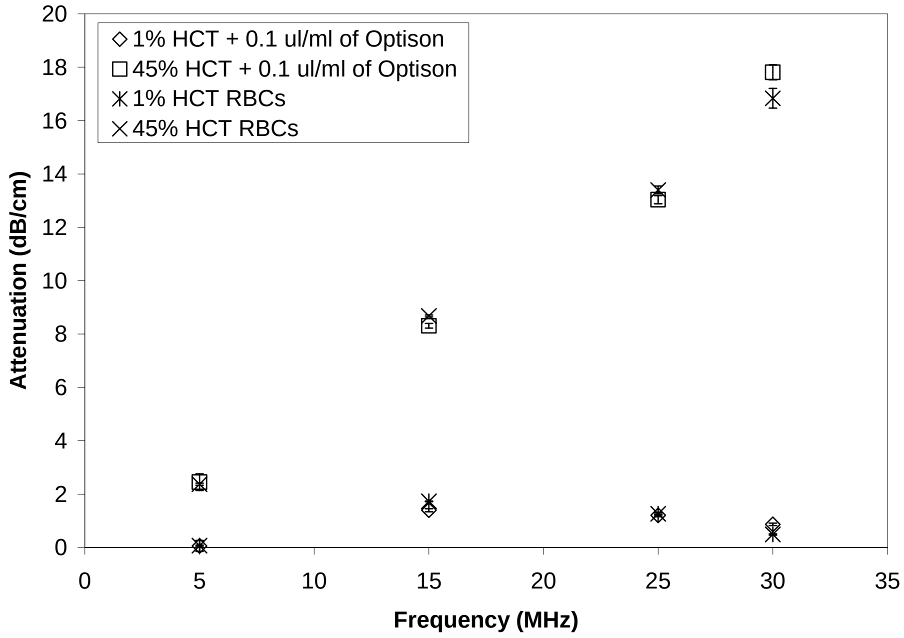

Figure 5.11 Attenuation coefficient as a function of frequency for suspensions of 1% hematocrit and 45% hematocrit red blood cells and the clinical dose (0.1 µl/ml or 6.5x10^4 microbubbles/ml) of *Optison*® compared to pure red blood cells at the same hematocrit values. Error bars indicate precision error.

When the concentration of *Optison*® is increased by a factor of 10, as can be seen from Figure 5.12, Figure 5.13 and from Table 5.11, the microbubbles have a greater effect on the attenuation of the signal. From Figure 5.12 it can be observed that the 15, 25, and 30 MHz data points for the 1% hematocrit blood with the addition of *Optison*® are offset by 1.8-3.3 dB/cm compared to those of pure red blood cells. In addition, at 5 MHz, one can observe a large jump of approximately 16 dB/cm in the attenuation for the suspension with *Optison*®. This jump can be explained by the fact that many of the microbubbles are of resonance size at around 5 MHz (see Sec. 5.3), as predicted by Figure 2.15 for contrast agent microbubbles in the 1-1.5 µm radius range. At resonance, the scattering cross-section of the microbubbles significantly increases, causing additional attenuation to occur due to the additional scattering and the increased absorption cross-section. It is therefore important to consider and account for this increase in the attenuation when computing the SNR in Sec. 5.5.

	1% HCT (dB/cm)	1% HCT + 0.1 µl/ml *Optison®* (dB/cm)	45% HCT (dB/cm)	45% HCT + 0.1 µl/ml *Optison®* (dB/cm)
5 MHz	0.07±0.02	0.06±0.21	2.38±0.04	2.45±0.31
15 MHz	1.73±0.01	1.40±0.06	8.68±0.03	8.31±0.09
25 MHz	1.27±0.05	1.21±0.05	13.40±0.15	13.04±0.15
30 MHz	0.49±0.02	0.87±0.04	16.84±0.37	17.81±0.28

Table 5.10 Data for the amplitude attenuation coefficient for suspensions of 1% hematocrit and 45% hematocrit red blood cells with and without the clinical dose (0.1 µl/ml or 6.5x10^4 microbubbles/ml) of *Optison®*. Uncertainties indicate the precision error and will be explained in Sec. 5.4.1.

	1% HCT (dB/cm)	1% HCT + 1 µl/ml *Optison®* (dB/cm)	45% HCT (dB/cm)	45% HCT + 1 µl/ml *Optison®* (dB/cm)
5 MHz	0.23±0.01	16.88±0.47	4.87±0.27	22.35±0.15
15 MHz	0.73±0.01	4.04±0.15	7.73±0.04	8.74±0.15
25 MHz	2.68±0.04	5.09±0.19	15.42±0.25	15.79±0.20
30 MHz	2.22±0.02	4.01±0.07	17.63±0.26	18.49±0.33

Table 5.11 Data for the amplitude attenuation coefficient for suspensions of 1% hematocrit and 45% hematocrit red blood cells with and without the maximum dose (1 µl/ml or 6.5x10^5 microbubbles/ml) of *Optison®*. Uncertainties indicate the precision error and will be explained in Sec. 5.4.1.

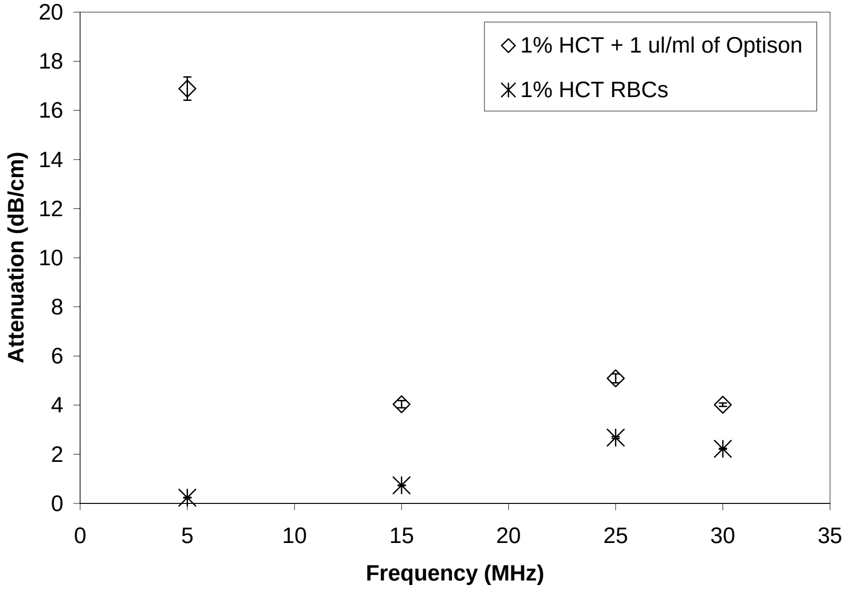

Figure 5.12 Attenuation coefficient as a function of frequency for a suspension of 1% hematocrit red blood cells and the maximum dose (1 µl/ml or 6.5x10^5 microbubbles/ml) of *Optison*® compared to that of only red blood cells at the same hematocrit. Error bars indicate the precision error.

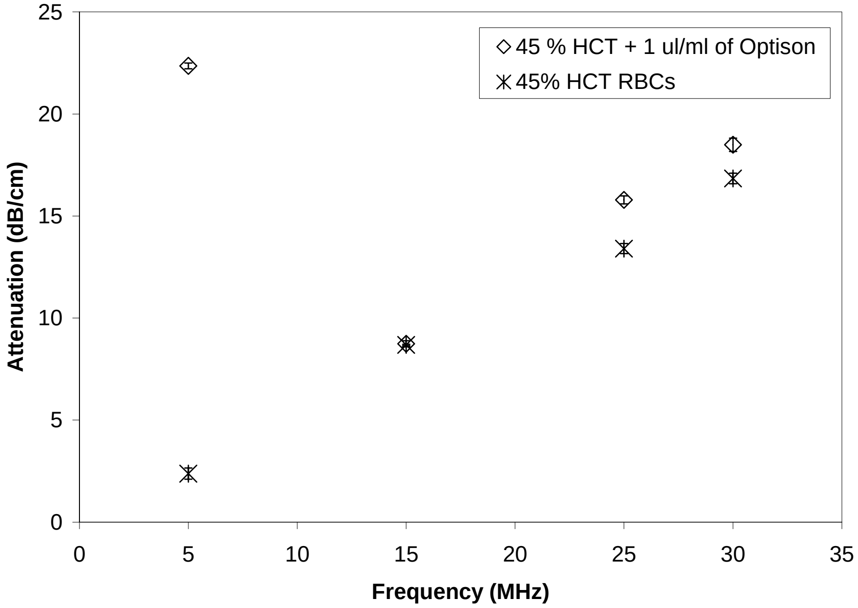

Figure 5.13 Attenuation coefficient as a function of frequency for a suspension of 45% hematocrit red blood cells and the maximum dose (1 µl/ml or 6.5x10^5 microbubbles/ml) of *Optison*® compared to that of only red blood cells at the same hematocrit. Error bars indicate the precision error.

Similarly to the case of a suspension of 1% hematocrit red blood cells with 1 µl/ml of *Optison*®, the results for the 45% hematocrit measurement given in Figure 5.13 show a slight offset between the curves with and without bubbles. Apart from the 5 MHz point, the offset is slightly smaller than that for the 1% case (1 dB/cm at 15 MHz, 0.4 dB/cm at 25 MHz, and 0.9 dB/cm at 30 MHz). This is probably due to the fact that the tighter packing of the red blood cells inhibits the response of the bubbles, decreasing their ability to scatter sound and therefore causing a smaller change in the attenuation coefficient compared to the 1% hematocrit case. Figure 5.13 also shows a large increase in the attenuation at 5 MHz (17.5 dB/cm) and the reason for this high value is the same as that for the 1% case, resonance of the microbubbles.

The attenuation of 0.1 µl/ml and 1 µl/ml of *Optison*® in just saline were also measured, with results shown in Figure 5.14. It can be seen from the plot that the clinical dose (0.1 µl/ml) of *Optison*® has negligible attenuation, while the maximum dose (1 µl/ml) of *Optison*® causes considerable attenuation. Again, the 5 MHz point is much higher than the rest while for higher frequencies, 1µl/ml of *Optison*® seems to introduce about 2-3 dB/cm of attenuation.

Based on these results, it can be concluded that the addition of 0.1 µl/ml of *Optison*® does not contribute significantly to the total attenuation when mixed with blood. On the other hand, 1 µl/ml of *Optison*® has a strong impact on the total suspension attenuation especially at the low hematocrit concentration and at 5 MHz, the resonance frequency of many of the contrast agent microbubbles.

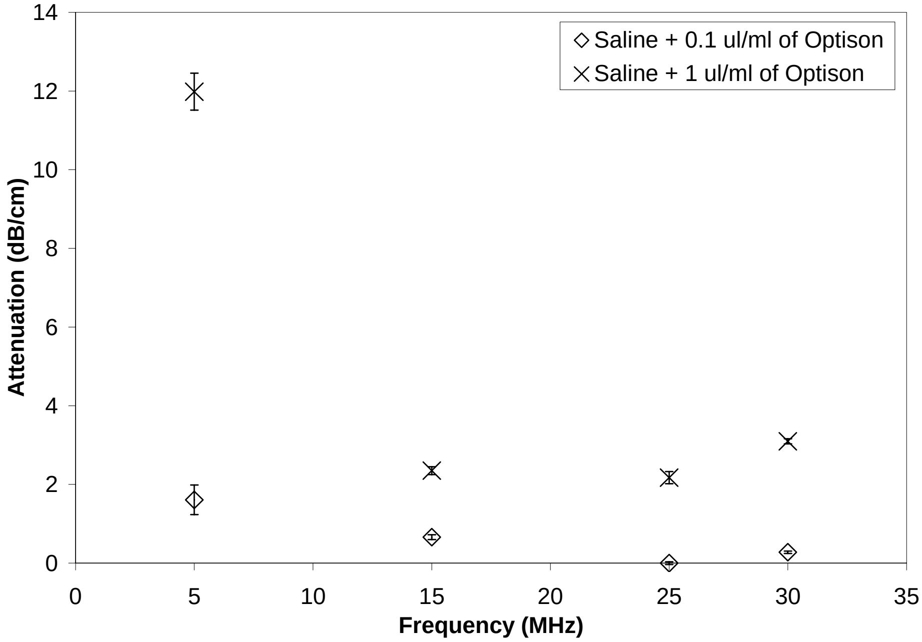

Figure 5.14 Attenuation coefficient as a function of frequency for a the clinical dose (0.1 µl/ml or $6.5x10^4$ microbubbles/ml) and the maximum dose (1 µl/ml or $6.5x10^5$ microbubbles/ml) of *Optison*® microbubbles in isotonic (0.9% NaCl) saline. Error bars indicate the precision error.

5.4.1 Uncertainty analysis

The precision error for the attenuation of blood and saline with the addition of *Optison*® microbubbles was computed using Eq. (5.2) in the same way as in Sec. 5.1.1 and results are summarized in Table 5.12 and Table 5.13.

The precision error results indicate a 1-13% precision uncertainty in the 0.1 µl/ml of *Optison*® attenuation measurements and a 1-7% precision uncertainty in the 1 µl/ml of *Optison*® measurements. The only anomalous point with a larger error was the 5 MHz point with the 1% hematocrit suspension and 0.1 µl/ml of *Optison*®, which displayed an error of 200%. Similar results were also obtained for the precision error for 0.1 µl/ml and 1 µl/ml of *Optison*® in saline which ranged from 1-5%. Precision error can therefore be considered negligible and was not found to be the major source of error in the present measurements.

Additional forms of error are the uncertainty in the measurement of the hematocrit and those in microbubble number density and microbubble size distribution. As explained in Sec. 5.1.1, the hematocrit uncertainty is about 0.71% and leads to a maximum variation in the attenuation coefficient of ±0.1 dB/cm at 5 MHz and up to ±2.5 dB/cm at 30 MHz.

Changes in the microbubble size distribution and microbubble number density must also be considered. Sec. 5.3 shows that the bubble size distribution changes over time, tending towards an increase in bubble size that can reach a maximum of 33% (causing a larger attenuation coefficient due to an increase in the scattering). Alternatively, over time, microbubble contrast agents may dissolve or get damaged by the introduction of air into the vial, causing a reduction in the bubble number density, and leading to a lower attenuation.

As with all the experimental measurements performed, all systematic errors due to the apparatus used can be considered negligible, since they are factored out when computing the ratio of rms voltages.

	1% HCT + 0.1 µl/ml *Optison®* δ_α (dB/cm)	45% HCT + 0.1 µl/ml *Optison®* δ_α (dB/cm)	1% HCT + 1 µl/ml *Optison®* δ_α (dB/cm)	45% HCT + 1 µl/ml *Optison®* δ_α (dB/cm)
5 MHz	0.21	0.31	0.47	0.14
15 MHz	0.06	0.09	0.15	0.15
25 MHz	0.05	0.15	0.19	0.20
30 MHz	0.04	0.28	0.07	0.33

Table 5.12 Precision error for the attenuation coefficient of a 1% and 45% suspension of red blood cells with the addition of 0.1 µl/ml (6.5×10^4 microbubbles/ml) and 1 µl/ml (6.5×10^5 microbubbles/ml) of *Optison®*.

	Saline + 0.1 µl/ml *Optison®* δ_α (dB/cm)	Saline + 1µ/ml *Optison®* δ_α (dB/cm)
5 MHz	0.38	0.47
15 MHz	0.06	0.10
25 MHz	0.04	0.15
30 MHz	0.03	0.07

Table 5.13 Precision error for the attenuation coefficient of 0.1 µl/ml ($6.5x10^4$ microbubbles/ml) and 1 µl/ml ($6.5x10^5$ microbubbles/ml) of *Optison®* in isotonic saline.

5.5 SNR of *Optison®* Microbubbles in Suspensions of Red Blood Cells

The SNR of microbubbles in suspensions of red blood cells was computed for two different hematocrits (1% and 45%) and two different *Optison®* microbubble concentrations (0.1 µl/ml or $6.5x10^4$ microbubbles/ml and 1 µl/ml or $6.5x10^5$ microbubbles/ml) as a function of frequency. The choice of a low and high hematocrit was made to mimic two situations in which the red blood cells had approximately the same scattering properties (based on the theory developed in Sec. 3.1.1), but in one case were very far apart and in the other case very tightly packed. The two different microbubble concentrations were chosen to mimic the clinical dose (0.1 µl/ml) and the maximum allowable dose (1 µl/ml) per treatment. Using results from the measurements of the SNR, important insight can be obtained on how different hematocrit and microbubble concentrations affect the detection and imaging of microbubbles in blood.

Experimentally, the SNR is computed from Eq. (4.11) corrected for the attenuation obtained from the data presented in Sec. 5.4. The theory to which the data was compared was the one developed in Sec. 3.3.2 with the SNR defined as in Eq. (3.13).

5.5.1 SNR for 0.1 µl/ml of *Optison*® in 1% and 45% hematocrit red blood cells

Figure 5.15, Figure 5.16, and Table 5.14 display the results for the SNR of suspensions of 1% and 45% hematocrit red blood cells with the clinical dose of *Optison*® microbubbles. Results in the 1% hematocrit suspension display a reduction in the SNR of 18.9 dB over the 5-30 MHz frequency range going from a maximum of 22.3 dB at 5 MHz, to a minimum of 3.4 dB at 30 MHz. Similarly, for the 45% hematocrit red blood cell suspension, the reduction in SNR was about 17.4 dB going from a maximum of 17.7 dB to a minimum of 0.3 dB. For both hematocrit concentrations, the increase in frequency has caused a dramatic increase in the contribution of the red blood cells to the scattering. For 1% hematocrit, the two populations of scatterers were almost indistinguishable at 30 MHz, while for 45% hematocrit the SNR was nearing 0 dB at and above 25 MHz.

	1% HCT + 0.1 µl/ml *Optison*® (dB)	45% HCT + 0.1 µl/ml *Optison*® (dB)
5 MHz	22.3±0.9	17.7±0.4
15 MHz	14.0±1.2	4.6±0.8
25 MHz	5.0±0.9	0.4±0.7
30 MHz	3.4±1.3	0.3±1.3

Table 5.14 Results of the SNR for the clinical dose (0.1 µl/ml or 6.5×10^4 microbubbles/ml) of *Optison*® microbubbles in a 1% and 45% hematocrit suspension of red blood cells. Uncertainties indicate the precision error and will be explained in Sec. 5.5.3.

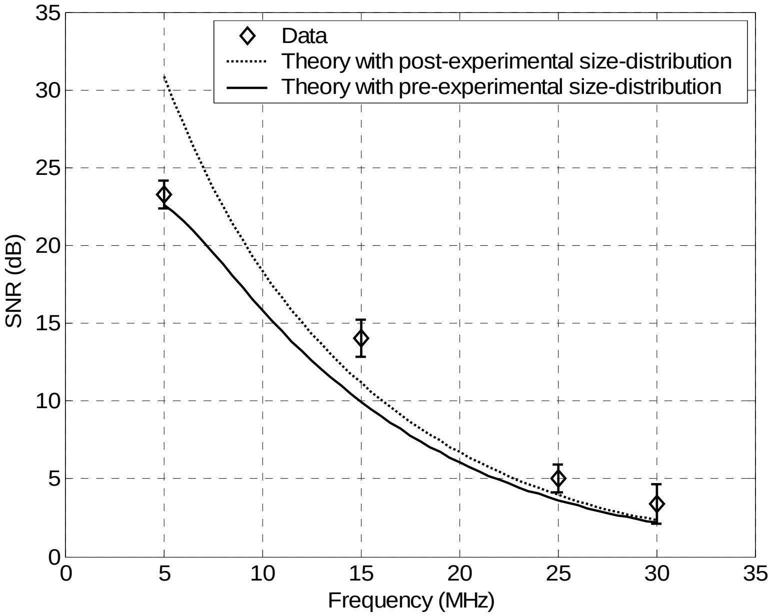

Figure 5.15 SNR for the clinical dose (0.1 µl/ml or 6.5x10^4 microbubbles/ml) of *Optison*® microbubbles in a 1% hematocrit suspension of red blood cells. Error bars indicate precision error.

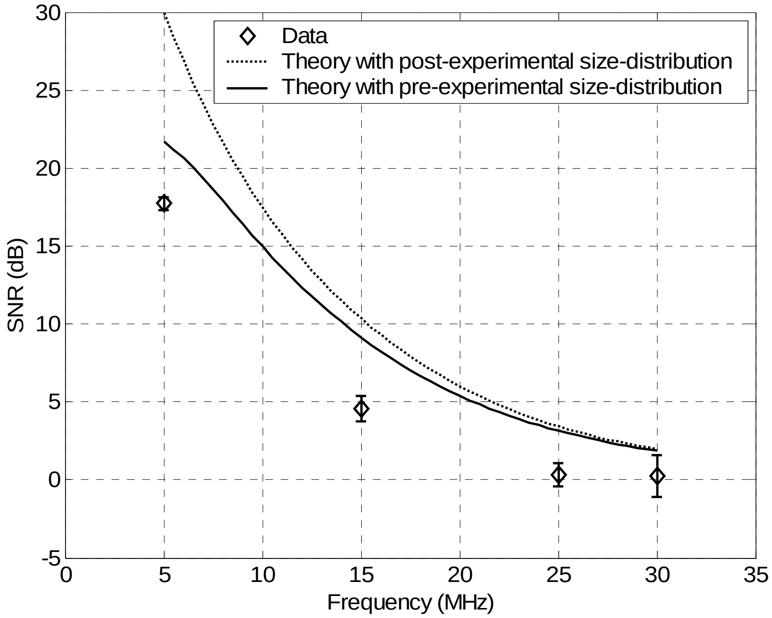

Figure 5.16 SNR for the clinical dose (0.1 µl/ml or 6.5x10^4 microbubbles/ml) of *Optison*® microbubbles in a 45% hematocrit suspension of red blood cells. Error bars indicate precision error.

The 1% hematocrit data points given in Figure 5.15 are compared to theoretical formulations of the SNR using the initial and final size distributions of *Optison*® microbubbles. Results are in good agreement with the theory using the final size distribution of *Optison*® microbubbles, except for the 5 MHz point, that seems to better agree with the theory using the initial size distribution. This difference can be explained by the fact that the 5 MHz data points were the first points collected during the experiment, followed by the 25 MHz, 30 MHz, and 15 MHz data points. Therefore, it seems as if the size of the bubbles was close to the initial size distribution for the first measurements and then quickly reached a state that agreed better with the final size distribution of *Optison*® microbubbles. In general, the 1% hematocrit data slightly overshoots the theory, suggesting that the combined contribution of the blood and microbubbles might be larger than the sum of the individual contributions. In addition, errors such as hematocrit and bubble number density uncertainties might also have contributed to this small difference and will be later discussed in Sec. 5.5.3.

The data points displayed in Figure 5.16 for the clinical dose (0.1 µl/ml) of *Optison*® in a 45% hematocrit suspension of red blood cells seem to undershoot the theory. The data trend is in better agreement with the theory that uses the final size distribution of microbubbles, leading us to believe that the time frame in which the bubbles changed in size was very small.

At 45% hematocrit, the red blood cells are no longer spread out in space. This tighter packing of the cells has caused the mixture of blood and microbubbles to scatter less than the two populations would independently, therefore leading to a lower SNR than what was expected. Since the microbubbles are the dominating scatterers, it is reasonable to believe that the tighter packing of the red blood cells has caused an inhibition in the response of the microbubbles. It can therefore be concluded, that at the clinical dose of *Optison*® and at the physiological hematocrit, the two populations of scatterers are not independent of each other leading, to a lower signal-to-noise ratio than what might be expected from theory.

A good way of visualizing this result is by showing both the 1% hematocrit and the 45% hematocrit results on the same plot, as in Figure 5.17. The theoretical formulations for 1% hematocrit and 45% hematocrit are very similar to each other, since the scattering from the red blood cell suspensions is comparable at those hematocrits. On the other hand, the downward shift towards a lower SNR in the data points is much larger than that of the theory, suggesting that the increased packing of red blood cells has introduced an additional mechanism leading to an added reduction in the SNR. This mechanism is believed to be an inhibition in the motion of the bubbles causing their inability to oscillate and leading to a lower backscatter coefficient.

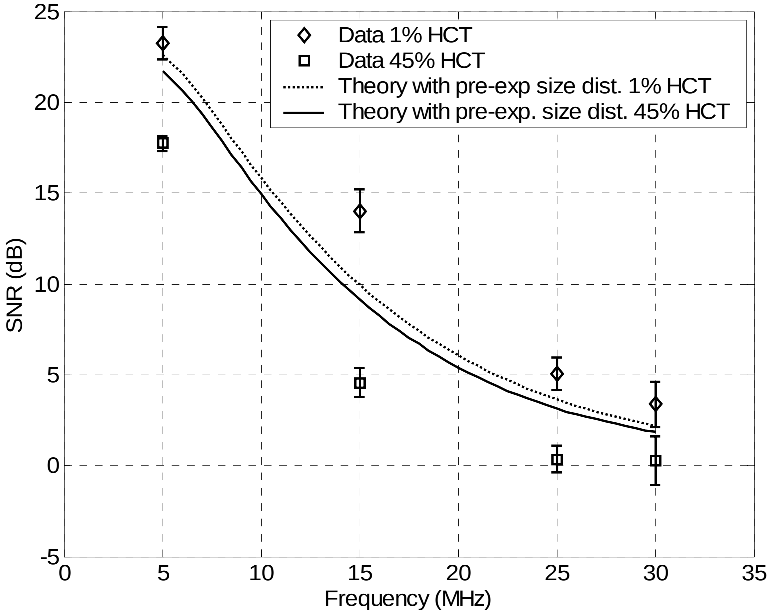

Figure 5.17 Comparison between the SNR for the clinical dose (0.1µl/ml or 6.5x10^4 microbubbles/ml) of *Optison*® microbubbles in suspensions of 1% and 45% hematocrit red blood cells. Also plotted are the theoretical formulations using the initial size distributions of *Optison*®. Error bars indicate the precision error.

5.5.2 SNR for 1 µl/ml of *Optison*® in 1% and 45% hematocrit red blood cells

Similarly to what was observed in Sec. 5.5.1, when the concentration of *Optison*® microbubbles was increased by a factor of 10 to 1 µl/ml, the SNR exhibited a reduction of 19.9 dB in the 1% hematocrit suspension and 25.1 dB in the 45% hematocrit suspension. The increase in bubble concentration has therefore caused the SNR to be higher than the 0.1 µl/ml case, going from 31.0 dB at 5 MHz to 11.1 dB at 30 MHz for the 1% hematocrit suspension. At 1% hematocrit, the reduction in SNR over that frequency range was significant (20 dB), but the scattering from the microbubbles can still be distinguished from the scattering from red blood cells at 30 MHz. On the other hand, when the red blood cell concentration was increased to 45% hematocrit, the SNR decreased from a maximum of 25.9 dB at 5 MHz to 0.8 dB at 30 MHz, meaning that the microbubble contribution to the overall scattering becomes negligible at the higher frequencies. It therefore seems that the high red blood cell concentration has caused a much larger impact on the reduction in SNR than the low hematocrit concentration.

	1% HCT + 1 µl/ml *Optison*® (dB)	45% HCT + 1 µl/ml *Optison*® (dB)
5 MHz	31.0±1.4	25.9±0.7
15 MHz	22.3±0.9	9.8±0.6
25 MHz	13.2±0.9	0.9±0.7
30 MHz	11.1±1.0	0.8±1.1

Table 5.15 Results of the SNR for 1 µl/ml (6.5×10^5 microbubbles/ml) of *Optison*® microbubbles in a 1% and 45% hematocrit suspension of red blood cells. Uncertainties indicate the precision error and will be explained in Sec. 5.5.3.

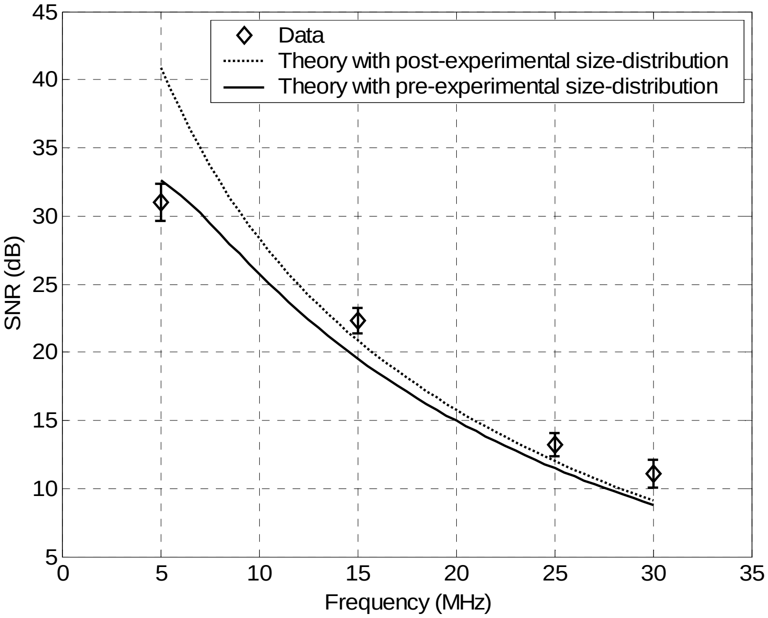

Figure 5.18 SNR for 1 µl/ml (6.5x10^5 microbubbles/ml) of *Optison*® microbubbles in a 1% hematocrit suspension of red blood cells. Error bars indicate precision error.

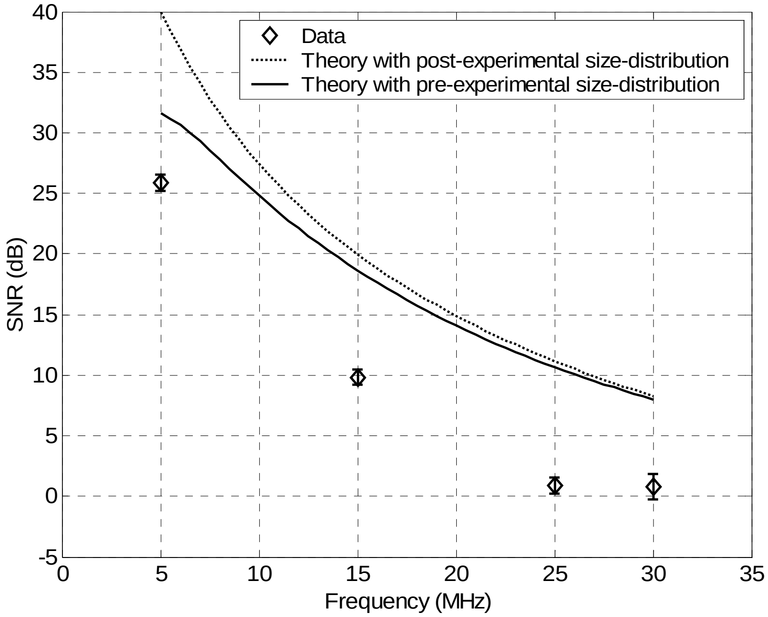

Figure 5.19 SNR for 1µl/ml (6.5x10^5 microbubbles/ml) of *Optison*® microbubbles in a 45% hematocrit suspension of red blood cells. Error bars indicate precision error.

In Figure 5.18 and Figure 5.19, one can observe how the reduction in SNR for the *Optison*® microbubbles at 1 µl/ml only approaches 0 dB for the 45% hematocrit case. Data points for the 1% hematocrit suspension are in good agreement with the theory using the post-experimental *Optison*® size distribution except for the 5 MHz point, which agrees better with the initial size distribution. The fact that the theory slightly underestimates the data may be due to uncertainties in the bubble number density or in the hematocrit measurement. However, the theoretical prediction, which is based on the premise that the two populations of scatterers do not interact, is in good agreement with the data. This indicates that, at the low red blood cell concentrations, the two populations of scatterers are indeed independent of each other.

On the other hand, the data displayed in Figure 5.19 indicates that the measured SNR is much lower than predicted by theory. The general trend of the data indicates quantitative agreement with the theory based on the final post-experimental size distribution of *Optison*® microbubbles, but is shifted to a significantly lower SNR. This suggests that the two populations of scatterers no longer scatter independently. Once more, it seems as though the tighter packing of the red blood cells has caused the mixture of microbubbles and blood to scatter less. This decreased response could be due either to multiple scattering effects, not accounted for by the theory, or to an inhibition of the bubble motion, leading to smaller bubble pulsations and therefore a smaller backscatter coefficient. The important conclusion to draw is that at the human physiological hematocrit and ten times the clinical dosage of *Optison*® the SNR still tends to zero at 25 and 30 MHz, therefore eliminating the image enhancement that might be produced by the contrast agent.

To better visualize the aforementioned results, Figure 5.20 displays the SNR for both the 1% hematocrit and 45% hematocrit red blood cell suspensions with 1 µl/ml of *Optison*® on the same plot with their respective theory. Similarly to the 0.1 µl/ml of *Optison*® case, the theoretical curves for the SNR in 1% hematocrit and 45% hematocrit blood, which are nearly identical, slightly underestimate the 1% hematocrit data, but greatly overestimate the 45% hematocrit data.

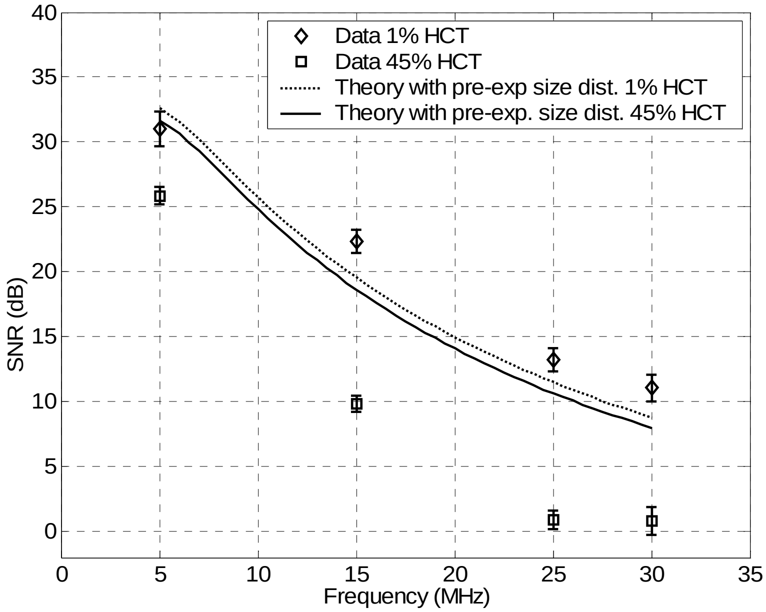

Figure 5.20 Comparison between the SNR for 1 µl/ml ($6.5\text{x}10^5$ microbubbles/ml) of *Optison*® microbubbles in suspensions of 1% and 45% hematocrit red blood cells. Also plotted are the theoretical formulations using the initial size distributions of *Optison*®. Error bars indicate the precision error.

5.5.3 Uncertainty analysis

The precision error for the SNR of *Optison*® microbubbles in blood was computed in the same manner as in Eq. (5.8) and (5.11) with results displayed in Table 5.16. Precision error values increased in percentage as a function of frequency, going from a minimum of 2.5% at 5 MHz to a maximum of 500% at 30 MHz for 1 µl/ml of *Optison*®. Such behavior can be explained by the fact that as the SNR approaches zero, there is no scattering mechanism that dominates over the other, leading to larger fluctuations from a mean value.

	δ_{SNR} 1% HCT + 0.1 µl/ml *Optison*® (dB)	δ_{SNR} 45% HCT + 0.1 µl/ml *Optison*® (dB)	δ_{SNR} 1% HCT + 1 µl/ml *Optison*® (dB)	δ_{SNR} 45% HCT + 1 µl/ml *Optison*® (dB)
5 MHz	0.9	0.4	1.4	0.7
15 MHz	1.2	0.8	0.9	0.6
25 MHz	0.9	0.7	0.9	0.7
30 MHz	1.3	1.3	1.0	1.1

Table 5.16 Precision error in the measurements of the SNR of the clinical dose 0.1 µl/ml (6.5×10^4 microbubbles/ml) and the maximum dose 1 µl/ml (6.5×10^5 microbubbles/ml) of *Optison*® microbubbles in suspensions of 1% hematocrit and 45% hematocrit red blood cells.

In addition to errors associated with the precision of the current measurements, bias uncertainties must also be considered. Assuming that the experimental setup and apparatus did not introduce any bias errors because all errors got factored out when taking the ratio of rms voltages, errors associated with hematocrit, bubble number density, and bubble size distribution were the three main sources of uncertainty in the experiment. The effect of size distribution became smaller as the frequency was increased, from about 8 dB at 5 MHz to 0 dB at 30 MHz, and was unaffected by changes in hematocrit. Similarly, the error associated with the number density of microbubbles present in the investigated samples did not depend on the hematocrit and was found to amount to about 1-2 dB over the frequency range.

The error associated with hematocrit was found to be the most influential error at the low 1% hematocrit. This error introduced an almost constant 5 dB shift between the theoretical formulations, while it was considered negligible at the high 45% hematocrit value.

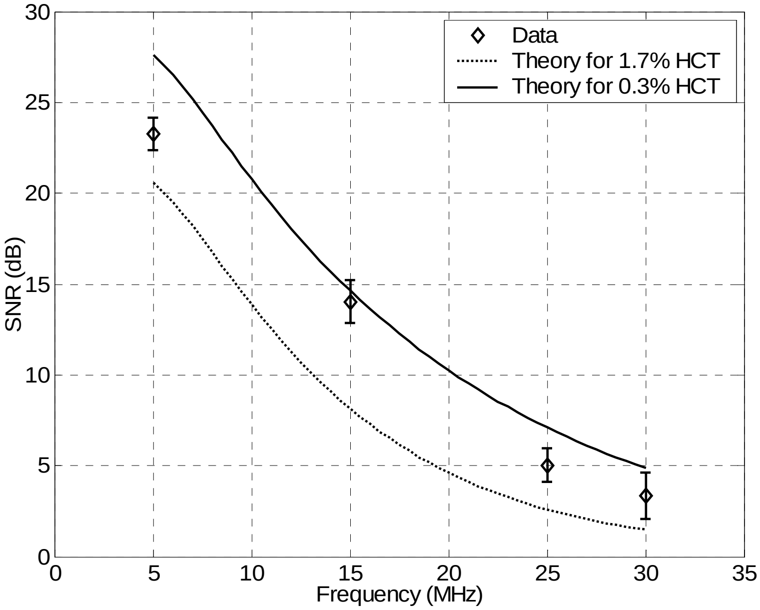

Figure 5.21 Influence of the error in hematocrit for the clinical dose (0.1µl/ml or 6.5x10^4 microbubbles/ml) of *Optison*® in a 1% suspension of red blood cells.

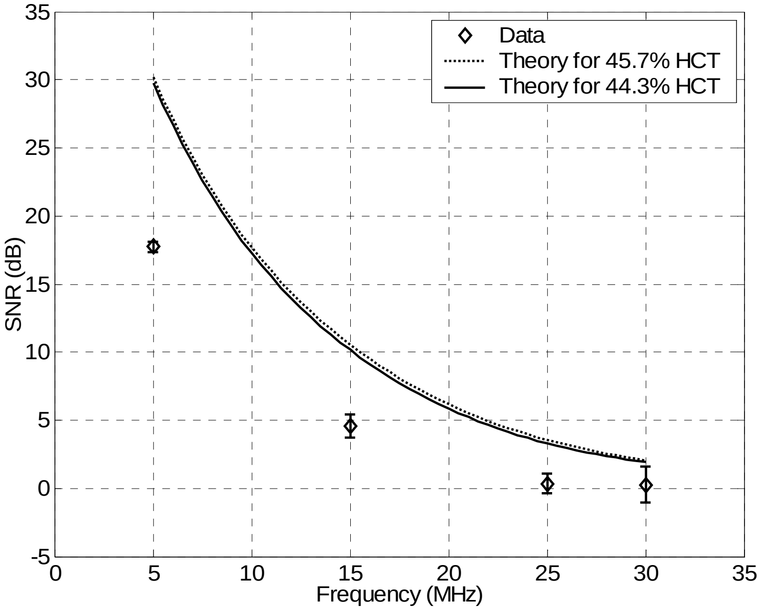

Figure 5.22 Influence of the error in hematocrit for clinical dose (0.1 µl/ml or 6.5x10^4 microbubbles/ml) *Optison*® in a 45% suspension of red blood cells.

As previously stated, the bias error associated with the hematocrit was determined to be 0.71%. Figure 5.21 and Figure 5.22 give an example of the influence that the uncertainty in hematocrit has on the theory for determining the SNR of clinical dose (0.1 µl/ml) of *Optison*® microbubbles in blood at 1% and 45% hematocrit respectively. It was found that the hematocrit uncertainty had a much larger influence in the results at 1% (Figure 5.21) compared to 45% (Figure 5.22). This can be explained by the fact that, as can be seen from Figure 3.1, the slope of the BSC vs. hematocrit curve is much steeper at the lower hematocrits around 1% than it is around 45%. In addition, the direction in which the curve shifts is inverted for 1% and 45% hematocrit. This occurs because the BSC of red blood cells increases at as a function of hematocrit below 13% hematocrit while it decreases at the higher hematocrits.

Figure 5.21 therefore shows that at 1% hematocrit, a slight change in the hematocrit level can cause a large shift in the theory, and that any differences between theory and data can be accounted for by this error. On the other hand, Figure 5.22 shows that at 45% hematocrit, the uncertainty in hematocrit is barely noticeable and therefore is not sufficient to explain the difference between theory and experiment.

Another error that must be considered is that associated with the microbubble number density. In all the previous theoretical computations, the average number density of microbubbles contained within an *Optison®* vial (6.5×10^8 bubbles/ml) and provided by the manufacturer of *Optison*® was used [70]. This number density can vary from a minimum of 5×10^8 bubbles/ml to a maximum of 8×10^8 bubbles/ml. Figure 5.23 gives an example of how the bubble number density can influence the theoretical formulation of the SNR. This error can cause a shift in the SNR of no more than 1-2 dB over the 5-30 MHz frequency range.

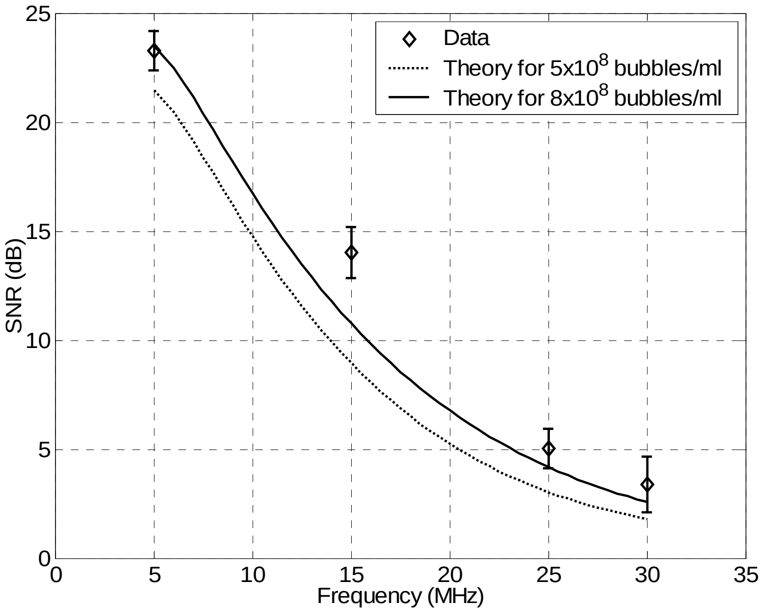

Figure 5.23 Sample plot showing the influence of the uncertainty in number density on the SNR of the clinical dose (0.1 µl/ml) of *Optison*® microbubbles in a 1% hematocrit suspension of red blood cells.

Of all the errors discussed in the present section, the uncertainty in hematocrit was found to be the most influential when considering the 1% hematocrit suspensions of red blood cells. Conversely, this error had a very small influence on the 45% hematocrit suspensions. Additional errors due to the bubble number density and bubble size distribution could lead to an additional shift in the theory curves both at 1% and 45% hematocrit. All of the sources of error just discussed can explain the discrepancies between theory and experiment for the 1% hematocrit suspensions of red blood cells. On the other hand, at the higher 45% hematocrit concentration, the discrepancies cannot be explained from just error analysis. Additional mechanisms must be present when the packing of red blood cells increases that cause an additional reduction in the SNR.

Chapter 6

Conclusions and Future Work

The purpose of this thesis was to address and investigate the frequency dependent acoustic scattering in the 5-30 MHz range, from a strong scatterer (cylindrical wire target) or suspensions of strong scatterers (microbubble contrast agents) in suspensions of weakly scattering red blood cells. Important parameters such as the red blood cell concentration (hematocrit) and microbubble concentration were included in the study to make the problem clinically relevant and determine the dominant parameters that affect the imaging and detection of microbubbles in blood. The hypothesis was that, since blood cells are weak Rayleigh scatterers (BSC is proportional to f^4) and most contrast agents are strong scatterers (BSC is proportional to f^0), as frequency increases the echo return from the former eventually overwhelms the latter and the efficacy of the contrast agent is compromised.

An active cavitation detector operating in the 5-30 MHz range was successfully implemented for measuring the backscatter of suspensions of red blood cells, cylindrical tungsten and fiberglass wire targets, and suspensions of *Optison*® microbubbles. Measurements of the attenuation of pure red blood cells at different concentrations (3.5-50% hematocrit) and the attenuation of red blood cells (1% and 45% hematocrit) with the addition of *Optison*®

microbubbles at two different concentrations (0.1 µl/ml and 1 µl/ml) were performed. The lower concentration corresponding to 6.5×10^4 microbubbles/ml is the clinical dose of *Optison®*, while the higher concentration corresponding to 6.5×10^5 microbubbles/ml is the maximum allowable dose.

A convenient method was devised for easily comparing the influence of microbubbles on scattering from blood as a function of frequency, hematocrit, and microbubble concentration. This method consisted in determining a signal-to-noise ratio (SNR) by measuring the backscattered return from different hematocrit suspensions of red blood cells with the addition of different concentrations of *Optison*® microbubble contrast agent. SNR results were compared to a theoretical formulation that summed the contributions of the red blood cells and microbubble contrast agents to obtain the overall backscattering coefficient. The weak scattering Born approximation was used to formulate expressions for the backscattering from red blood cells, while shelled bubble dynamics theory was used to determine the backscattering from the *Optison*® microbubbles. The underlying assumption in the theoretical formulation was that the two populations of scatterers were far enough apart to behave independently, with no multiple scattering effects present, and satisfied the Watermann-Truell condition.

6.1 Attenuation

6.1.1 Attenuation through suspensions of red blood cells

Attenuation measurements were performed at 5, 15, 25, and 30 MHz for six hematocrit values in the 3.5%-50% range. The measured attenuation was found to increase with increasing frequency and hematocrit and exhibited a power law regression. The frequency dependence was found to range from $f^{1.6}$ at 5% hematocrit to $f^{1.1}$ at 50% hematocrit. The hematocrit dependence was found to be $H^{0.76}$ at 5 MHz to $H^{0.44}$ at 30 MHz. Attenuation through suspensions of red blood cells was therefore linear in frequency at the high hematocrits (30% and above) and linear in hematocrit at the lower frequencies (5 MHz and below). In between, results were found to accurately follow a power law with coefficients given in Table 5.2-Table 5.3. The most important source of error affecting attenuation measurements was found to be the uncertainty in hematocrit, causing uncertainties in the attenuation values that ranged from ±0.1 dB/cm at 5 MHz to ±2.5 dB/cm at 30 MHz.

6.1.2 Attenuation through suspensions of red blood cells and *Optison®*

Attenuation measurements were also performed for a suspension of 0.1 and 1 µl/ml of *Optison®* microbubbles in 1% and 45% hematocrit red blood cells. Results indicated that no additional attenuation was introduced by adding 0.1 µl/ml of *Optison®* to the red blood cell suspension both at 1% and 45% hematocrit, with results matching those of pure red blood cells given in Sec. 6.1.1. On the other hand, the addition of 1 µl/ml of *Optison®* to the red blood cell suspension caused an increase in the attenuation coefficient of approximately 1.8-3.3 dB/cm for the 1% hematocrit suspension and 0.4-1 dB/cm for the 45% hematocrit suspension in the 15-30 MHz range. At 5 MHz, the increase was found to be 16-17.5 dB/cm. One can therefore infer from the results that the higher microbubble concentration introduced an additional attenuation effect that was largest at 5 MHz, where many bubbles are of resonance size. In addition, attenuation effects due to the *Optison®* microbubbles were larger at 1% hematocrit, where the particles are loosely packed, compared to 45% hematocrit, where the particles are more tightly packed. It is therefore believed that the tighter packing of the red blood cells inhibited the microbubble response, leading to lower attenuation measurements.

The parameters found to most strongly affect the attenuation of microbubbles in blood in addition to frequency were therefore microbubble concentration, where an increase by a factor of

10 (from the clinical dose of .01 µl/ml to the maximum dose of 1 µl/ml) led to an increased attenuation of about 0.4-3.3 dB/cm and hematocrit, where the tighter packing was found to cause a decrease in the attenuation coefficient. The clinical dose of *Optison*® was found to produce no attenuation in addition to that already caused by the red blood cell suspensions, while the maximum dose of *Optison*® was found to cause significant additional attenuation.

6.2 Signal-To-Noise Ratio

The SNR was measured for a cylindrical fiberglass wire and a cylindrical tungsten wire target in suspensions of 13% hematocrit red blood, showing a decrease of 30 dB and 40 dB respectively over the 5-30 MHz frequency range. Measurements were then obtained for the SNR of *Optison*® microbubbles in blood for two concentrations of *Optison*®, 0.1 µl/ml and 1 µl/ml, and two hematocrit levels, 1% and 45%.

Results for both 0.1 µl/ml and 1 µl/ml suspensions of *Optison*® in 1% hematocrit red blood cells showed a decrease of 18.9 dB and 19.9 dB over the 5-30 MHz range. Indeed, at 30 MHz, 0.1 µl/ml of *Optison*® were found to produce no image enhancement and could not be clearly distinguished from the weakly scattering red blood cells. At the maximum dosage of *Optison*®, on the other hand, the microbubbles were still distinguishable from the blood (SNR = 11.1 dB). The aforementioned results were found to be in good agreement with the theoretical formulation for the SNR leading to the assumption that at low hematocrits the two populations of scatterers, red blood cells and microbubbles, scatter sound independently.

At 45% hematocrit, the reduction in SNR was found to be 17.4 dB and 25.1 dB for the 0.1 µl/ml and 1 µl/ml suspensions of *Optison*® respectively. Beyond 25 MHz, the scattering from the red blood cells was found to greatly dominate the scattering from *Optison*® microbubbles both at the clinical dosage and the maximum dosage. Therefore, at the physiological hematocrit, the image enhancement produced by the *Optison*® contrast agent was found to be negligible beyond 25 MHz, inhibiting our ability to detect microbubbles. Theoretical predictions were found to greatly overestimate experimental data, suggesting that at 45% hematocrit, the two populations of scatterers are no longer independent, and additional phenomena have caused an increased reduction in the SNR. Such phenomena may be attributed to an inhibition of bubble motion due to the tighter packing of the red blood cell suspensions.

In addition to frequency, hematocrit, and microbubble concentration, microbubble size distribution and microbubble number density were parameters that were found to play important roles when imaging *Optison*® in blood. Over time, the size distribution of *Optison*® microbubbles was found to grow, leading to a change in SNR going from a maximum of 8 dB at 5 MHz to a minimum of 0 dB at 30 MHz. In addition, the number of bubbles per unit volume could also decrease over time, leading to a maximum decrease in SNR of about 2 dB in the 5-30 MHz range. Therefore, the most relevant parameters for the imaging and detection of *Optison*® microbubbles in blood were found to be, in order of importance, frequency, hematocrit, microbubble concentration, microbubble size distribution, and microbubble number density.

From the experimental data collected in the present study we can confirm the hypothesis stated in the early part of the present chapter: as the imaging frequency is increased, echo returns from strong scattering contrast agents are overwhelmed by those of weak scattering red blood cells. It was shown that beyond 25 MHz, the image-enhancement effects of *Optison®* at the physiological hematocrit (45%) were no longer present. Therefore, in a clinical environment, it is very important to consider the contribution of weakly scattering particles as the imaging frequency is increased, even in the presence of well known strongly-scattering particles. This conclusion challenges the common belief that higher frequencies always imply better ultrasound images.

In addition, effects associated with the proximity of particles suggested, for the case of *Optison®* in suspensions of red blood cells, that at high hematocrit values, the two populations of scatterers no longer scatter independently. The closer proximity of the red blood cells was shown to cause an additional decrease in SNR results, suggesting that the tighter packing of the red blood cells had caused an inhibition in the response of the microbubble contrast agents.

6.3 Suggestions for Future Work

Work from the current research can be expanded in both its theoretical and experimental parts. Theoretically, the development of a model that accounts for how the red blood cells may or may not impede the motion of bubbles is needed. Such a model would allow us to predict the downward shift in SNR at the higher hematocrits and better understand the way microbubbles interact with blood cells. In addition, the development of a model for the attenuation of suspensions of *Optison*® microbubbles would be an effective tool to validate and predict the anomalous behavior of the attenuation coefficient around resonance.

Experimentally, the project could be extended to include other parameters such as the driving pressure and the duty cycle of the insonifying acoustic field. The increase in driving pressure would allow us to observe non-linear effects associated with cavitation as well as allowing us to determine thresholds for the rupturing of contrast agents in the presence of red blood cells. An increase in the duty cycle, instead, could allow us to observe effects associated with the rectified diffusion of the bubbles (diffusion of gas into the bubbles through the use of the sound field) and see how the size distribution of microbubble contrast agents varies as a function of duty cycle. Experiments could also be repeated with different batches of *Optison*® to observe how the SNR varies from batch to batch. Unfortunately, the quantity of *Optison*® available for the present project was very limited due to the high cost of the product. Additional suggestions include looking at transient effects that occur when working with *Optison*® contrast agents, such as the dominant time constants associated with bubble-growth over time and with the perceived decrease in bubble density. In addition, free cavitating microbubbles could be generated with a HIFU source and driven inertially to observe how the SNR changes once inertial effects start taking place.

Based on the results obtained in the present work, one may conclude that above 25 MHz the image-enhancing properties of *Optison*® at its clinical dose and at physiological hematocrit are no longer present. Results were found to be very dependent on the hematocrit, leaving room for additional experiments at intermediate hematocrit levels between 1% and 45%. Supplementary experimental results would then allow to determine at what hematocrit level the red blood cells can be considered “packed” and the theory starts deviating from the observed experimental results.

Appendices

Appendix A – Coefficients for Eq. (2.63)

$x_{1c} = k_{1c}\mathrm{b}$; $x_{1cs} = k_{1cs}\mathrm{b}$; $x_2 = k_2\mathrm{b}$; $\mathrm{y}_{1c} = k_{1c}\mathrm{a}$; $\mathrm{y}_{1s} = k_{1s}a$; $\mathrm{y}_{1g} = k_{1g}a$

$$\alpha_{12} = \left(2\rho_1 / x_{1s}{}^2\right)\left[\left(x_{1c}{}^2 - \frac{1}{2}x_{1s}{}^2\right) j_n\left(x_{1c}\right) + x_{1c}{}^2 j_n''\left(x_{1c}\right)\right]$$

$$\alpha_{13} = \left(2\rho_1 / x_{1s}{}^2\right)\left[\left(x_{1c}{}^2 - \frac{1}{2}x_{1s}{}^2\right) n_n\left(x_{1c}\right) + x_{1c}{}^2 n_n''\left(x_{1c}\right)\right]$$

$$\alpha_{14} = \left(2\rho_1 / x_{1s}{}^2\right) n\left(n+1\right)\left[x_{1s} j_n'\left(x_{1s}\right) - j_n\left(x_{1s}\right)\right]$$

$$\alpha_{15} = \left(2\rho_1 / x_{1s}{}^2\right) n\left(n+1\right)\left[x_{1s} n_n'\left(x_{1s}\right) - n_n\left(x_{1s}\right)\right]$$

$$\alpha_{22} = x_{1c} j_n'\left(x_{1c}\right)$$

$$\alpha_{23} = x_{1c} n_n'\left(x_{1c}\right)$$

$$\alpha_{24} = n\left(n+1\right) j_n\left(x_{1s}\right)$$

$$\alpha_{25} = n\left(n+1\right) n_n\left(x_{1s}\right)$$

$$\alpha_{32} = 2\left[x_{1c} j_n'\left(x_{1s}\right) - j_n\left(x_{1c}\right)\right]$$

$$\alpha_{33} = 2\left[x_{1c} n_n'\left(x_{1s}\right) - n_n\left(x_{1c}\right)\right]$$

$$\alpha_{34} = \left(n^2 + n - 2\right) j_n\left(x_{1s}\right) + x_{1s}{}^2 j_n''\left(x_{1s}\right)$$

$$\alpha_{35} = \left(n^2 + n - 2\right) n_n\left(x_{1s}\right) + x_{1s}{}^2 n_n''\left(x_{1s}\right)$$

$$\alpha_{42} = \left(2\rho_1 / {y_{1s}}^2\right)\left[\left({y_{1c}}^2 - \frac{1}{2}{y_{1s}}^2\right) j_n\left(y_{1c}\right) + {y_{1c}}^2 j_n''\left(y_{1c}\right)\right]$$

$$\alpha_{43} = \left(2\rho_1 / {y_{1s}}^2\right)\left[\left({y_{1c}}^2 - \frac{1}{2}{y_{1s}}^2\right) n_n\left(y_{1c}\right) + {y_{1c}}^2 n_n''\left(y_{1c}\right)\right]$$

$$\alpha_{44} = \left(2\rho_1 / {y_{1s}}^2\right) n\left(n+1\right)\left[y_{1s} j_n'\left(y_{1s}\right) - j_n\left(y_{1s}\right)\right]$$

$$\alpha_{45} = \left(2\rho_1 / {y_{1s}}^2\right) n\left(n+1\right)\left[y_{1s} n_n'\left(y_{1s}\right) - n_n\left(y_{1s}\right)\right]$$

$$\alpha_{46} = \rho_{1g}\, j_n''\left(y_{1g}\right)$$

$$\alpha_{52} = y_{1c}\, j_n'\left(y_{1c}\right)$$

$$\alpha_{53} = y_{1c} n_n'\left(y_{1c}\right)$$

$$\alpha_{54} = n\left(n+1\right) j_n\left(y_{1s}\right)$$

$$\alpha_{55} = n\left(n+1\right) n_n\left(y_{1s}\right)$$

$$\alpha_{56} = -y_{1g}\, j_n'\left(y_{1g}\right)$$

$$\alpha_{62} = 2\left[y_{1c}\, j_n'\left(y_{1s}\right) - j_n\left(y_{1c}\right)\right]$$

$$\alpha_{63} = 2\left[y_{1c} n_n'\left(y_{1s}\right) - n_n\left(y_{1c}\right)\right]$$

$$\alpha_{64} = \left(n^2 + n - 2\right) j_n\left(y_{1s}\right) + {y_{1s}}^2 j_n''\left(y_{1s}\right)$$

$$\alpha_{65} = \left(n^2 + n - 2\right) n_n\left(y_{1s}\right) + {x_{1s}}^2 n_n''\left(y_{1s}\right)$$

Appendix B – MATLAB Scripts

MATLAB Code for the Scattering From Red Blood Cells

```
% The purpose of this code is to derive a solution for the scattering from
% red blood cells using the fluid sphere solution, Born approximation, and
% Rayleigh approximation.

%==================================================================
%=========================Fluid Sphere Solution==========================

 clear all;

%Define all constants

Po = .1e6;                              % Ambient pressure
r = 1;                                  % Observation point
theta = pi;                             % Angle of observation
a = 2.5e-6;                             % Radius of the sphere
f = linspace(.1e6, 100e6, 20);          % Frequency range
omega = 2*pi*f;                         % Angular frequency range

rho0 = 1004;                            % Density of fluid
rho1 = 1.087E3;                         % Density of scatterer

c0 = 1541;                              % Sound speed in fluid
c1 = 1609.8;                            % Sound speed in scatterer

g = rho1/rho0;                          % Ratio of densities
h = c1/c0;                              % Ratio of sound speeds
z = g*h;

numax = 8;                              % Maximum number of points

%Wavenumbers

k0 = omega./c0;
k1 = omega./c1;


% Argument of bessel functions

x(1,:) = k0.*a;
x(2,:) = k1.*a;
```

```
% Compute spherical bessel and neumann functions

for xcnt = 1:2,
     for nu = 1:numax+1,
       n = nu - 1;
       sphbsl(nu,xcnt,:) = besselj(n+0.5,x(xcnt,:)) ./ sqrt(2*x(xcnt,:)/pi);
       sphneu(nu,xcnt,:) = bessely(n+0.5,x(xcnt,:)) ./ sqrt(2*x(xcnt,:)/pi);
   end
end

% Compute derivatives of spherical bessel and neumann functions

for xcnt = 1:2,
     sphbsld(1,xcnt,:) = -sphbsl(2,xcnt,:);
     sphneud(1,xcnt,:) = -sphneu(2,xcnt,:);
     for nu = 2:numax,
         n = nu - 1;
         sphbsld(nu,xcnt,:) = 1/(2*n+1) * (n*sphbsl(nu-1,xcnt,:) - (n+1)*sphbsl(nu+1,xcnt,:));
         sphneud(nu,xcnt,:) = 1/(2*n+1) * (n*sphneu(nu-1,xcnt,:) - (n+1)*sphneu(nu+1,xcnt,:));
     end
end

% Compute alpha and beta

for xcnt = 1:2,
    for nu=1:numax,
        n=nu-1;
        alpha_n(nu,xcnt,:) = ((2*n)+1)*sphbsld(nu,xcnt,:);
        beta_n(nu,xcnt,:) = ((2*n)+1)*sphneud(nu,xcnt,:);

    end
end

alpha0(1,:) = -sphbsl(2,1,:);
alpha1(1,:) =-sphbsl(2,2,:);
beta0(1,:) = -sphneu(2,1,:);
beta1(1,:) = -sphneu(2,2,:);

for nu = 2:numax,
    n = nu - 1;

    alpha0(nu,:) = n*sphbsl(nu-1,1,:) - (n+1)*sphbsl(nu+1,1,:);
    alpha1(nu,:) = n*sphbsl(nu-1,2,:) - (n+1)*sphbsl(nu+1,2,:);

    beta0(nu,:) = n.*sphneu(nu-1,1,:)-(n+1).*sphneu(nu+1,1,:);
    beta1(nu,:) = n.*sphneu(nu-1,2,:)-(n+1).*sphneu(nu+1,2,:);
end

% Determine constant Cm from Anderson's paper

for n = 1:numax,

    sphbsl0(n,:) = sphbsl(n,1,:);
```

```
    sphbsl1(n,:) = sphbsl(n,2,:);

    sphneu0(n,:) = sphneu(n,1,:);
    sphneu1(n,:) = sphneu(n,2,:);

    term1(n,:) = (alpha1(n,:)./alpha0(n,:)) .* (sphneu0(n,:)./sphbsl1(n,:));
    term2(n,:) = (beta0(n,:)./alpha0(n,:)) * z;
    term3(n,:) = (alpha1(n,:)./alpha0(n,:)) .* (sphbsl0(n,:)./sphbsl1(n,:));
    term4 = z;

    c(n,:) = ( term1(n,:) - term2(n,:) ) ./ ( term3(n,:) - term4 );
end

% Determine the form function phi

for nu = 1:numax,
    n = nu-1;
    pn = legendre(n,cos(theta));                    % Legendre Polynomial

    phi(nu,:) = (((2*n)+1)* pn(1)) ./ ( 1+(i*c(nu,:)) );
end

PHI_180 = (1./(k0)) .* (abs(sum(phi(:,:))));        % Differential backscattering form function

sigmadbs = (PHI_180).^2./(pi*a^2);                  % Backscattering cross-section

%=====================================================================
%=====================Rayleigh Approximation==========================

kapa0=4.42E-10;                          % Compressibility of scatterer
kapa1=3.55E-10;                          % Compressibility of fluid

gamakapa=(kapa1-kapa0)/kapa0;
gamarho=(rho1-rho0)/rho1;

% Differential backscattering form function

phi180rayleigh=abs((k0.^2*(a^3))./3)*(gamakapa-(3*(rho1-rho0)/(2*rho1+rho0)));

% Backscattering cross-section

sigmah180=phi180rayleigh.^2;

%=====================================================================
%=======================Born Approximation============================

x(3,:) = (2*k0*sin(theta/2))*a;                          % New argument of Bessel Function mu*a

for nu = 1:numax+1,
     n = nu - 1;
     sphbslborn(nu,:) = besselj(n+0.5,x(3,:)) ./ sqrt(2*x(3,:)/pi);
end
```

```
% Differential backscattering form function

phi180born = (k0.^2*(a^3))*(gamakapa-gamarho).*((sphbslborn(2,:))./x(3,:));

% Backscattering cross-section

sigmah180born=phi180born.^2;
```

MATLAB Code for the Scattering from an Elastic Sphere

```
% The purpose of this code is to derive the solution for the scattered field from a full elastic sphere.
% Solution obtained from Faran's paper.

clear all;

% Define all the constants

a = 2.5E-6;                                              % Radius of the sphere
Po = 1e5;                                                % Incident wave pressure amplitude
f = linspace(.1e6, 100e6, 2000);                         % Frequency range
omega = 2*pi*f;                                          % Angular frequency range
rho1 = 2.8e3;                                            % Density of scatterer
rho3 = 1000;                                             % Density of fluid

sigma = 0.3;                                             % Poisson's ratio
E = 85e9;                                                % Young's modulus

% Determine velocities

c1 = ((E*(1-sigma))/(rho1*(1+sigma)*(1-2*sigma)))^0.5;   % Comp. velocity in scatterer
c2 = [E/(2*rho1*(1+sigma))]^0.5;                         % Shear wave vel. in scatteres
c3 = 1480;                                               % Velocity of sound in fluid

% Determine wave numbers

k1 = omega/c1;
k2 = omega/c2;
k3 = omega/c3;

%Distance of observation
r = 1;

% x-values

x(1,:) = k1*a;
x(2,:) = k2*a;
x(3,:) = k3*a;
x(4,:) = k3*r;

%Angle of observation

theta = pi;                                              % For backscatter theta = pi


% Compute spherical Bessel and Neumann functions

numax = 20;                                              % Maximum number of points

for xcnt = 1:4,
```

```
     for nu = 1:numax+1,
       n = nu - 1;
       sphbsl(nu,xcnt,:) = besselj(n+0.5,x(xcnt,:)) ./ sqrt(2*x(xcnt,:)/pi);
       sphneu(nu,xcnt,:) = bessely(n+0.5,x(xcnt,:)) ./ sqrt(2*x(xcnt,:)/pi);
   end
end

% Compute derivatives of spherical Bessel and Neumann functions

for xcnt = 1:4,
     sphbsld(1,xcnt,:) = -sphbsl(2,xcnt,:);
     sphneud(1,xcnt,:) = -sphneu(2,xcnt,:);
     for nu = 2:numax,
         n = nu - 1;
         sphbsld(nu,xcnt,:) = 1/(2*n+1) * (n*sphbsl(nu-1,xcnt,:) - (n+1)*sphbsl(nu+1,xcnt,:));
         sphneud(nu,xcnt,:) = 1/(2*n+1) * (n*sphneu(nu-1,xcnt,:) - (n+1)*sphneu(nu+1,xcnt,:));
     end
end

% Determine the intermediate angles

for xcnt = 1:4,
    for n=1:numax,
        resphbsl = reshape(sphbsl(n,:,:), 4, numel(f));
        resphbsld = reshape(sphbsld(n,:,:), 4,numel(f));
        resphneu = reshape(sphneu(n,:,:), 4, numel(f));
        resphneud = reshape(sphneud(n,:,:), 4, numel(f));
        delta(n,xcnt,:) = atan(-resphbsl(xcnt,:) ./ resphneu(xcnt,:));
        alpha(n,xcnt,:) = atan(-x(xcnt,:).*resphbsld(xcnt,:) ./ resphbsl(xcnt,:));
        beta(n,xcnt,:) = atan(-x(xcnt,:).*resphneud(xcnt,:) ./ resphneu(xcnt,:));
    end
end

% Determine the scattering phase angle

for nu=1:numax,
    n = nu - 1;
    tan1(nu,:) = tan(alpha(nu,1,:));
    tan2(nu,:) = tan(alpha(nu,2,:));
    X2 = 0.5*x(2,:).^2;
    term1(nu,:) = (tan1(nu,:)./(tan1(nu,:)+1));
    term2(nu,:) = ((n^2+n)./(n^2+n-1-X2+tan2(nu,:)));
    term3(nu,:) = ((n^2+n-X2+2*tan1(nu,:))./(tan1(nu,:)+1));
    term4(nu,:) = (((n^2+n)*(tan2(nu,:)+1))./(n^2+n-1-X2+tan2(nu,:)));

    zeta(nu,:) = atan( (-X2).*(term1(nu,:)-term2(nu,:))./(term3(nu,:)-term4(nu,:)));
end


% Determine the boundary impedance phase angle

for n=1:numax,
    tan_phi(n,:) = -(rho3/rho1)*tan(zeta(n,:));
```

```
end

% Phase shift of the nth scattered wave

for n=1:numax,
    tanalpha(n,:) = tan(alpha(n,3,:));
    tanbeta(n,:) = tan(beta(n,3,:));
    tandelta(n,:) = tan(delta(n,3,:));

    tan_eta(n,:) = (tandelta(n,:).*(tan_phi(n,:)+tanalpha(n,:))) ./ ...
                    (tan_phi(n,:)+tanbeta(n,:));
end
eta_n = atan(tan_eta);


% The pressure distribution in the scattered wave at large distances

for nu = 1:numax,
    n = nu-1;
    pn = legendre(n,cos(theta));    %Computing the Legendre Polynomial
    Ps(nu,:) = (((2*n)+1)*sin(eta_n(nu,:))...
        .*exp(i*eta_n(nu,:))*pn(1));

end

Pss =  (Po./(k3*r)).*abs(sum(Ps(:,:)));

% Calculating the differential scattering form function phi_180

phi_180 = (Pss*r)./(Po*exp(i*k3*r));

% Determine the differential scattering cross-section

sigmadbs = abs(phi_180).^2;

% Determine the backscattering coefficient

eta_density = 10^5;                                   % Number Density
BSC = (sigmadbs*1E4)*eta_density;                     % Backscatter Coefficient
```

MATLAB Code for the Scattering from an Elastic Cylinder

```
% The purpose of this code is to derive a solution for the scattering from an infinite elastic cylinder.
% Solution obtained from Faran’s paper.

clear all;

% Define all the constants

N = 3000;
dia = 30e-6;                                            % Diameter of cyl
a =dia/2;                                               % Radius of the cyl
Po = 1e5;                                               % Incident wave pressure amplitude
f = linspace(.1e6, 100e6, N);                           % Frequency range
omega = 2*pi*f;                                         % Angular frequency range
rho1 = 3.8e3;                                           % Density of scatterer
rho3 = 1000;                                            % Density of fluid;
sigma = .24;                                            % Poisson's ratio
E = 65e9;                                               % Young's modulus

% Determine velocities

c1 = ((E*(1-sigma))/(rho1*(1+sigma)*(1-2*sigma)))^0.5;  % Comp. velocity in scatterer
c2 = [E/(2*rho1*(1+sigma))]^0.5;                        % Shear wave vel. in scatteres
c3 = 1500;                                              % Velocity of sound in fluid

% Determine wave numbers

k1 = omega/c1;
k2 = omega/c2;
k3 = omega/c3;

%Distance of observation

r = 1;

% x-values

x(1,:) = k1*a;
x(2,:) = k2*a;
x(3,:) = k3*a;
x(4,:) = k3*r;

%Angle of observation

theta = pi;                                             % For backscatter theta=pi


% Compute spherical Bessel and Neumann functions

numax = 10;                                              % Maximum number of points
```

```
for xcnt = 1:4,
     for nu = 1:numax+1,
       n = nu - 1;
       bsl(nu,xcnt,:) = besselj(n,x(xcnt,:));
       neu(nu,xcnt,:) = bessely(n,x(xcnt,:));
   end
end

% Compute derivatives of spherical Bessel and Neumann functions

for xcnt = 1:4,
     bsld(1,xcnt,:) = -bsl(2,xcnt,:);
     neud(1,xcnt,:) = -neu(2,xcnt,:);
     for nu = 2:numax,
         n = nu - 1;
         bsld(nu,xcnt,:) = 1/2 * (bsl(nu-1,xcnt,:) - bsl(nu+1,xcnt,:));
         neud(nu,xcnt,:) = 1/2 * (neu(nu-1,xcnt,:) - neu(nu+1,xcnt,:));
     end
end

% Determine the intermediate angles

for nu=1:numax,
     rebsl_1(nu,:) = bsl(nu,1,:);
     rebsl_2(nu,:) = bsl(nu,2,:);
     rebsl_3(nu,:) = bsl(nu,3,:);
     rebsld_1(nu,:) = bsld(nu,1,:);
     rebsld_2(nu,:) = bsld(nu,2,:);
     rebsld_3(nu,:) = bsld(nu,3,:);
     reneu_1(nu,:) = neu(nu,1,:);
     reneu_2(nu,:) = neu(nu,2,:);
     reneu_3(nu,:) = neu(nu,3,:);
     reneud_1(nu,:) = neud(nu,1,:);
     reneud_2(nu,:) = neud(nu,2,:);
     reneud_3(nu,:) = neud(nu,3,:);
end

for nu = 1:numax,
     delta_1(nu,:) = atan(-rebsl_1(nu,:) ./ reneu_1(nu,:));
     alpha_1(nu,:) = atan(-x(1,:).*rebsld_1(nu,:) ./ rebsl_1(nu,:));
     beta_1(nu,:) = atan(-x(1,:).*reneud_1(nu,:) ./ reneu_1(nu,:));

     delta_2(nu,:) = atan(-rebsl_2(nu,:) ./ reneu_2(nu,:));
     alpha_2(nu,:) = atan(-x(2,:).*rebsld_2(nu,:) ./ rebsl_2(nu,:));
     beta_2(nu,:) = atan(-x(2,:).*reneud_2(nu,:) ./ reneu_2(nu,:));

     delta_3(nu,:) = atan(-rebsl_3(nu,:) ./ reneu_3(nu,:));
     alpha_3(nu,:) = atan(-x(3,:).*rebsld_3(nu,:) ./ rebsl_3(nu,:));
     beta_3(nu,:) = atan(-x(3,:).*reneud_3(nu,:) ./ reneu_3(nu,:));
 end

% Determine the scattering phase angle
```

```
for nu=1:numax,
    n = nu - 1;
    tan1(nu,:) = tan(alpha_1(nu,:));
    tan2(nu,:) = tan(alpha_2(nu,:));  %
    X2 = 0.5*x(2,:).^2;
    term1(nu,:) = (tan1(nu,:)./(tan1(nu,:)+1));
    term2(nu,:) = ((n^2)./(n^2-X2+tan2(nu,:)));
    term3(nu,:) = ((n^2-X2+tan1(nu,:))./(tan1(nu,:)+1));
    term4(nu,:) = (((n^2)*(tan2(nu,:)+1))./(n^2-X2+tan2(nu,:)));

    zeta(nu,:) = atan( (-X2).*(term1(nu,:)-term2(nu,:))./(term3(nu,:)-term4(nu,:)));
end


%Determine the boundary impedance phase angle

for n=1:numax,
    tan_phi(n,:) = -(rho3/rho1)*tan(zeta(n,:));
end

%Phase shift of the nth scattered wave

for n=1:numax,
    tanalpha(n,:) = tan(alpha_3(n,:));
    tanbeta(n,:) = tan(beta_3(n,:));
    tandelta(n,:) = tan(delta_3(n,:));

    tan_eta(n,:) = (tandelta(n,:).*(tan_phi(n,:)+tanalpha(n,:))) ./ ...
                (tan_phi(n,:)+tanbeta(n,:));
 end

 eta_n = atan(tan_eta);

% Pressure distribution in the scattered wave at large distances

for nu = 1:numax,
    n = nu-1;

    if n == 0;
        epsilon = 1;
    else epsilon = 2;
    end

    Ps(nu,:) = (epsilon*sin(eta_n(nu,:))...
        .*exp(i*eta_n(nu,:))*cos(n*theta));
end

Pss =  (Po*(2./(pi*k3*r)).^0.5).*abs(sum(Ps(:,:)));

% Calculating the backscattering from form function phi_180

phi_180 = ((2*r/a)^0.5)*((Pss)/Po);
```

```
% Determine the differential scattering cross-section

sigmadbs = abs(phi_180).^2;

% Determine the backscatter coefficient

eta_density = 1;                              % Number Density
BSC = (sigmadbs*1E4)*eta_density;             % Backscatter Coefficient
```

MATLAB Code for the Scattering from *Optison*® Contrast Agents

```
% The purpose of this code is to derive a solution for the scattering from
% contrast agent microbubbles corrected for the size distribution.
% Theoretical solution obtained from Church's paper.

clear all;

% Define Constants

f=[5E6:0.5E6:30E6];                             % Frequency range
omega=2*pi*f;                                   % Angular frequency

% Liquid Parameters

P0=0.1E6;                                       % Ambient Pressure in Pa
rhol=1E3;                                       % Density in Kg/m^3
mul=0.001;                                      % Shear Viscosity Pa-s
sigma1 = 40E-3;                                 % N/m
c=1500;                                         % Sound Speed in liquid m/s

%Shell Parameters

rhos=1.1E3;                                     % Density Kg/m^3;
mus=1.77;                                       % Viscosity Pa-s
sigma2 = 5e-3;                                  % N/m
Gs=88.8e6;                                      % Shear elastic modulus MPa
Rs=15e-9;                                       % Thickness of sheel in m

%Gas Parameters

kappa=1.1;                                      % Polytropic Exponent

% Define a bin size and number of points per bin for discretization

binsize = 0.25*1E-6;                            % Bin Size (mum)
binpts = 100;                                   % Points in every bin
inc = binsize/binpts;                           % Increment
R01= 0.25E-6:inc:2.5E-6;                        % Inner Radius

N = length(R01);                                % Number of points

%Estimate resonance frequency and scattering cross-section as a function of microbubble radius

for j=1:1:length(f)
  for i=1:1:N
  R02(i)=Rs+R01(i);
  Vs(i)=R02(i)^3-R01(i)^3;
  alpha(i)=1+((rhol-rhos)/rhos)*(R01(i)/R02(i));
  deltad(i)=4*((Vs(i)*mus+R01(i)^3*mul)/R02(i)^3)*(rhos*R01(i)^2*alpha(i))^(-1);
```

```
  %Resonance Frequency

  Z(i) = ((2*sigma1/R01(i))+(2*sigma2/R02(i)))*(R02(i)^3/Vs(i))*(4*Gs)^-1;

  omega0(i)=( (rhos*R01(i)^2*alpha(i)).^-1 * ((3*kappa*P0)-(2*sigma1/R01(i))-
(2*sigma2*R01(i)^3/R02(i)^4)...
     +4*(Vs(i)*Gs/R02(i)^3)*(1+Z(i)*(1+(3*R01(i)^3/R02(i)^3)))) )^0.5;

  freef0(i)=omega0(i)/(2*pi);

  OMEGA(i,j)=omega(j)/omega0(i);

  delta(i)=deltad(i)/omega0(i);

  Chi1(i,j)=((1-OMEGA(i,j)^2)^2+delta(i)^2*OMEGA(i,j)^2)^(-0.5);

  %Scattering Cross-Section

  sigmas1(i,j)=(4*pi*R01(i)^2*OMEGA(i,j)^4*Chi1(i,j)^2*rhol^2)/(alpha(i)^2*rhos^2);
   end
end

% Discretize the results

for j = 1:length(f),
   for i = binpts+1:binpts:N,
      sigmabar(i-binpts:i,j) = sigmas1((i-(binpts/2)),j);
   end
end

% Reported values for the distribution of Optison Microbubbles

dist = [0 .032 0.079 .254 .317 .206 .079 0.032 0];               % In %bubbles

eta_density = 6.5E4;                                             % Ave Number density

% Compute the Backscattering Coefficient

for j = 1:length(f),
   for  i = 1:length(dist),
       BSCbar(i,j)= (sigmabar(i*binpts,j))*1E4*eta_density*dist(i) /(4*pi);
   end
end

BSC_Corrected = sum(BSCbar(:,:));
```

Bibliography

[1] J.W.S. Rayleigh, *Investigation of the disturbance produced by a spherical obstacle on the waves of sound*, Proceedings of the London Mathematical Society, 4: 253, 1872.

[2] J.W.S. Rayleigh, *On the pressure developed by a liquid during the collapse of a spherical cavity*, Philosophical Magazine, 34: 94, 1917.

[3] M. Minnaert, *On musical air bubbles and sounds of running water*, Philosophical Magazine, 16: 235, 1933.

[4] L. L. Foldy, *The multiple scattering of waves I. General thoery of isotropic scattering by randomly distributed scatterers*, Physical Review, 67: 107, 1945.

[5] M.S. Plesset, *The dynamics of cavitation bubbles*, Journal of Applied Mechanics, 16: 277, 1949.

[6] V.C. Anderson, *Sound scattering from a fluid sphere*, Journal of the Acoustical Society of America, 22: 426, 1950.

[7] B.E. Noltingk and E.A. Neppiras, *Cavitation produced by ultrasonics*, Proceedings of the Physical Society, B63: 674, 1950.

[8] J. Faran Jr., *Sound scattering by solid cylinders and spheres*, Journal of the Acoustical Society of America, 23: 405, 1951.

[9] E.A. Neppiras and B.E. Noltingk, *Cavitation produced by ultrasonics: theoretical conditions for the onset of cavitation*, Proceedings of the Physical Society, B64: 1032, 1951.

[10] E.L. Carstensen, K. Li, and H.P. Schwan, *Determination of the acoustic properties of blood and its components*, Journal of the Acoustical Society of America, 25: 286, 1953.

[11] C. Devin, *Survey of thermal, radiation, and viscous damping of pulsating air bubbles in water*, Journal of the Acoustical Society of America, 31: 1654, 1959.

[12] P. Waterman and R. Truell, *Multiple scattering of waves*, Journal of Mathematical Physics, 2: 517, 1961.

[13] R. R. Goodman and R. Stern, *Reflection and transmission of sound by elastic spherical shells*, Journal of the Acoustical Society of America, 34: 338, 1962.

[14] R. Hickling, *Analysis of echoes from a solid elastic sphere in water*, Journal of the Acoustical Society of America, 34: 1582, 1962.

[15] R. Hickling, *Analysis of echoes from a hollow metallic sphere in water*, Journal of the Acoustical Society of America, 36: 1124, 1964.

[16] V. Twersky, *Acoustic bulk parameters of random value distributions of small scatterers*, Journal of the Acoustical Society of America, 36: 1314, 1964.

[17] R. Hickling, *Echoes from spherical shells in air*, Journal of the Acoustical Society of America, 42: 388, 1967.

[18] J.V. Dacie and S.M. Lewis, *Practical Haematology*, Grune and Stratton Inc., fourth edition, 1968.

[19] R. D. Doolittle and H. Uberall, *Sound scattering by elastic cylinders*, Journal of the Acoustical Society of America, 43: 1, 1968.

[20] R. D. Doolittle and H. Uberall, *Sound scattering by elastic cylindrical shells*, Journal of the Acoustical Society of America, 39: 272, 1968.

[21] P. M. Morse and K. U. Ingard, *Theoretical Acoustics*, McGrw-Hill, 1968.

[22] J.W.S. Rayleigh, *The Theory of Sound*, Dover Publications, 1968.

[23] J.W. Delaney and G. Garratty, *Handbook of Haematological and Blood Transfusion Technique*, Appelton-Century-Crofts, second edition, 1969.

[24] J.M. Reid, R.A. Sigelmann, M. Nasser, and D. Baker, *The scattering of ultrasound by human blood*, 8th International Conference of Medicine and Biomedical Engineering, Paper #10-7, 1969.

[25] R.A. Sigelmann and J.M. Reid, *Analysis and measurement of ultrasound backscattering from an ensemble of scatterers excited by sine-wave bursts*, Journal of the Acoustical Society of America, 53: 1351, 1972.

[26] P. Atkinson and M.V. Berry, *Random noise in ultrasonic echoes of diffracted blood*, Journal of Physics A: Mathematical & General, 7: 1293, 1974.

[27] K.K. Shung, R.A. Sigelmann, and J.M. Reid, *Scattering of ultrasound by blood*, IEEE Transactions in Biomedical Engineering , 23: 460, 1976.

[28] H. D. Dardy, J. A. Bucaro, L. S. Scheutz, and L. R. Dragonette, *Dynamic wide-bandwidth acoustic form function determination*, Journal of the Acoustical Society of America, 62: 1373, 1977.

[29] G.C. Gaunaurd, *The sonar cross-section of a hollow coated cylinder in water*, Journal of the Acoustical Society of America, 61: 360, 1977.

[30] L.S. Scheutz and W.G. Neubauer, *Acoustic reflection from cylinders – nonabsorbing and absorbing*, Journal of the Acoustical Society of America, 62: 513, 1977.

[31] L.A. Segal, *Mathematics Applied to Continuum Mechanics*, Dover Publications, 1977.

[32] S. H. Borders, A. Fronek, W. S. Kemper, and D. Franklin, *Ultrasonic energy backscatter from blood: An experimental determination of the variation of sound energy with hematocrit*, Annals of Biomedical Engineering , 6: 83, 1978.

[33] V. Twersky, *Acoustic bulk parameters in distributions of pair-correlated scatterers*, Journal of the Acoustical Society of America, 64: 1710, 1978.

[34] B.A.J. Angelsen, *A theoretical study of the scattering of ultrasound from blood,* IEEE Transactions in Biomedical Engineering, 27: 61, 1980.

[35] A. D. Pierce, *Acoustics: An Introduction to its Physical Principles and Applications*, McGraw-Hill, 1981.

[36] R.E. Apfel, *Acoustic cavitation: A possible consequence of biomedical uses of ultrasound*, British Journal of Cancer, 45: 140, 1982.

[37] H.G. Flynn, *Generation of transient cavities in liquids by microsecond pulses of ultrasound*, Journal of the Acoustical Society of America, 72: 1160, 1982.

[38] A.E. Hay and R. W. Burling, *On sound scattering and attenuation in suspensions, with marine applications*, Journal of the Acoustical Society of America, 72: 950, 1982.

[39] K.K. Shung, *On ultrasound scattering from blood as a function of hematocrit*, IEEE Transactions in Sonics and Ultrasonics, 29: 327, 1982.

[40] M.A.H Weiser, R.E. Apfel, E.A. Neppiras, *Interparticle forceson red cells in a standing wave field*, International Journal on Acoustics, 56: 114, 1984.

[41] R.A. Roy, A.A. Atchley, L.A. Crum, J.B. Fowlkes and J.J. Reidy, *A precise technique for the measurement of acoustic cavitation thresholds and some preliminary results*, Journal of the Acoustical Society of America, 78: 1799, 1985.

[42] W.G. Neubauer, *Acoustic Reflection from Surfaces and Shapes*, Naval Research Laboratory, 1986.

[43] R.A. Roy, *Quantitative Particle Characterization by Scattered Ultrasound*, PhD Dissertation, Yale University, 1987.

[44] A.A. Atchley, L.A. Frizzell, R.E. Apfel, C.K. Holland, S. Madanshetty, and R.A. Roy, *Thresholds for cavitation produced in water by pulsed ultrasound*, Ultrasonics, 26: 280, 1988.

[45] T. Hasegawa, K. Saka, N. Inoue, and K. Matsuzawa, *Acoustic radiation force experienced by a solid cylinder in a plane progressive field*, Journal of the Acoustical Society of America, 83: 1770, 1988.

[46] V. Twersky, *Low frequency scattering by correlated distributions of randomly oriented particles*, Journal of the Acoustical Society of America, 84: 409, 1988.

[47] Y.W. Yuan and K.K. Shung, *Ultrasonic backscatter from flowing whole blood I: Dependence on shear rate and hematocrit*, Journal of the Acoustical Society of America, 84: 1195, 1988.

[48] Y.W. Yuan and K.K. Shung, *Ultrasonic backscatter from flowing whole blood II:Dependence on frequency and fibrinogen concentration*, Journal of the Acoustical Society of America, 84: 52, 1988.

[49] K. Commander and A. Prosperetti, *Linear pressure waves in bubbly liquids: Comparison between theory and experiment*, Journal of the Acoustical Society of America, 85: 732, 1989.

[50] R.A. Roy, and R.E. Apfel, *Mechanical characterization of microparticles by scattered ultrasound*, Journal of the Acoustical Society of America, 87: 2332, 1990.

[51] R.A. Roy, C.C. Church, and A. Calabrese, *Cavitation produced by short pulses of ultrasound*, Frontiers of Nonlinear Acoustics: Proceedings of 12th ISNA, pg. 476, Elsevier Science Publishers Ltd, London, 1990.

[52] R.A. Roy, S. I. Madanshetty and R.E. Apfel, *An acoustic backscattering technique for the detection of transient cavitation produced by microsecond pulses of ultrasound*, Journal of the Acoustical Society of America, 87: 2451, 1990.

[53] G.R. Lockwood, L.K. Ryan, J.W. Hunt, and F.S. Foster, *Measurement of the ultrasonic properties of vascular tissues and blood from 35-65 MHz,* Ultrasound in Medicine and Biology, 17: 653, 1991.

[54] S. I. Madanshetty, R.A. Roy, and R.E. Apfel, *Acoustic microcavitation: its active and passive detection*, Journal of the Acoustical Society of America, 90: 1515, 1991.

[55] L.A. Crum, R.A. Roy, M.A. Dinno, C.C. Church, R.E. Apfel, C.K. Holland, and S.I. Madanshetty, *Acoustic cavitation produced by microsecond pulses of ultrasound: a discussion of some selected results,* Journal of the Acoustical Society of America, 91: 1113, 1992.

[56] C.K. Holland, R.A. Roy, R.E. Apfel, and LA. Crum, *In vitro detection of cavitation induced by a diagnostic ultrasound system*, IEEE Transactions on Ultrasonics, Ferroelectrics, and Frequency Control, 39: 95, 1992.

[57] N. de Jong, L. Hoff, T. Skotland, and N. Bom, *Absorption and scatter of encapsulated gas filled microspheres: theoretical considerations and some measurements,* Ultrasonics, 30: 95, 1992.

[58] N. de Jong, and L. Hoff, *Ultrasonic scattering properties of Albunex microspheres*, Ultrasonics, 31: 175, 1993.

[59] T. Hasegawa, Y. Hino, A. Annou, H. Noda, M. Kato, and N. Inoue, *Acoustic radiation pressure acting on spherical and cylindrical shells,* Journal of the Acoustical Society of America, 93: 154, 1993.

[60] V.E. Huertas, I.R.S. Makin, and E.C. Everbach, *Active cavitation detection of microbubble echocontrast agents in blood,* Journal of the Acoustical Society of America, 95: 2856, 1994.

[61] T. G. Leighton, *The Acoustic Bubble,* Academic Press, 1994.

[62] C.C. Church, *The effects of an elastic solid surface layer on the radial pulsations of gas bubbles*, Journal of the Acoustical Society of America, 97: 1510, 1995.

[63] A.M Calabrese, *Threshold measurements and production rates for inertial cavitation due to pulsed, megahertz-frequency ultrasound,* PhD dissertation, University of Mississippi, 1996.

[64] Z. Ye, *On sound scattering and attenuation of Albunex*$^{®}$ *bubbles*, Journal of the Acoustical Society of America, 100: 2011, 1996.

[65] S.H. Wang and K.K. Shung, *An approach for measuring ultrasonic backscattering from biological tissues with focused transducers*, IEE Transactions in Biomedical Engineering, 44: 5489, 1997.

[66] J.N. Marsh, M.S. Hughes, C.S. Hall, H. Lewis, R.L. Trousil, G.H. Brandenburger, H.L. Levene, and J.G. Miller, *Frequency and concentration dependence of the backscatter coefficient of the ultrasound contrast agent Albunex*$^{®}$, Journal of the Acoustical Society of America, 104: 1654, 1998.

[67] J.B. Fowlkes and C.K. Holland, *Mechanical bioeffects from diagnostic ultrasound: AIUM consensus statements*, Journal of Ultrasound in Medicine, 19, 2000.

[68] D.T. Blackstock, *Fundamentals of Physical Acoustics*, John Wiley and Sons Inc., 2000.

[69] R.S. Figliola and D.E. Beasley, *Theory and Design for Mechanical Measurements*, John Wiley and Sons Inc., 2000.

[70] Mallinckrodt Inc., *Optison*® (Human Albumin Microspheres) Injectable suspension octafluoropropane formulation, instruction manual, 2000.

[71] J.S. Allen, D. E. Kurse, and D.W. Ferrara, *Shell waves and acoustic scattering from ultrasound contrast agents,* IEEE Transactions on Ultrasonics, Ferroelectrics, and Frequency Control, 48, 2001.

[72] C.C. Coussios, *Monitoring of Hemolysis by Acoustic Scattering*, PhD dissertation, Pembroke College, University of Cambridge, 2001.

[73] L. Hoff, *Acoustic Characterization of Contrast Agents for Medical Ultrasound Imaging*, Kluwer Academic Publishers, 2001.

[74] S.H. Wang, L.P. Lee, J.S. Lee, *A linear relation between the compressibility and density of blood*, Journal of the Acoustical Society of America, 109: 390, 2001.

[75] S. Maruvada, K.K. Shung, and S.H. Wang, *High-frequency backscatter and attenuation measurements of porcine erythrocyte suspensions between 30-90 MHz,* Ultrasound in Medicine and Biology, 28: 1081, 2002.

[76] J. Ostensen, P.C. Sontum, L. Hoff, R. Bendilksen, *Microbubble volume concentration: A better efficacy parameter for US contrast agents than the number concentration,* Academic Radiology, Vol. 9 (suppl. 1): S38, 2002.

[77] C.R. Thomas, *Design, Fabrication and Use of A KC-135 Experiment for Studying Sonoluminescence*, Masters Thesis, Boston University, 2003.

[78] Panametrics, *Ultrasonic Transducers – Catalog*, 2003.

[79] Professor Ronald A. Roy, *Personal Communication*, 2004.

Vita

Paolo Zanetti was born in Melbourne, Australia in 1980, son of Giancarlo and Gabriella Zanetti. He has two older siblings: Flavio Zanetti, his older brother, and Chiara Zanetti Guisgant, his older sister. In 1984 Paolo's family moved to Tangier, Morocco where Paolo attended elementary school at The American School of Tangier. After eight years in Morocco, in 1992, Paolo headed back to his ancestral home, Italy, where he first enrolled in the American Overseas School of Rome for his middle school years, followed by the Liceo Classico De Sanctis (Italian high school). Following a stay of four years in Rome, Paolo was again on the move. His family moved to Bonn, Germany, where he attended Bonn American High School (11th grade), followed by Bonn International School (12th grade).

After obtaining his American High School Diploma and the equivalent Italian Scientific High School Diploma, in the fall of 1998, Paolo moved to Boston to study Mechanical Engineering at Boston University. Here, he met professor Robin Cleveland, his advisor, whom he worked for, starting in 2001, as an undergraduate research assistant, looking at the fragmentation of kidney stones with shock wave lithotripsy. In the summer of 2002, after graduating with his B.S. in mechanical engineering, Paolo started working for professor Ronald A. Roy as a research assistant. Paolo then entered the M.S. program at Boston University the following fall. A brief curriculum vitae follows on the next page.

Permanent Address: Via Francesco Ferrara 50, 00191 Rome, Italy

CURRICULUM VITAE: Paolo Zanetti 4/1/2004

Year and Place of Birth: 1980, Melbourne, Australia
Nationality: Italian
Address: 84 Gardner Street Apt 37, Allston MA 02134, U.S.A.
Telephone: +1 (617) 783-5309; +1 (857) 204-3249
email: pzanetti@bu.edu, zannafdg@hotmail.com

EDUCATION

M.S. Mechanical Engineering, May 2004
Boston University, College of Engineering
Advisor: Professor Ronald A. Roy
GPA: 3.7 / 4.0
Thesis Title: *Parameters Affecting the Detection and Imaging of Microbubbles in Blood*

B.S. Mechanical Engineering, May 2002
Boston University, College of Engineering
Advisor: Professor Robin O. Cleveland
GPA: 3.6 / 4.0
Capstone Project: *3-D Positioning System*
Concentration: Fluid Mechanics

HONORS AND AWARDS

- B.U. Graduate Research Assistantship
- B.U. B.S. Magna Cum Laude
- B.U. Dean's List (1998-2002)
- Golden Key International Honors Society
- B.U. Pi-Tau-Sigma Honors Society

RESEARCH EXPERIENCE

September 2002 – Present
Graduate Research Assistant
Boston University
Department of Aero. and Mech. Engineering
Supervisor: Ronald A. Roy

May 2002 – August 2002
Research Assistant
Boston University
Department of Aero. and Mech. Engineering
Supervisors: Ronald A. Roy, William Carey

September 2001 – May 2002
Undergraduate Research Assistant
Boston University
Department of Aero. and Mech. Engineering
Supervisor: Robin O. Cleveland

PROFESSIONAL AFFILIATIONS

- The Acoustical Society of America (ASA)
- The American Society of Mechanical Engineers (ASME)

SELECTED PUBLISHED ABSTRACTS

C. C. Coussios, P. Zanetti, R. A. Roy, *Parameters affecting the detection of microbubbles in blood*, JASA, 114 (4): 2321, 2003.

P. Zanetti, C. C. Coussios, R. A. Roy, *Signal to noise ratio and attenuation through blood and Optison® microbubbles*, JASA, 115 (4): 2322, 2004.

SELECTED PRESENTATIONS

November 18th 2003
CenSISS Research and Industrial Collaboration Conference
Northeastern University
Title: *Parameters Affecting the Imaging of Microbubbles in Blood*

April 8th 2003
CenSISS Year Three Site Visit
Boston University
Title: *An Ultrasound TestBED for Supporting Research in Biomedical, Nonlinear, and Dual-Wave Imaging*

LANGUAGES

- Italian – Mother tongue
- English, French, and Spanish – Fluent
  - French Summer Course, University of Geneva, Switzerland, June 2001
  - Spanish Summer Course, Istituto Mediterraneo Sol, Granada, Spain, May 2000